TÉCNICO LISBOA

UNIVERSIDADE DE LISBOA

INSTITUTO SUPERIOR TÉCNICO

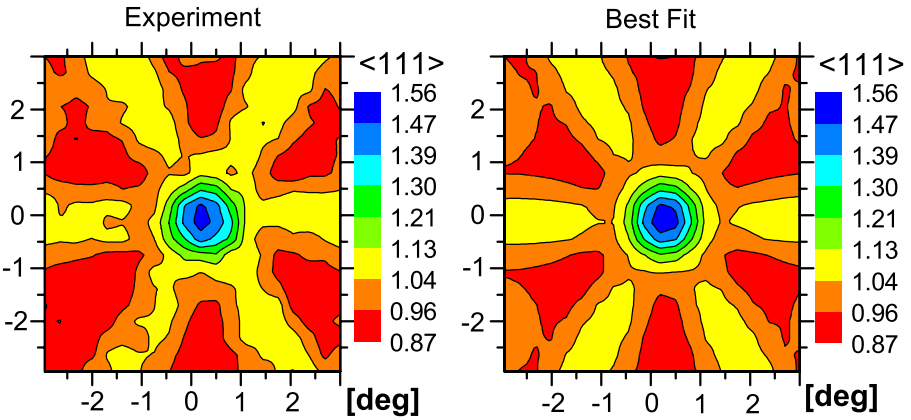

Lattice location of impurities in Silicon Carbide

Ângelo Rafael Granadeiro Costa

Supervisor: Doctor Ulrich Wahl

Co-Supervisor: Doctor João Guilherme Martins Correia

Thesis approved in public session to obtain the PhD Degree in Physics

Jury final classification: Pass with Distinction

2018

TÉCNICO LISBOA

UNIVERSIDADE DE LISBOA

INSTITUTO SUPERIOR TÉCNICO

Lattice location of impurities in Silicon Carbide

Ângelo Rafael Granadeiro Costa

Supervisor: Doctor Ulrich Wahl

Co-Supervisor: Doctor João Guilherme Martins Correia

Thesis approved in public session to obtain the PhD Degree in Physics

Jury final classification: Pass with Distinction

Jury

Chairperson : Doctor José Luís Rodrigues Júlio Martins, Instituto Superior Técnico, Universidade de Lisboa
Members of Committee:
Doctor Krishanlal Bharuth-Ram, Faculty of Applied Sciences, Durban University of Technology, Africa do Sul
Doctor Ulrich Wahl, Instituto Superior Técnico, Universidade de Lisboa
Doctor Lino Miguel da Costa Pereira, Faculty of Science, KU Leuven, Bélgica
Doctor Katharina Lorenz, Instituto Superior Técnico, Universidade de Lisboa

Funding Institutions

Portuguese Foundation for Science and Technology (CERN/FIS-NUC/0004/2015, UID/Multi/04349/2013 and SFRH/BD/86386/2012)
FWO Vlaanderen and the KU Leuven (STRT/14/002 and GOA/14/007)
European Commission through the Horizon 2020 program (grant number 654002 ENSAR2)

2018

Acknowledgments

I must start by giving my special thanks to my co-supervisor Dr. João Guilherme Correia, for giving me the opportunity to work at CERN, to introduce me to my supervisor, Dr. Ulrich Wahl and the world of emission channeling. Also, thank you Guilherme for your patience, knowledge and guidance in those hundreds of hours hands-on work passed in both 275 and 508 laboratories.

My most sincere thank you goes to you Uli, for having accompanied my work through all my PhD all the way to the last line written in this thesis. None of this would have been possible without your vision, immense technical knowledge, precious guidance and enormous patience.

I would like to thank Fundação para a Ciência e Tecnologia (FCT), for the financial support of my PhD (SFRH/BD/86386/2012). The ISOLDE collaboration is also acknowledged for providing pure radioactive beams. A special thank you is reserved for you Tânia, for your concern in providing us the best optimized radioactive beam whenever you were in control.

I am thankful to a number of many wonderful people, who contributed to the success of this thesis, without you people, none of this would have been possible. A big thanks to all the people from CTN in Bobadela, specially Cátia, Sérgio and Maria Isabel for your help and support. A special word of thanks to Dr. Rui Silva for the many hours spent in conversation about physics. I learned a lot with you.

To my CERN office buddies Abel, Eric and Tânia a big thank you is in order for your support, very nice long lunches at Restaurant 1 and, most of the time, very nice coffee breaks full of stimulating discussions (some scientific, others not so much).

Thank you, Lino, Eric, Valérie, Daniel and Tiago, for your help during the long sleepless beam time nights. Without you people, those nights would have been harder to pass.
Above all, a special thanks to my family for their encouragement and for being always there for me.
Finally, thank you Sónia, for your understanding, patience and for always standing by my side. Without you this PhD would not have been possible.

Resumo

A presença e comportamento dos metais de transição (MT) em semicondutores tais como o silício ou carboneto de silício tem sido uma preocupação constante desde do início da sua produção a nível industrial. Estes são contaminantes difíceis de evitar, geralmente introduzidos de forma não intencional durante o crescimento do cristal e fabrico de dispositivos. Em particular no carboneto de silício, formam facilmente níveis de energia profundos no hiato de energia, quando isolados ou quando formando complexos com outros defeitos que possam existir na rede cristalina do semicondutor.

Diversos estudos indicam que os MT, no interior do carboneto de silício, possuem coeficientes de difusão muito baixos e, consequentemente, são considerados imóveis durante o crescimento epitaxial do mesmo. No entanto, durante o processo de fabrico de dispositivos baseados neste semicondutor, são necessários passos de recozimentos a elevadas temperaturas, seja para recuperação da rede cristalina devido à implantação iónica de dopantes elétricos, ou para efeito de ativação dos mesmos. Durante a realização destes processos a elevadas temperaturas, é possível que os MT se movam e atinjam a região ativa do semicondutor degradando as suas características elétricas.

Os MT também podem ser usados como dopantes magnéticos em semicondutores. Semicondutores binários têm sido investigados com bastante interesse, depois da descoberta do ferromagnetismo no semicondutor dopado com Mn "diluído" (Ga,Mn)As. No entanto, a temperatura máxima de Curie encontrada chega apenas a 185 K, que é muito baixa para aplicações práticas. A necessidade de se ter temperaturas de Curie mais elevadas (à temperatura ambiente) levou a que outros semicondutores, tais como o carboneto de silício e o silício entre

outros, fossem considerados. No que respeita ao carboneto de silício, MTs tais como crómio, manganês ou ferro são considerados como possíveis candidatos a dopantes magnéticos se localizados na posição substitucional do silício.

Todas estas questões podem ser exploradas através do estudo das posições dos MT após o processo de implantação. Neste trabalho foram investigadas as posições e respetiva estabilidade térmica dos elementos Mn, Fe, Ni e Ag utilizando a técnica "emission channeling" através de dopagem por implantação iónica dos isótopos radioativos ^{56}Mn, ^{59}Fe, ^{65}Ni e ^{111}Ag em duas diferentes estruturas cristalinas do carboneto de silício: 3C (estrutura cristalina cúbica) e 6H (estrutura cristalina hexagonal). Para os isótopos de Mn, Fe e Ni implantados na estrutura cúbica do carboneto de silício, foram identificadas posições deslocadas relativamente à posição substitucional do silício ("near S_{Si}"); já para a estrutura hexagonal do carboneto de silício, foram identificadas posições substitucionais do silício ("ideal S_{Si}"). Foram também identificadas posições intersticiais tetraédricas coordenadas pelo carbono ("ideal T_C") em ambas as estruturas cristalinas, onde se verificou que a maioria dos átomos de Mn, Fe e Ni implantados se encontram localizados nesta última posição. A dependência da ocupação das posições substitucional Si e intersticial tetraédrica coordenada por carbono com a temperatura de recozimento foi análoga para os átomos implantados de Mn, Fe e Ni e em ambas as estruturas cristalinas do carboneto de silício aqui estudadas, o que é indicativo de que os respetivos complexos devem ser formados independentemente da natureza dos MT em estudo. Os átomos de Mn, Fe e Ni desaparecem parcialmente das posições "ideal T_C" após recozimento a temperaturas de 500 °C e 700 °C, dependendo especificamente do elemento em questão. Este processo é acompanhado pelo aumento das fracções destes MT ocupando, em minoria, posições substitucionais do silício – designadas por lacunas de silício e a maioria, em posições "random" – termo geralmente usado para descrever posições de baixa simetria cristalográfica ou com vizinhança amorfa. Esta mudança de posições ocorre no mesmo intervalo de temperatura que a literatura sugere que acontece a transformação das lacunas de silício em complexos lacuna-antisite de carbono ($V_{Si} \rightarrow V_C$-C_{Si}), e consequentemente não disponíveis em quantidade suficiente para funcionarem como principais posições de captura dos MT. Os valores da energia de ativação da migração correspondentes aos TM no intervalo de temperatura já referido variam entre 1.7 eV e 3.2 eV. As lacunas de silício resultam originalmente do processo de implantação dos MT na rede cristalina do carboneto de silício, mas desaparecem com sucessivos recozimentos até ao máximo de 750 °C. De facto, a literatura identifica três estádios principais correspondentes a recozimentos a temperaturas de 150 °C, 350 °C e 750 °C, onde os dois primeiros estádios são associados a processos de recombinação de pares de Frenkel com duas

energias de ativação 0.2 eV e 1.4 eV respetivamente, e a terceira associada à transformação $V_{Si} \rightarrow V_C$-C_{Si} com uma energia de 2.2-2.5 eV. Estes valores de energia sobrepõem-se aos valores de energia obtidos para a ativação da migração dos MT pelo que são dois processos que competem entre si, o que pode explicar porque os MT que migram de posições "ideal T_C" não são todos incorporados em lacunas de silício.

No que respeita aos sistemas ^{111}Ag:(3C, 6H)-SiC, 4 amostras foram implantadas com fluências diversas de Ag: (1) 2 amostras de 3C-SiC foram preparadas com fluências de 6×10^{12} Ag^+ cm^{-2} e 1×10^{14} Ag^+ cm^{-2}; (2) 2 amostras de 6H-SiC foram preparadas com fluências de 2×10^{13} Ag^+ cm^{-2} e 1×10^{14} Ag^+ cm^{-2}. Em todos os casos, a maioria dos átomos de Ag implantados foram identificados em posições deslocadas relativamente às posições ideais substitucionais de silício na estrutura 3C-SiC ("near Si") e em posições substitucionais de silício na estrutura 6H-SiC ("ideal Si"). Foi também identificada a ocupação de uma segunda posição pelos átomos de Ag: para a estrutura 3C, na vizinhança da posição substitucional C, apesar dos resultados de "emission channeling" não permitirem identificar claramente a direção do deslocamento e, para a estrutura 6H, na posição intersticial BC. E, contrariamente ao observado para os outros MT, não foram encontrados átomos de Ag em posições intersticiais tetraédricas, coordenadas por carbono ou silício. Verificou-se que o comportamento das frações de Ag com os recozimentos sucessivos, obtidas da análise de "emission channeling", é similar para amostras com fluências implantadas de Ag da mesma ordem de grandeza e não depende da estrutura cristalina cúbica ou hexagonal do cristal.

A fracção de átomos de Ag localizados em posições substitucionais em silício é máxima após o recozimento a 900 °C para todas as amostras. Após o último recozimento, esta fracção diminui sem clara evidência de que existe um aumento correspondente no segundo site – indicativo de uma mudança de posição (substitucional Si $\rightarrow$ intersticial BC). De facto, o total das fracções de ambas posições diminui com o último recozimento, indicativo que os átomos de Ag localizados nas posições substitucionais de silício movem-se para posições "random". Foi estimada a energia de ativação para difusão dos átomos de Ag das posições substitucionais de silício, 3.1-4.1 eV. A literatura sugere dois processos (1) processo de difusão de Franck-Turnbull e (2) processo de "kick-out", como explicações mais prováveis para este processo de difusão. De facto, previsões teóricas apresentam o valor de energia de ativação de 3.35 eV para o processo de "kick-out", valor este que se enquadra bem no intervalo de energias estimado nesta tese. Por outro lado, nenhum valor de energia de ativação para o processo de Franck-Turnbull existe, pelo que não é possível fazer uma comparação com os valores de energia aqui estimadas.

Para produzir carboneto de silício do tipo *n* ou do tipo *p*, elementos do grupo VA ou do grupo IIIA da tabela periódica são usados respectivamente. Enquanto que o Azoto e fósforo são os elementos usados como dopantes eléctricos para produzir carboneto de silício do tipo *n*, os elementos boro e alumínio são a escolha usual para produzir carboneto de silício do tipo *p*. Apesar de cálculos teóricos existentes na literatura preverem energias de ionização similares às do alumínio, o uso deste elemento como dopante elétrico no carboneto de silício ainda não foi documentado.

Neste trabalho foram investigadas as posições e respectiva estabilidade térmica do isótopo radioativo ^{124}In em carboneto de silício cúbico (3C) com a técnica de "emission channeling". Uma fracção de 39% dos átomos de In foram identificados em posições deslocadas da posição substitucional do silício ("near Si"), após o processo de implantação, encontrando-se a restante fração localizada em posições "random". Com a implantação a 600 °C, a fração de In, inicialmente localizada em posições "near Si", encontra-se agora em posições substitucionais do silício, "ideal Si", não ocorrendo mais nenhuma alteração significativa até ao fim da experiência. Após a implantação a 800 °C, obteve-se uma fração máxima de In de 45% em posições substitucionais do silício.

Finalmente, os resultados obtidos nesta tese referentes à caracterização local de dopantes foram comparados com outros resultados, existentes na literatura, obtidos por "emission channeling" em semicondutores como o silício e o diamante. Os resultados referentes ao Fe implantado em carboneto de silício foram também comparados com resultados obtidos por espectroscopia de Mössbauer, também disponíveis na literatura.

Palavras chave: canalização electrónica de emissão, metais de transição, implantação iónica, carboneto de silício, caracterização local de dopantes.

Abstract

The presence and behaviour of transition metals (TMs) in Silicon Carbide (SiC) has been a concern since the start of producing device-grade wafers of this wide band gap semiconductor. They are unintentionally introduced during SiC production, crystal growth and device manufacturing, which makes them difficult contaminants to avoid. Once in SiC they easily form deep levels, either when in the isolated form or when forming complexes with other defects.
On the other hand, using intentional TM doping, it is possible to change the electrical, optical and magnetic properties of SiC. TMs such as chromium, manganese or iron have been considered as possible candidates for magnetic dopants in SiC, if located on silicon lattice sites. All these issues can be explored by investigating the lattice site of implanted TMs. This thesis addresses the lattice location and thermal stability of the implanted TM radioactive probes ^{56}Mn, ^{59}Fe, ^{65}Ni and ^{111}Ag in both cubic 3C- and hexagonal 6H-SiC polytypes by means of emission channeling experiments. For the Mn, Fe and Ni implanted probes in both polytypes, the occupation of displaced Si substitutional (near S_{Si}) sites and tetrahedral interstitial carbon coordinated (ideal T_C) sites was identified directly following room temperature (RT) implantation, with the majority of the TM probes found located in interstitial sites. The dependence of the identified lattice sites on annealing temperature was similar for Mn, Fe and Ni, hence the related complexes may be formed irrespective of the TM nature. The transition metal atoms partially disappear from ideal T_C positions during annealing at temperatures between 500 °C and 700 °C which is accompanied by an increase in the TM fraction on S_{Si} as well on random sites. The site changes were attributed to the onset of interstitial diffusion of the TMs, which allowed estimating values for the migration energies E_M as E_M(Mn)=1.9-2.7

eV, E_M(Fe)=2.3-3.2 eV, and E_M(Ni)=1.7-2.3 eV. The observed site change to random sites also happens in a temperature range where the literature suggests the transformation of the Si vacancy into a carbon vacancy-antisite complex ($V_{Si} \rightarrow V_C$-C_{Si}), and consequently its unavailability as a major trap. Regarding the experiments with Ag, in 3C-SiC case, the ^{111}Ag probes were found near Si substitutional sites and also a second fraction in the vicinity of substitutional C and bond-center (BC) sites, although emission channeling analysis was not able to clearly identify the exact location of this second fraction. As for the more complicated structure of 6H-SiC, where only ideal sites could be considered in the analysis of the experimental data, it was found that the Ag probes are located both at S_{Si} sites and BC sites. In 3C as well as in 6H-SiC the Ag probes occupying both types of sites showed high thermal stability, with the ones located at Si substitutional sites starting to disappear after annealing at 900 °C. From this an activation energy for the dissociation of substitutional Ag was estimated as 3.1-4.1 eV and identified as the onset of diffusion of substitutional Ag, for which two possible processes had been proposed in the literature: Franck-Turnbull diffusion and the so-called kick-out mechanism. The literature only presents a theoretical estimate of 3.35 eV for the activation energy of the kick-out process, which in fact fits quite well within the energy range estimated in this work. For semiconductors to be used effectively in applications they need to be doped with shallow donors or acceptors. While for *n*-type SiC with nitrogen or phosphorus two fairly shallow donors are available, for *p*-SiC, the most commonly used acceptors aluminium or boron are relatively deep. Although theoretical calculations in the literature predict similar ionization energies as in the case of Al, the use of indium as acceptor in SiC has not been documented. Here, the lattice location of ^{124}In in 3C-SiC and its thermal stability was studied as a function of the implantation temperature from RT to 800 °C. It was determined that an In fraction of 39% occupies near substitutional silicon sites after room temperature implantation, with the remaining In fraction sitting on “random” positions. For 600 °C implantation the In fraction located at near S_{Si} sites shifted to ideal S_{Si} sites, a similar result to the one obtained in this work for the other impurities, and related to the recovery of the host crystalline structure from implantation damage with the thermal treatments. Following implantation at 800 °C the In fraction sitting on ideal S_{Si} sites reached its maximum value of 45%. Finally, lattice location results obtained in this thesis were compared to the ones for emission channeling studies in Si and diamond from the literature. The results for Fe in Si were also compared with Mössbauer spectroscopy studies, also available from the literature.

Keywords: emission channeling, transition metals, ionic implantation, silicon carbide, lattice location

Contents

Introduction

Silicon carbide (SiC) is a wide band gap semiconductor with an increasing number of applications able to work not only at high temperatures but also under high-power, high-frequency conditions and in high-radiation environments [Trew1991, Neudeck1994, Choyke2004, Wright2008, Kimoto2015]. These properties make it possible to replace mainstream silicon-based power devices with outperforming SiC-based ones. Table 1 shows the main physical characteristics of SiC at room temperature and some other common semiconductors for comparison.

Table 1. Main physical properties for various common semiconductors at room temperature [Ioffe, Sze1981, Morkoç1994, Chow2004, Willander2006]. Si, GaAs, GaN and Diamond are included for comparison.

	Si	GaAs	3C-SiC	6H-SiC	4H-SiC	GaN	Diamond
Band gap at 300 K E_g (eV)	1.12	1.42	2.4	3.0	3.26	3.4	5.5
Breakdown electric field E_c (MV cm^{-1})	0.3	0.4	1.2	2.5	2.2	3.3	5-10
Electron saturated drift velocity v_{sat} (10^7 cm s^{-1})	1	2.0	2.0	2.0	2.7	2.5	2.7
Electron mobility μ_e (cm^2 V^{-1} s^{-1})	1350	8500	900	370[a] 50[c]	720[a] 650[c]	900	1800
Hole mobility μ_h (cm^2 V^{-1} s^{-1})	480	400	40	80	120	30	1200
Relative dielectric constant ε_r	11.8	12.8	9.7	10	10	8.9	5.5-5.7
Thermal conductivity λ (W cm^{-1} K^{-1})	1.5	0.5	5	5	5	1.3	10-30
Lattice constant (Å)	5.43	5.65	4.36	a=3.08 c=15.12	a=3.08 c=10.08	a=3.19 c=5.19	3.57
Density ρ (g cm^{-3})	2.3	5.3	3.2	3.2	3.2	6.1	3.51

[a] mobility along a-axis
[c] mobility along c-axis

In order to quantify the advantages of semiconductors for various applications several figure of merit parameters (FOMs) have been established [Johnson1965, Keyes1972, Baliga1982, Baliga1989]. The analysis of these FOM will help in assessing the benefits of using wide band gap semiconductors for making power and high frequency devices. Normalized FOM (Si values are used as a normalization factor) of several semiconductors are shown in Table 2. Chow *et al.* [Chow1994] reported a critical evaluation of the performance capabilities of various wide band gap semiconductors for high-power and high frequency unipolar electron devices using seven different FOM. Johnson [Johnson1965] and Keyes [Keyes1972] FOM are basically used for comparison purposes like high frequency and power evaluation. The other FOM are more critical for power device performance. For high-frequency device applications, SiC devices can provide much higher speed compared to Si devices due to higher saturated drift velocity v_{sat} (influence the delay time $\tau = W/v_{sat}$) and lower permittivity ε_r (capacitance $C \propto \varepsilon_r$). Apart from favourable properties of SiC, the full performance of SiC devices is limited by the material quality itself and the contacts (either Schottky or Ohmic) because they provide the means for communication between the device and the outside world.

Table 2. Various figures of merit for several semiconductors. FOM data extracted from [Chow1994].

Material	JM[a] $(E_c v_{sat}/\pi)^2$	KM[b] $\lambda(v_{sat}/\varepsilon_r)^{1/2}$	QF1[c] $\lambda\sigma_A$	QF2[d] $\lambda\sigma_A E_c$	QF3[e] $\sigma_A=\varepsilon_r\mu E_c^3$	BHFM[f] μE_c^2
Si	1.00	1.00	1.00	1.00	1.00	1.00
GaAs	11	0.45	9.4	16	28	16
GaN	790	1.8	910	10300	910	100
3C-SiC	110	5.8	130	550	40	12
4H-SiC	410	5.1	950	9630	290	34
6H-SiC	260	5.1	300	2440	90	13

[a] Johnson's FOM (JM) for the basic limit to device performance (high power and frequency)
[b] Keyes's FOM is based on the switching speed of the transistor.
[c] Quality factor 1 (thermal FOM) for heat sink material and the active device area in power device
[d] Quality factor 2 is based on perfect heat sinks
[e] Quality factor 3 is based on no assumptions about the sink materials or geometry
[f] Baliga's FOM for evaluation of high frequency application

Until recent years the development of SiC electronic devices was hindered by the material cost and the wafer growth technology. Small wafer size and the presence of point and extended defects were the major obstacles. Today, with these obstacles being steadily overcome, we observe a rapid development of the SiC technology and applications. Also, the capability to easily form several different crystal structures with different stacking sequence along a particular crystallographic direction, called polytypism (which will be addressed in more detail in chapter 1), has been an obstacle to grow electronic-grade SiC crystals. While there are known more than 200 different SiC polytypes, the industry is mainly focused on cubic (3C) and the

hexagonal 4H and 6H structures. 3C-SiC crystallises in the pure cubic structure, whereas 4H- and 6H-SiC present alternating hexagonally and cubically coordinated bilayers. In 4H-SiC, hexagonal and cubic bilayers follow one after the other, while in 6H-SiC, a hexagonal bilayer follows after two cubic bilayers. From these three polytypes only 4H- and 6H-SiC are produced in the form of bulk wafers, while 3C-SiC is not yet commercially available in this form. The material can be grown heteroepitaxialy on various substrate materials such as Si, with the disadvantage of being highly stressed due to the 20% lattice mismatch [Nishiguchi2004] or on 6H-SiC with several advantages such as insignificant lattice mismatch and identical chemical properties [Lebedev2006]. Nevertheless, despite significant progress in producing device-grade 3C-SiC epilayers in recent years, it is still necessary to further reduce the crystallographic structural defects during crystal growth before this polytype becomes a viable alternative to 4H- and 6H-SiC [Soueidan2007]. Irrespective of the SiC polytype, nitrogen or phosphorus are employed for *n*-type while aluminium or boron are used for *p*-type doping [Kimoto2015, Johnson2001]. Nitrogen occupies carbon sublattice sites, whereas aluminium, phosphorus and boron sit on the silicon sites. The dopant ionization energies depend on the lattice site, particularly in 4H- and 6H-SiC on whether the site is hexagonal or cubic [Ikeda1980].

In silicon (Si), many impurity atoms, in particular transition metals (TMs), form deep levels in the band gap and produce harmful effects like reduction of minority carrier lifetime [Graff2000]. The impurity atoms can be introduced to device regions from contaminated areas during the device manufacture process due to rapid diffusion. The most important and commonly used procedures to diminish the unwanted effects of the introduced deep levels are based on the so-called gettering techniques, where TMs are “gettered”, i.e. trapped, away from the active device areas [Graff2000, Myers2000]. TMs are a class of impurities that are also commonly found in bulk SiC samples and it is known that some of them, either in their isolated form or when in complexes with other defects, generate deep levels in SiC, changing its electrical properties and thus also having the potential of affecting the performance of devices [Lebedev1999, Baur1997, Assali2003]. However, gettering processes are largely absent in SiC processing, which poses the question why TMs have the potential to be so detrimental in Si devices but not in SiC. Although this question cannot be answered with certainty at the moment, for the simple fact that many of the basic properties of TMs in SiC, e.g. regarding their possible lattice sites, electrical levels, diffusion coefficients, solubilities, interactions with other defects, are still insufficiently known, it will be addressed again in the conclusions of this thesis.

Apart from possible detrimental behaviour, there are also desired effects of transition metal incorporation in semiconductors, especially regarding their magnetic doping. The classic

example is (Ga,Mn)As, which is known since the late 1990s to act as a so-called dilute magnetic semiconductor (DMS) at low temperatures [Hayashi1997]. In 2000 Dietl *et al*. predicted the room temperature (RT) ferromagnetism in Mn-doped ZnO single crystals, which triggered the search for DMS systems based on wide band gap semiconductors [Dietl2000]. Since then, TMs are being used intentionally as magnetic dopants in particular in wide band gap semiconductors such as ZnO, GaN and also SiC. Substitutional doping of SiC with transition metals (e.g. Cr, Mn, Fe) in order to produce a DMS has been considered in a number of publications [Dupeyrat2010, Bouziane2008, Miao2003, Takano2007, Machado2015]. An example where electrical properties of TMs are used beneficially in SiC, is the introduction of vanadium in order to compensate the excess of nitrogen, an undesirable electrically active impurity of semi-insulating SiC single-crystal growth process [Reshanov2000].

Whether being inherently present or intentionally introduced, TMs may play a decisive role in the performance of SiC semiconductor application devices. More specifically, the local structural configuration of the impurity atoms in the single-crystalline semiconductor lattice (i.e. the exact lattice location of the impurity) has a major influence on their electronic energy levels and spin state, determining the electronic, magnetic and optical properties of the doped semiconductor. In this thesis, a systematic study of the lattice site location of the radioactive TM impurities ^{56}Mn, ^{59}Fe, ^{65}Ni and ^{111}Ag in 3C- and 6H-SiC will be presented. Note that the focus on TMs is also due to the fact that for these elements are available as well established probes at ISOLDE, while for instance for the major electrical dopants of SiC - N, P, Al and B – radioactive beams are not available. However, one lattice location experiment was also performed with a potential acceptor dopant using the radioactive probe ^{124}In.

References

[Assali2003] L. V. C. Assali, W. V. M. Machado, J. F. Justo, "Transition metal impurities in 3C-SiC and 2H-SiC", *Physica* B **340–342** 116–120 (2003).

[Baliga1982] B. J. Baliga, "Semiconductors for high-voltage, vertical channel field effect transistors", *J. Appl. Phys*. **53** 1759–1764 (1982).

[Baliga1989] B. J. Baliga, "Power Semiconductor Device Figure of Merit for High-Frequency Applications", *IEEE Elect. Dev. Lett.* **10** 455–457 (1989).

[Baur1997] J. Baur, M. Kunzer, J. Schneider, "Transition metals in SiC polytypes, as studied by magnetic resonance techniques", *Phys. Stat. Sol.* (a) **162** 153–172 (1997).

[Bouziane2008] K. Bouziane, M. Mamor, M. Elzain, P. Djemia, S. M. Chérif, "Defects and magnetic properties in Mn-implanted 3C-SiC epilayer on Si(100): Experiments and first-principles calculations", *Phys. Rev.* B **78** 195305(1–7) (2008).

[Choyke2004] W. J. Choyke, H. Matsunami, G. Pensl (eds.), "Silicon Carbide: Recent Major Advances", Springer Verlag Berlin, Heidelberg, New York, 2004.

[Chow1994] T. P. Chow, R. Tyagi, "Wide band gap compound semiconductors for superior high-voltage unipolar power devices", *IEEE Trans. Elect. Dev*. **41** 1481-1483 (1994)

[Chow2004] T. P. Chow, N. Ramungul, J. Fedison, Y. Tang, "SiC power bipolar transistors and thyristors", in *Silicon Carbide: Recent Major Advances*, Springer Verlag Berlin, Heidelberg, New York, 2004, pp. 737–768.

[Dietl2000] T.Dietl, H. Ohno, F. Matsukura, J. Cibert, D. Ferrand, "Zener model description of ferromagnetism in zinc-blende magnetic semiconductors", *Science* **287** 1019–1022 (2000).

[Dupeyrat2010] C. Dupeyrat, A. Declémy, M. Drouet, A. Debelle, L. Thomé, Fe-implanted SiC as a potential DMS: X-ray diffraction and rutherford backscattering and channelling study", *Nucl. Instruments Methods Phys. Res.* B **268** 2863–2865 (2010).

[Graff2000] K. Graff, "Metal Impurities in Silicon-Device Fabrication", 2nd Edition, Springer Verlag Berlin, Heidelberg, New York, 2000.

[Ikeda1980] M. Ikeda, H. Matsunami, T. Tanaka, "Site effect on the impurity levels in 4H, 6H, and 15R SiC", *Phys. Rev*. B **22** 2842–2854 (1980).

[Ioffe] http://www.ioffe.ru/SVA/NSM/Semicond/

[Hayashi1997] T. Hayashi, M. Tanaka, T. Nishinaga, H. Shimada, "Magnetic and magnetotransport properties of new III-V diluted magnetic semiconductors: GaMnAs", *J. Appl. Phys.* **81** 4865-4867 (1997).

[Johnson1965] E. O. Johnson, “Physical limitations on frequency and power parameters of transistors”, *RCA Rev*. 163–177 (1965)

[Johnson2001] C. Johnson, N. Wright, M. Uren, K. Hilton, M. Rahimo, D. Hinchley, A. Knights, D. Morrison, A. Horsfall, S. Ortolland, A. O’Neill, “Recent progress and current issues in SiC semiconductor devices for power applications”, *IEEE Proc. - Circuits, Devices Syst*. **148** 101–108 (2001).

[Keyes1972] R. W. Keyes, “Figure of merit for semiconductors for high-speed switches” *Proceedings of the IEEE – Proceeding Letters* 225 (1971)

[Kimoto2015] T. Kimoto, “Material science and device physics in SiC technology for high-voltage power devices”, *Jpn. J. Appl. Phys.* **54** 040103(1–27) (2015).

[Lebedev1999] A. A. Lebedev, “Deep level centers in silicon carbide: A review”, Semiconductors **33** 107–130 (1999).

[Lebedev2006] A. A. Lebedev, “Heterojunctions and superlattices based on silicon carbide”, *Semicond. Sci. Technol.* **21** R17-R34 (2006).

[Machado2015] W. V. M. Machado, J. F. Justo, L. V. C. Assali, “Iron and manganese-related magnetic centers in hexagonal silicon carbide: A possible roadmap for spintronic devices”, *J. Appl. Phys.* **118** 045704(1–6) (2015).

[Miao2003] M. Miao, W. Lambrecht, “Magnetic properties of substitutional 3d transition metal impurities in silicon carbide”, *Phys. Rev*. B **68** 125204(1–10) (2003).

[Morkoç1994] H. Morkoç, S. Strite, G. B. Gao, M. E. Lin, B. Sverdlov, M. Burns, “Large-band-gap SiC, III-V nitride and II-VI ZnSe-based semiconductor device technologies”, *J. Appl. Phys*. **76** 1363–1398 (1994).

[Myers2000] S. M. Myers, M. Seibt, W. Schröter, “Mechanisms of transition-metal gettering in silicon”, *J. Appl. Phys.* **88** 3795–3819 (2000).

[Neudeck1994] P. G. Neudeck, “Progress towards high temperature, high power SiC devices”, *Institute of Physics Conference Series* **141** 1–6 (1994).

[Nishiguchi2004] T. Nishiguchi, M. Nakamura, K. Nishio, T. Isshiki, S. Nishino, “Heteroepitaxial growth of (111) 3C-SiC on well-lattice-matched (110) Si substrates by chemical vapor deposition”, *Appl. Phys. Lett*. **84** 3082–3084 (2004).

[Reshanov2000] S. A. Reshanov, “Growth and high temperature performance of semi-insulating silicon carbide”, *Diam. Relat. Mater*. **9** 480–482 (2000).

[Soueidan2007] M. Soueidan, G. Ferro, O. Kim-Hak, F. Robaut, O. Dezellus, J. Dazord, F. Cauwet, J. C. Viala, B. Nsouli, “Nucleation of 3C-SiC on 6H-SiC from a liquid phase” *Acta Mater.* **55** 6873–6880 (2007).

[Sze1981] S. M. Sze, N. N. Ng, “Physics of semiconductor Devices”, Appendix F, John Wiley & Sons 2nd Edition, New York, 1981, pp. 789.

[Takano2007] F. Takano, W. Wang, H. Akinaga, H. Ofuchi, S. Hishiki, T. Ohshima, “Characterization of Mn-doped 3C-SiC prepared by ion implantation” *J. Appl. Phys.* **101** 09N510(1–3) (2007).

[Trew1991] R. J. Trew, J. B. Yan, P. M. Mock, “The Potential of Diamond and SiC Electronic Devices for Microwave and Millimeter-Wave Power Applications”, *Proc. IEEE* **79** 598–620 (1991).

[Willander2006] M. Willander, M. Friesel, Q. ul Wahab, B. Straumal, “Silicon carbide and diamond for high temperature device applications”, *J. Mater Sci.: Mater. Electron.* **17** 1–25 (2006).

[Wright2008] N. G. Wright, A. B. Horsfall, K. Vassilevski, “Prospects for SiC electronics and sensors”, *Mater. Today* **11** 16–21 (2008).

Chapter 1

Silicon Carbide

1.1. Silicon Carbide – a brief history

The compund silicon carbide was first referred to in 1824 by the Swedish scientist, Jöns Jacob Berzelius with the suggestion that a silicon-carbon chemical bond could exist. A few decades later, in 1891, the American inventor Edward G. Acheson heated a mixture of clay and powdered coke (carbon), in an iron bowl, with the bowl and an ordinary carbon arc-light serving as the electrodes. Green crystals were found attached to the carbon electrode, which Acheson mistook as a new compound synthesized from carbon and alumina (Al_2O_3). The new compound was hence called carborundum, a name derived from the natural mineral form of alumina – corundum, which supposedly served as a starting material (present in the clay mixture) and carbon. Carborundum, represented by the chemical formula SiC, is an amorphous phase of silicon carbide and was found to be an abrasive material, with hardness only slightly below diamond. This discovery paved the way for the large-scale production of silicon carbide for the abrasive industry, which remains its main commercial use till today. SiC can also form naturally. However, it is an extremely rare mineral produced as supernova remnants or ejected from carbon rich red giant stars, reaching the earth trapped in meteorites. Moissanite is the name given to naturally formed SiC, in honor of the French chemist Henri Moissan who first discovered the mineral after examining rock samples from a meteor crater located in Canyon Diablo, Arizona in 1904 [Moissan1904]. In 1907, H. J. Round produced what turned out to be

the first Light Emitting Diode (LED) by applying 10 V to contacts placed on a SiC crystal, observing yellow, orange and green luminescence at the cathode [Round1907]. H. Baumhauer, in 1912, used for the first time the word "polytype" to describe the ability of SiC to crystallize into different forms, varying only in their stacking sequence in one direction. The possible use of SiC in the semiconductor industry created the need of high quality crystals. The beginning was made in 1955 by Lely, who developed a method of producing SiC crystals [Lely1955]. The growth of high quality SiC crystals produced by this method attracted the interest of many researchers and many pioneering works were published after that. However, a couple of decades later, SiC technology started to fade. The way towards SiC electronics on an industrial scale was blocked by the small produced wafer size (10 mm in diameter). At this point, Tairov and Tsvetkov in 1978 introduced a modification to the Lely process that opened the way towards controlled growth of bulk SiC crystals – the use of small SiC crystal grown with the Lely method as seed for their sublimation growth process [Tairov1973, Tairov1978, Tairov1981]. This growth technique was further improved by PhD students at the North Carolina State University, who in 1987 founded the company Cree Research Inc. [Cree], nowadays one of the largest suppliers of SiC devices.

The first SiC based product was completed in 1989 – the world's first blue light emitting diode, entering in production in the summer of 1990. Also, the first single crystal SiC wafers were commercially available in the beginnings of the 1990s. They were just an inch in diameter and used mostly for research. In later years, efforts were mainly focused towards the increase of the wafer size and improvement of the wafer quality, while decreasing the manufacture costs. To achieve this, several prerequisites had to be accomplished: (i) Japanese researchers introduced SiC vapor phase epitaxial (VPE) growth processes on Si substrates [Matsunami1981, Nishino1983, Kuroda1987, Kimoto1994]; (ii) further developments of epitaxial chemical vapor deposition (CVD) using a hot-wall setup [Kordina1995] and chloride based epitaxy [LaVia2014]; (iii) development of a new sublimation reactor labelled *high temperature* CVD, by Kordina *et al*. [Kordina1996].

These achivements resulted, for example, in the appearance of the first SiC Schottky diode commercially available in 2001 by Infineon and shortly after by Cree.

Today, 6 inch wafers in diameter are available, free of micropipe defects while further efforts are being made to reduce basal plane dislocation density in order to improve the characteristics of the produced electronic devices.

1.2. Silicon carbide – lattice structure

Silicon carbide is built up equally of silicon and carbon atoms. In this structure every atom is tetrahedrally surrounded by four atoms of the other species (CSi_4 or SiC_4) and is considered the smallest building element of any SiC lattice. The Si-C bond is very strong due to its short bond length (1.89 Å) and its sp^3 bond hybridization. The bond has nearly covalent character, however due to slightly different electronegativity values for carbon and silicon, a small ionic contribution of about 12% can be estimated from Pauling's formula to the SiC bond [Knippenberg1963]. The stacking of double layers (where one double layer is composed of one Si layer and one C layer), produces a close packed structure if the subsequent double layer (labeled B) is shifted with regard to the first double layer (labeled A), as seen in Fig. 1.1(a, b). The following layer can take the position of A again or a new one, labeled C. It is possible to have a longer stacking sequence, which in turn can give rise to a vast number of different structures (more than 200 different SiC polytypes are known). These structures are identified as different polytypes of SiC, where each polytype is characterized by the stacking sequence of layers A, B and C. For instance, stacking the layers in ABC order will produce the cubic zincblende structure, while the stacking sequence AB will produce the hexagonal wurtzite structure. Note that the stacking sequence always happens along a particular crystallographic direction, usually denominated c-axis (cf reference [Lebedev2006] for a good introduction into the subject). The resulting unit cell built from stacking the different bilayers, for both 3C- and 6H-SiC structures, can be found in Fig. 1.1(c, d). A commonly used notation is the Ramsdell notation [Ramsdell1947], describing each polytype with a number followed by a letter. The number denotes the count of double layers in the unit cell, and the letter stands for the symmetry, which can be cubic (C), hexagonal (H) or rhombohedral (R). As an example, the 2H-SiC polytype has a unit cell composed of 2 double layers with a stacking sequence AB, giving rise to hexagonal symmetry (wurtzite structure), where the local environment of each tetrahedron is purely hexagonal and labeled *h* after the Jagodzinski notation [Jagodzinski1949]. On the other hand, the 3C-SiC polytype has a unit cell composed of 3 double layers with a stacking sequence ABC, giving rise to cubic symmetry (zincblende structure).

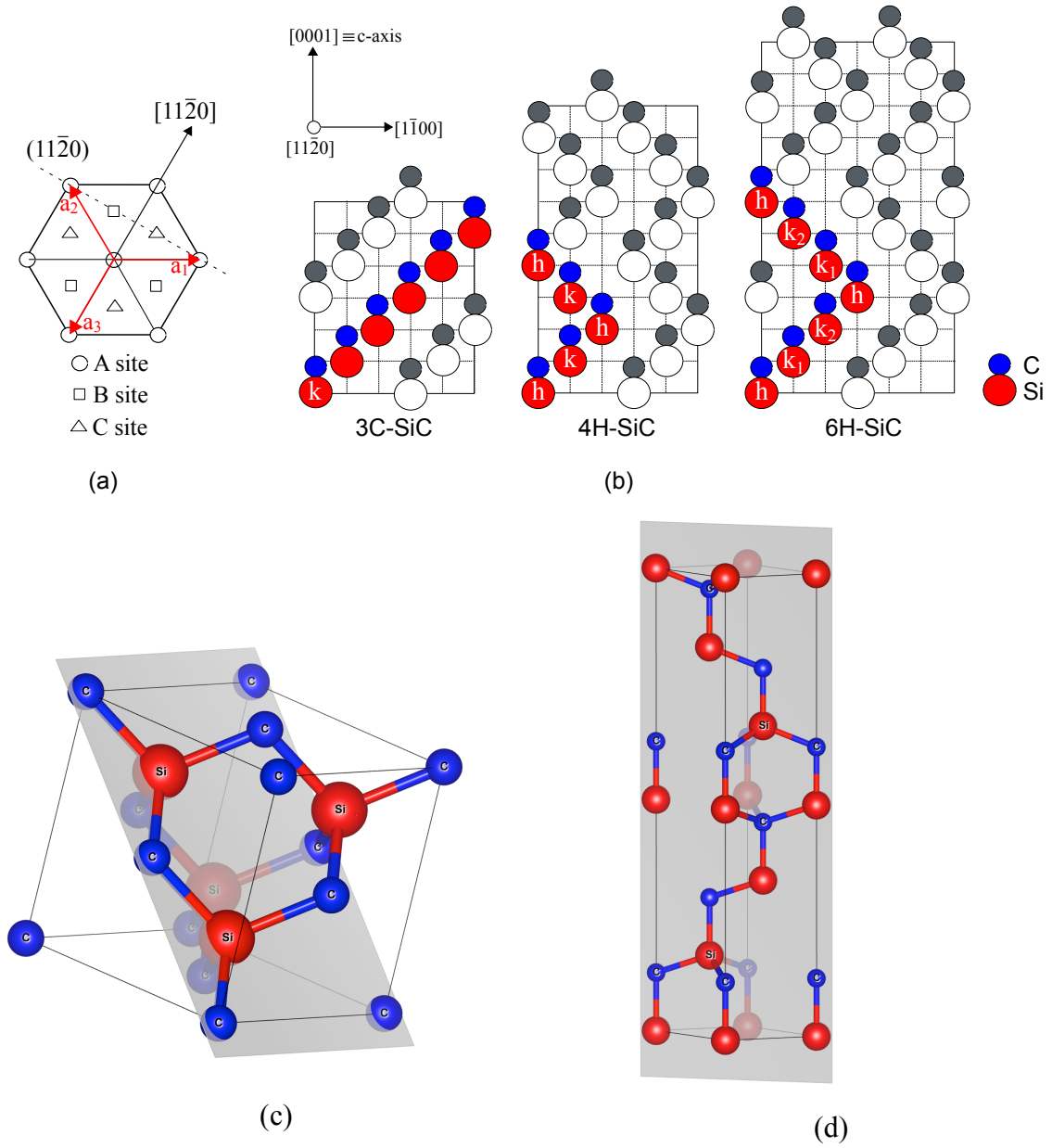

Figure 1.1. Crystalline structure of SiC: (a) the three possible stacking layers (A, B and C) with both (11$\underline{2}$0) plane and [11$\underline{2}$0] direction for guidance. The base vectors a_1, a_2 and a_3 in the basal plane of the hexagonal crystal structure are also marked in colour red. Crystal directions in hexagonal lattices are usually given in the form of four Miller-Bravais indices [hkil] which refer to the vectors a_1, a_2, a_3 and c. (b) shows the stacking sequence of three common SiC polytypes along the [0001] direction. The different cubic and hexagonal lattice sites are marked. The unit cells of (c) 3C-SiC and (d) 6H-SiC structures are also shown, drawn with VESTA software [Momma2011]. The silicon atoms are marked in red and the carbon atoms marked in blue. The planes {110} and {11$\underline{2}$0} are also identified by the gray colour.

This also means that the local environment of each tetrahedron is purely cubic and is labeled *k*. Other polytypes are mixtures of zincblende and wurtzite structures, such as 4H-, 6H- or 15R-SiC (the most common polytypes), and present lattice sites with both cubic and hexagonal environments. Depending on the stacking sequence, the fraction of hexagonal lattice sites in the unit cell, changes from 100% in 2H- to 50% in 4H- (one double layer *h* and one *k*), 33% in

6H- (layer *h* and layers k_1, k_2) and 0% in 3C-SiC.

The crystal directions in the cubic and in hexagonal polytypes are labelled differently. While in the cubic lattice the ordinary Miller indices are based on the Cartesian coordinates *x*, *y* and *z*, the directions in the hexagonal lattice are denoted by four digit Miller-Bravais indices in the way [*hkil*]. The three *hki* express components of a crystallographic direction with respect to multiples of the vectors a_1, a_2, and a_3 that are arranged at angles of 120° in the basal plane [see Fig 1.1(a)], while the value *l* is with respect to the base vector *c* parallel to the stacking direction of the crystal. While due to the constraint $h+k+i=0$ the index *i* is redundant, this notation is advantageous for the labelling of directions in hexagonal crystals, since the reference vectors for the coordinates a_i are parallel to the basis vectors of the crystal lattice. In particular, crystallographic axes and planes belonging to the same class are then easily recognizable since they can be expressed by simple cyclic permutation of the three Miller-Bravais sub-indices *hki*.

Table 1.1. Structural characteristics of common SiC polytypes (information regarding: (i) different SiC polytype space groups and corresponding lattice parameters were gathered from (a) [Landolt1987]; (ii) indirect energy band gap from (b) [Goldberg2001], (c) [Patrick1966] and (d) [Humphreys1981]).

Polytype	Space group[(a)]	a (Å)	c (Å)[(a)]	Indirect band gap (eV)	Hexagonality (%)
3C	T^2_d-F$\underline{4}$3m	4.36	4.36	2.3[(b)]	0
2H	C^4_{6v}-P6$_3$mc	3.08	5.05	3.3[(c)]	100
4H	C^4_{6v}-P6$_3$mc	3.08	10.05	3.2[(b)]	50
6H	C^4_{6v}-P6$_3$mc	3.08	15.12	3.0[(b)]	33
15R	C^5_{3v}-R3m	3.08	37.7	3.0[(d)]	40

In general, different polytypes have widely ranging physical properties [Bechstedt1997], therefore SiC can be thought of a whole class of materials. For instance, all of the 200 known polytypes have an indirect energy band gap (E_g), but it varies over a wide range from 2.3 eV (3C) to 3.3 eV (2H) as the hexagonality increases from 0% to 100%. The empirical Choyke-Hamilton-Patrick relation predicts a linear relationship between the band gap E_g and the degree of hexagonality up to 50% [Choyke1964], which states that E_g increases for polytypes with increasing amount of hexagonal sites. It was observed for 2H-SiC, which has a hexagonality degree of 100%, that if it followed the empirical relation, it would present a E_g higher than the measured value of 3.3 eV. Backes *et al*. tried to theoretically explain this relation by a one-dimensional Kronig-Penney like model [Backes1996], being successful only for SiC polytypes with hexagonality below 50%.

The polytypism affects the properties of point defects in the various SiC modifications, as will be discussed in more detail in the next sections of this chapter. One point is the difference

between cubic and hexagonal sites. Taking as an example the carbon atom in the center of Fig. 1.2, the local environment, i.e. the nearest neighbour shell surrounding it, is identical. This changes for the second neighbour shell. The carbon atoms which are the second neighbours to the central carbon atoms depicted in Fig. 1.2 are rotated by 60° between the cubic site and the hexagonal site. This different second-neighbour environment will result in point defects that will introduce different energy levels in the crystal host band gap, depending on whether they are cubic or hexagonal.

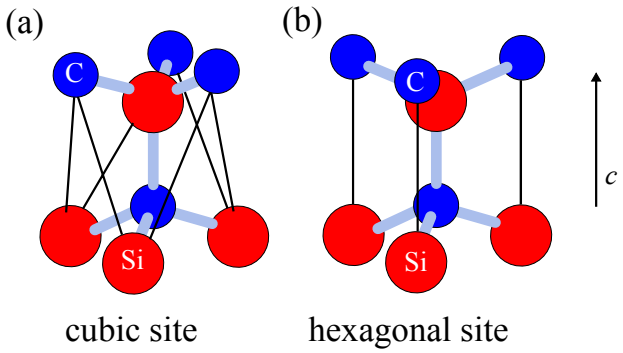

Figure 1.2. Local geometry of a carbon atom at (a) the cubic and (b) the hexagonal site. The upper carbon layer is rotated by 60° between these two configurations, which is indicated by the lines connecting the upper and the lower bi-layer. Note that the same is true for the local geometry of a silicon atom.

1.3. Doping of SiC

Doping a semiconductor material during the crystal growth process is a common technique to achieve large-area homogeneously doped wafers with well-controlled impurity concentration. It is also common to selectively dope a certain region of the semiconductor material in order to change its electrical properties in that region. This is important when building an electronic device. When in operation, these different regions have different tasks. Some improve the conduction of electrons through the device, some serve as contacts to the device exterior and some as a buffer or high resistance between conducting areas.

Since many decades silicon is the most important semiconductor material in use. While initially Si devices requiring selectively doped regions had to rely on dopant diffusion, since the early 1970s ion implantation has become the main doping process in silicon-based microelectronics. It allows a precise control over the dopant depth profiles since the depth and shape are mainly determined by factors such as dopant ions impinging energy, the dopant ion atomic mass and charge and the implant fluence. As a result, for typical Si based applications, around 40-60 ion-implantation steps using as many as 20 implant species, ranging usually between few hundred eV to several MeV, and ion-fluences from order 10^{11} cm^{-2} to order 10^{16} cm^{-2}, are used. The ion-implantation steps have several objectives: primarily doping, threshold-voltage adjustment and diffusion control, e.g. pre-amorphization and/or co-implantation [Elliman2015]. It is possible to accurately model the distribution of the dopant ions in the substrate, which is convenient for device designers and results in devices with reproducible and reliable semiconduting properties. Also, dopants can be introduced at concentrations exceeding their solid solubility limit in the target material because ion implantation is a nonequilibrium process.

Concerning SiC, the story is different. The close packed stacking and the short bond lenght of the Si-C layers hinder the efficient diffusion of dopants/impurities at low temperatures, leading to negligible dopant diffusion at temperatures below 1800 °C, as can be seen in Table 1.2, where a summary of diffusion data in SiC is presented. Only small atoms like hydrogen, lithium and boron have a comparably fast migration in SiC [Linnarsson1999, Rüschenschmidt2001, Svensson1998]. Due to the need to have temperatures that exceed 2000 °C, thermal diffusion cannot be considered as a practical doping process for SiC.

Table 1.2. Activation energy and effective diffusion coefficients for various impurities in SiC. The self-diffusion coefficients for SiC are also included.

Material	Dopant	Act. energy (eV)	Effective diffusion coefficient		Temperature range (°C)
			Fast branch (cm^2s^{-1})	Slow branch (cm^2s^{-1})	
SiC	N	7.6–9.3	-	5×10^{-12}	1800–2450
	B	5.1–5.5	2×10^{-9}–1×10^{-7}	2.5×10^{-13}–3×10^{-11}	1800–2300
	Al	4.9–6.1	-	3×10^{-14}–6×10^{-12}	1800–2300
	H	3.5	$\sim10^{-14}$		800
	Li	2.1	$\sim3\times10^{-14}$		700
	Si	7.6	1×10^{-16}–1×10^{-14}		2000–2200
	C	7.6	7.4×10^{-16}–3.9×10^{-14}		2100–2350

However, ion implantation causes damage to the crystal structure, depending on the mass, energy and flux density of the implanted ion, the material and its temperature and total implantation fluence. To reduce the induced damage and to electrically activate the implanted dopant species, high temperature post-irradiation annealing has to be performed, and an often used rule of thumb is that roughly temperatures of ~2/3 of the melting temperature (in K) are required for removal of extended defects [Williams1998]. Hence, in this case the high temperature stability of SiC is a disadvantage since the implantation process also produces high temperature stable defects that will be very difficult to remove by the annealing process. According to the above rule one estimates from the SiC melting temperature of 2730 °C that annealing temperatures around 2000 °C should be required. Experimentally, annealing around 1500 °C-1700 °C has been reported to result in electrical activation of implanted dopants that is sufficient for the use in devices, altough not all defects are removed at this temperature [Elliman2015, Hallén2016].

1.4. Common shallow dopants used in SiC

For the *n*- or *p*-type doping in SiC, elements of the VA or IIIA group of the periodic table are used respectively. Aluminium and boron are the most commonly used *p*-type dopants, while for *n*-type doping, nitrogen and phosphorus are the usual choices.

Each dopant will produce a different ionization energy state depending on whether it sits on the cubic or hexagonal site and also on the dopant concentration in the material [Ikeda1980, Pensl1993, Ivanov2005, Kimoto2015]. The size of the dopants in comparison to Si and C will

define their positions inside the SiC lattice. The Si lattice atoms will be substituted by Al and P atoms, while C lattice atoms by N. Boron was initially reported to occupy the C-site [Woodbury1961], however this was later revised by Zubatov *et al*. who found it to be incorporated only in Si-sites [Zubatov1985]. Theoretical considerations [Bockstedte2001, Deák2003] point out that both sites are possible but result in shallow (B_{Si}) or deep acceptors (B_C), respectively, although for the B deep acceptor also more complicated models have been proposed, cf. the remarks below. The site preference of specific dopants can be used, for example, during SiC epitaxial growth by choosing Si- or C-rich growth conditions in order to facilitate or hinder the dopant incorporation, as described in detail by Larkin *et al*. [Larkin1997]. Several authors, throughout the years, using different techniques, such as Fourier-transform far-infrared absorption, Raman scattering, photothermal ionization spectroscopy, photoluminescence of donor-acceptor pairs, or Hall-effect measurements, determined the ionization energies for these dopants. In the 3C-SiC cubic structure all sites are equivalent and so only one shallow donor (in the nitrogen or phosphorus case), and one shallow acceptor (for aluminium or boron), exists. Regarding the hexagonal structures, caution has to be taken due to the existence of inequivalent sites (hexagonal versus cubic configuration). Nitrogen, which replaces carbon, introduces two shallow donor levels in 4H-SiC and three donor levels in 6H-SiC (corresponding to the hexagonal (*h*) and cubic (*k*) lattice sites for 4H-SiC, and cubic (k_1, k_2) for 6H-SiC); the same is observed for the acceptor levels of aluminium, which resides on Si-lattice sites [Ikeda1980, Pensl1993, Ivanov2005]. Boron presents both shallow and deep B levels, with ionization energies of ~300 meV [Smith1999] and ~650 meV [Ikeda1980], respectively. With respect to the deep B acceptor the calculations of Bockstedte *et al*. suggest B_C as most likely candidate [Bockstedte2001], while also B_{Si} in complexes with an intrinsic defect has been proposed, e.g. $B_{Si}Si_C$ from theory [Aradi2001], or $B_{Si}V_C$ [Duijn1998] from experimental electron paramagnetic resonance and electron-nuclear double resonance (ENDOR) results. Phosphorus, just like nitrogen, can be used as a shallow dopant in SiC and, depending on the desired semiconductor properties, can be considered as a better alternative. As an example, phosphorus is the recommended dopant to use when producing highly doped *n*-type SiC. Nitrogen levels in as-grown SiC can be varied from 10^{14}-10^{16} cm^{-3} for not intentionally doped SiC (depending on growth technique) [Huh2006, Kimoto2015], up to 6×10^{18}-1.2×10^{19} cm^{-3} for the intentionally doped ones. However, it was found that even in N-implanted SiC there is a critical concentration of 2-5×10^{19} cm^{-3}, which represents an upper limit for electrically active N donors [Laube2002]. The saturation of the electrical activation above

this concentration limit is explained by the preferential incorporation of nitrogen into electrically inactive N-vacancy complexes [Gerstmann2003, Bockstedte2004a, Schmid2006]. On the other hand, almost complete electrical activation was observed for an ion-implanted phosphorus concentration up to 3×10^{20} cm^{-3} [Laube2002]. Bockstedte *et al*. also predicted that the formation of complexes between phosphorus and vacancies only becomes relevant at dopant concentrations above this value [Bockstedte2004a].

Table 1.3 presents a summary of measured ionization energy values for the most common dopants used in three different SiC polytypes. As already mentioned, one of the major difficulties that hinders the pratical use of SiC is the large dopant ionization energies. So, other dopants that introduce shallow energy levels with low ionization energies are strongly desired. As an example, Itoh *et al*. showed the effect of coimplantation of carbon and boron ions on the electrical activation of boron acceptors in 4H-SiC by using Hall effect and photoluminescence measurements [Itoh1998]. Miyata *et al*. [Miyata2008] investigated the ionization energies of several substitutional group-II, III, V and VI impurity atoms in 4H-SiC. His calculations suggest that antimony (group-V donor dopant), introduces a much shallower donor level when compared with the more conventional *n*-type dopants such as nitrogen and phosphorus, and as well that indium should be an acceptor with $E_a(Si_h)$ ~150 meV and $E_a(Si_k)$ ~260 meV in 4H-SiC, i.e. comparable to Al. Other possible dopants such as gallium and indium are also discussed briefly in the review by Lebedev *et al*. [Lebedev1999]. Whereas for the gallium acceptor ionization energies of 0.29 eV (6H), 0.3 eV (4H and 15R) and 0.34 eV (3C) are mentioned, it is stated that it was not possible to obtain *p*-type SiC from doping with indium during growth.

Table 1.3. Measured ionization energies for the most common donor and acceptor SiC dopants in cubic-like (*k*) and hexagonal-like (*h*) sites.

		Ionization energy (meV)				
	Site	N	Al	B	P	Reference
3C	*k*	56.5	254	735		[Ikeda1980]
		54.2				[Moore1993]
4H	*k*	124	191	647		[Ikeda1980]
	h	66				
	k	100				[Evwaraye1996]
	h	53				
	h	61.4	199(±2)			[Ivanov2005]
	k	125.5	201.3		60.7	[Ivanov2005]
	h	61.4	197.9		120(±20)	
	k		266			[Smith1999]
	h		212			
6H	*k*	155	249	723		[Ikeda1980]
	h	100	239	698		
	k_1			310		[Smith1999]
	k_2			380		
	h			270		
	k_1	137.6				[Suttrop1992]
	k_2	142.4				
	h	82.7				
	k	140				[Raynaud1994]
	h	82				

1.5. Transition metals in SiC

Transition metal (TM) impurities are invariably found in bulk samples of SiC [Schneider1993, Lebedev1999] due to the production processes normally employed. It is known that those impurities, either in isolated form or when in complexes with other defects, generate electrically active levels deep in the band gap of SiC [Lebedev1999, Baur1997, Assali2003]. The presence of deep-level defects as efficient carrier traps can seriously affect the performance of some semiconductor devices, which depend on long minority carrier lifetimes. On the other hand, using intentional doping with TM atoms, one can also beneficially vary the electrical, optical and magnetic properties of SiC.

The most studied TMs in SiC are titanium (Ti), vanadium (V), chromium (Cr) and tungsten (W). Ti, Cr, and V are dominant background impurities due to their presence in parts of SiC

growth (both sublimation and epitaxial CVD) reactors. The introduction of vanadium compensates the excess of nitrogen, an undesirable electrically active impurity in the growth process of semi-insulating SiC (SI-SiC) single-crystals [Reshanov2000], and was used for metal-semiconductor-field-effect transistor (MESFET) structures. In order for a semiconductor to be semi-insulating, the Fermi level should be pinned to the middle of the band gap. Vanadium is an electrically amphoteric impurity in SiC, which means that it can act as either a donor or an acceptor depending on the Fermi level position. In 6H-SiC, vanadium acceptor and donor levels are located at $E_C - (0.6\text{-}0.8\ \text{eV})$ and $E_C - (1.35\text{-}1.42\ \text{eV})$, respectively [Maier1992, Kunzer1995, Sudarshan1997, Mitchel1998, Lebedev1999], Fig. 1.3. According to the empirical 'Langer-Heinrich rule' [Langer1985], the levels in 4H-SiC are located deeper in the band gap: E_C–0.97 eV [Lebedev1999] for acceptor and E_C–1.42 eV [Mitchel1998] for donor states. The 'Langer-Heinrich rule' was established for transition metals in III-V and II-VI compound semiconductors and assumed valid for SiC polytypes. This rule states that energy levels of the transition metals are aligned within a group of isovalent compound semiconductors with respect to a common reference level. Dalibor *et al*. [Dalibor1997] and Achtziger *et al*. [Achtziger2004] concluded that deep levels related to the investigated TMs (Ti, Cr, V, Ta and W) in 4H-, 6H- and 3C-SiC follow the 'Langer-Heinrich rule' as well. The calculations of Miao *et al*. [Miao2003, Miao2006] found Mn, located at Si site, to be also amphoteric with acceptor and donor levels located at $E_C - (0.68\text{-}0.70\ \text{eV})$ and $E_C - (1.38\text{-}1.47\ \text{eV})$ respectively, and consequently a good candidate for making semi-insulating 4H-SiC. The same author also calculated the Fe and Ni energy levels located at Si site and found it deep in the 3C-SiC band gap, E_C–1.60 eV and $E_C - (0.75\text{-}1.10\ \text{eV})$ respectively. Excluding the early 3d TMs (Sc, Ti V and Cr), little is known about the energy level values for Mn, Fe and Ni in SiC band gap, a striking contrast when compared with the available literature about TMs in silicon semiconductors.

Substitutional doping with transition metals (e.g. Cr, Mn, Fe) has also been considered in the context of dilute magnetic semiconductors [Miao2003, Takano2007, Bouziane2008, Dupeyrat2010, Machado2015].

Currently, hardly any experimental data exist on the preferential lattice sites that TM impurities occupy in any of the SiC polytypes, while several theoretical studies have addressed this subject. Reference [Machado2015] finds that Mn and Fe in 2H-SiC "…are energetically more favorable in lattice sites with carbon atoms as their first nearest neighbours, in both substitutional and interstitial configurations, which results from the larger electronegativity of carbon with respect to that of silicon"; in the case of Fe in 3C-SiC similar site preferences were

also suggested in reference [Wright2016]. While references [Miao2003, Takano2007, Machado2015, Wright2016, Medvedeva2003] investigated most TMs in 3C-SiC, including Mn, Fe and Ni, only substitutional sites were addressed, of which the Si sites were considered most stable. On the other hand, reference [Gubanov2001] predicts that Cr, Fe and Co should predominantly occupy C sites while Mn should prefer to be found on Si sites. Moreover, entirely different lattice sites might also be found. For instance, the existence of mixed divacancies V_{Si}-V_C is reported in references [Kawasuso1996, Brauer1996, Oshima2001]. While one expects that single vacancies V_{Si} or V_C might trap interstitial TM atoms on substitutional Si or C sites, divacancies V_{Si}-V_C might trap TMs in V_{Si}-TM-V_C complexes where the position of the TM may correspond to the bond-center (BC) site in an undisturbed lattice. Such types of complexes have been suggested to be one of the most commonly found for ion implanted TMs in Si [Wahl2005, Wahl2006, Silva2013, Silva2014, Silva2016].

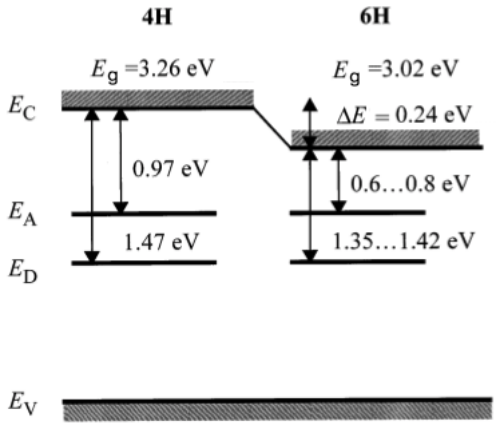

Figure 1.3. Vanadium band gap states in 4H- and 6H-SiC. E_C and E_V stands for conduction band and valence band respectively; E_A and E_D stands for acceptor and donor levels, respectively. Figure adopted from [Reshanov2000].

1.6. Point defects in SiC

The nature of SiC as a binary compound combined with the existence of inequivalent lattice sites in different polytypes give rise to a large variety of possible defects, which can be classified as follows:

(i) a vacancy, when an atom is removed from its original lattice site, either silicon vacancy (V_{Si}) or carbon vacancy (V_C). The electronic properties of both vacancies were discussed in detail by Zywietz *et al*. [Zywietz1999] and Torpo *et al*. [Torpo2001]. Their structure and annealing behavior were described based on the results obtained by Itoh *et al*. using ESR and PAS techniques [Itoh1997].

(ii) an interstitial, when an atom occupies a site that is not a regular substitutional lattice position. The interstitial atom can be the same species as the host lattice (then it is called self-interstitial), or a foreign atom (called an interstitial impurity). A silicon (carbon) interstitial is designated as Si_i (C_i), respectively. Several different types of interstitial sites exist in SiC: tetrahedrally coordinated sites with either four carbon or silicon neighbors (commonly represented by T_C and T_{Si}, respectively), hexagonal, bond-centered and <100>- or <110>-oriented split-interstitials. As the name implies, a bond-center interstitial is located at the center of the bond of two lattice atoms. In a Si split-interstitial, two silicon atom share one Si lattice site forming a displaced pair. Concerning the Si interstitials, they were investigated by several authors [Wang1988, Bockstedte2000, Mattausch2001,Bockstedte2004c] and the conclusion was reached that the hexagonal and bond-center sites are unstable, whereas the tetrahedrally carbon coordinated interstitial and the <110>-oriented split interstitial were found to be dominant. Similar sites are available for the carbon interstitials as for the silicon ones. Detailed analysis done by Bockstedte *et al* and Gao *et al*. for 3C-SiC showed that the carbon <100>-oriented split-interstitial at the carbon and silicon site are the most abundant, with the one at carbon site the most favorable [Bockstedte2004c, Gao2001].

(iii) pairs of vacancies and self-interstitials. A so-called Frenkel pair is formed when a vacancy is located close to a self-interstitial. Depending on the distance that separates the vacancy from the interstitial, their recombination proceeds in two steps: (1) diffusion limited motion of the vacancy and interstitial towards one another and (2) the recombination of the pair by a direct hop of the insterstitial into the vacancy. The first step is diffusion-limited and is described by the energy barrier

for migration of either the interstitial or the vacancy. A detailed study made by Bockstedte *et al*. about this subject, using ab initio methods based on density functional theory, can be found in reference [Bockstedte2004b].

(iv) an antisite, when an atom of one sublattice is placed on the other sublattice, either silicon antisite (Si_C) or carbon antisite (C_{Si}).

(v) a foreign impurity atom, occupying a regular site. For instance, an aluminium atom in a Si site (Al_{Si} as an acceptor), or a nitrogen atom in a C site (N_C, as a donor).

(vi) Combinations of these simple point defects are also possible, such as the vacancy-antisite complex. This kind of complex is relevant for the migration of the vacancies, in particular the V_C-C_{Si} complex, which is related to the metastability of the V_{Si} in *p*-type and intrisinc (compensated) material, as it will be seen in chapter 3. The simplest vacancy-antisite complex is created by exchanging the position of the vacancy with one of its nearest neighbors. As a result, the properties of the original vacancy dramatically change. It is transformed into a vacancy on the other sublattice and a neighboring antisite. The Si vacancy-antisite complex, which is related to the carbon vacancy ($V_C \rightarrow V_{Si}$-Si_C) is, according to the 3C-SiC study of Bockstedte *et al.*, unstable in all relevant charge states [Bockstedte2000]. On the other hand, the $V_{Si} \rightarrow V_C$-C_{Si} is energetically more favorable than the V_{Si} in *p*-type or intrinsic (compensated) SiC, whereas in *n*-type material V_{Si} is the more stable configuration. This metastability was also studied by Rauls *et al*. [Rauls2000] for the neutral pair in 4H-SiC using a DFT based tight binding method. Also, Lingner *et al.* suggested the V_C-C_{Si} complex as the only defect able to explain all experimental findings in neutron irradiated 6H-SiC [Lingner2001]. The formation energies of V_{Si} and V_C-C_{Si} as a function of the Fermi level are plotted in Fig. 1.4 for 3C- and 4H-SiC, where the significant energy gain yielded by the transformation of the vacancy to the corresponding vacancy-antisite complex is visible. Only for a Fermi level position above 1.7 eV (3C) and 2.0 eV (4H), a stable V_{Si} is obtained.

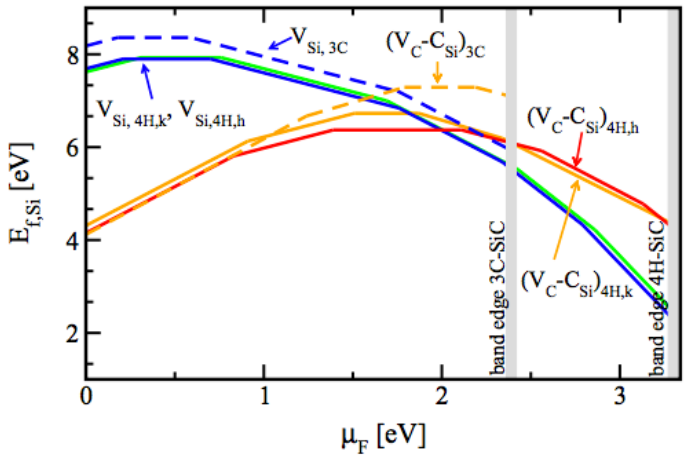

Figure 1.4. Formation energy of the silicon vacancy V_{Si} and the carbon vacancy-antisite V_C-C_{Si} for 3C- and 4H-SiC. The experimental energy band edges of both polytypes are indicated by vertical bars. The subscripts refer to the polytype and the cubic and hexagonal lattice site (*k* and *h* respectively). Figure adopted from reference [Bockstedte2004c].

Defects created by the presence of foreign atoms are called extrinsic defects. These are for example donors or acceptors, or foreign interstitials. On the other hand, defects arising through the rearrangement of the host atoms of the original lattice are called intrinsic defects. These could be self-interstitials, vacancies or antisites. Also, in complex defects both intrinsic and extrinsic defects can be mixed together. For example, as mentioned before, V_{Si}-V_C divacancies, C_{Si}-V_C, Si_C-V_{Si} vacancy-antisite pairs, X-V_{Si}, X-V_C, V_{Si}-X-V_C vacancy-impurity pairs (where X represents an impurity), or even more complex defects can be formed. All these defects can occupy both cubic and hexagonal sites in mixed-structure SiC polytype, e.g. (C_{Si}-V_C)(*h*) and (C_{Si}-V_C)(*k*) can exist in 4H-SiC, or V_C(*h*), V_C(k_1) and V_C(k_2) in 6H-SiC.

As was mentioned already, inequivalent lattice sites in SiC can give rise to, for example, different ionization energies with the same atom species of substitutional donor or acceptor atoms. Properties of intrinsic point defects are generally also site dependent. Defects, occupying both *k* and *h* sites have corresponding different energy levels in the band gap, which usually can be detected by optical or electron paramagnetic resonance (EPR) techniques.

A theoretical defect study in cubic SiC, with silver as an impurity, exists in the literature. Shrader *et al.* studied Ag interstitial and substitutional defects, including Ag-vacancy defect clusters and calculated their respective formation energies, Fig. 1.5. From all defects considered, the defect complex $(Ag_{Si}\text{-}V_C)^{-1}$ has the lowest formation energy 3.46 eV [Shrader2011].

It is worth noting that generation of defects, as lattice imperfections is usually accompanied by the relaxation of the surrounding atoms, in order to attain the minimum-energy configuration. Either inward or outward relaxation can occur around the defect center, resulting in a volume

change of the tetrahedron defined by the nearest-neighbour atoms. As an example, Stockmeier *et al*. [Stockmeier2009] studied the variations of the a- and c-lattice constants as a function of the incorporated nitrogen, boron and aluminum in bulk 6H-SiC crystals. The autor reported that aluminum increased both the a- and c-lattice parameters, while boron had the opposite effect, and nitrogen incorporation resulted in an increase of the 6H-SiC lattice along the c-axis direction but a decrease along the a-axis.

Lattice deformation caused by the presence of dopants can be responsible for the appearance of stress during the growth and formation of defects. Ohshige *et al*. [Ohshige2014] reported this effect during the initial stage of physical vapor transport (PVT) growth of 4H-SiC due to the presence of residual nitrogen in the seed SiC.

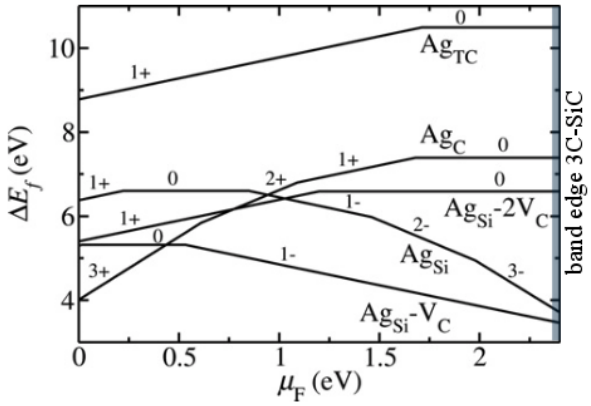

Figure 1.5. Formation energy of the most stable silver defects in 3C-SiC. The energy values are for Si-rich conditions. The experimental energy band gap edge is indicated by the gray vertical bar. Figure adopted from reference [Shrader2011].

References

[Achtziger2004] N. Achtziger, W. Witthuhn, "Radiotracer deep level transient spectroscopy", in *Silicon Carbide: Recent Major Advances*, Springer Verlag Berlin, Heidelberg, New York, 2004, pp. 537–561.

[Aradi2001] B. Aradi, A. Gali. P. Deak, E. Rauls, T. Frauenheim, N. T. Son, "Boron centers in 4H-SiC", *Mater. Sci. Forum* **353-356** 455–458 (2001).

[Assali2003] L. V. C. Assali, W. V. M. Machado, J. F. Justo, "Transition metal impurities in 3C-SiC and 2H-SiC", *Physica* B **340–342** 116–120 (2003).

[Backes1996] W. H. Backes, F. C. de Nooij, P. A. Bobbert, W. van Haeringen, "Kronig-Penney-like description for band gap variation in SiC polytypes", *Physica.* B **217** 207-211 (1996).

[Baur1997] J. Baur, M. Kunzer, J. Schneider, "Transition metals in SiC polytypes, as studied by magnetic resonance techniques", *Phys. Stat. Sol.* (a) **162** 153–72 (1997).

[Bechstedt1997] F. Bechstedt, P. Käckell, A. Zywietz, K. Karch, B. Adolf, K. Tenelsen, J. Furthmüller, "Polytypism and properties of Silicon Carbide", *Phys. Stat. Sol*. (b) **202** 35–62 (1997).

[Bockstedte2000] M. Bockstedte, O. Pankratov, "*Ab initio* study of intrinsic point defects and dopant-defect complexes in SiC: application to boron diffusion", *Mater. Sci. Forum* **338–342** 949–952 (2000).

[Bockstedte2001] M. Bockstedte, A. Mattausch, O. Pankratov, "Boron in SiC: structure and kinetics", *Mater. Sci. Forum* **353-356** 447–450 (2001).

[Bockstedte2004a] M. Bockstedte, A. Mattausch, O. Pankratov, "Solubility of nitrogen and phosphorus in 4H-SiC: a theoretical study", *Appl. Phys. Lett*. **85** 58–61 (2004).

[Bockstedte2004b] M. Bockstedte, A. Mattausch, O. Pankratov, "*Ab initio* study of the annealing of vacancies and interstitials in cubic SiC: vacancy-interstitial recombination and aggregation of carbon interstitials", *Phys. Rev*. B **69** 235202(1–13) (2004).

[Bockstedte2004c] M. Bockstedte, A. Mattausch, O. Pankratov, "Defect migration and annealing mechanisms", in *Silicon Carbide: Recent Major Advances*, Springer Verlag Berlin, Heidelberg, New York, 2004, p. 27–54.

[Bouziane2008] K. Bouziane, M. Mamor, M. Elzain, P. Djemia, S. M. Chérif, "Defects and magnetic properties in Mn-implanted 3C-SiC epilayer on Si(100): Experiments and first-principles calculations", *Phys. Rev.* B **78** 195305(1–7) (2008).

[Brauer1996] G. Brauer, W. Anwand, P. Coleman, A. Knights, F. Plazaola, Y. Pacaud, W.

Skorupa, J. Störmer, P. Willutzki, “Positron studies of defects in ion-implanted SiC”, *Phys. Rev.* B **54** 3084–3092 (1996).

[Choyke1964] W.J. Choyke, D.R. Hamilton, L. Patrick, “Optical properties of cubic SiC: Luminescence of nitrogen-exciton complexes, and interband absorption”, *Phys. Rev*. **133** A1163–1166 (1964).

[Cree] http://www.fundinguniverse.com/company-histories/cree-inc-history/

[Dalibor1997] T. Dalibor, G. Pensl, H. Matsunami, T. Kimoto, W. J. Choyke, A. Schöner, N. Nordell, “Deep defect centers in silicon carbide monitored with deep level transient spectroscopy”, *Phys. Stat. Sol*. (a) **162** 199–225 (1997).

[Deák2003] P. Deák, B. Aradi, A. Gali, U. Gerstmann, “Some like it shallower – *p*-type doping in SiC”, *Phys. Stat. Sol*. (b) **235**(1) 139–145 (2003)

[Duijn1998] A. v. Duijn-Arnold, T. Ikoma, O. G. Poluektov, P. G. Baranov, N. Mokhov, J. Schmidt, “Electronic structure of the deep boron acceptor in boron-doped 6H-SiC”, *Phys. Rev*. B **57** 1607–1619 (1998).

[Dupeyrat2010] C. Dupeyrat, A. Declémy, M. Drouet, A. Debelle, L. Thomé, “Fe-implanted SiC as a potential DMS: X-ray diffraction and rutherford backscattering and channelling study”, *Nucl. Instruments Methods Phys. Res.* B **268** 2863–2865 (2010).

[Elliman2015] R. G. Elliman, J. S. Williams, “Advances in ion beam modification of semiconductors”, *Current Opinion in Solid State and Materials Science* **19** 49–67 (2015).

[Evwaraye1996] A. O. Evwaraye, S. R. Smith, W. C. Mitchel, “Shallow and deep levels in *n*-type 4H-SiC”, *J. Appl. Phys*. **79** 7726–7730 (1996).

[Gao2001] F. Gao, E. J. Bylaska, J. Weber, L. René Corrales, “*Ab initio* and empirical-potential studies of defect properties in 3C-SiC”, *Phys. Rev*. B **64** 245208(1–7) (2001).

[Gerstmann2003] U. Gerstmann, E. Rauls, Th. Frauenheim, H. Overhof, “Formation and annealing of nitrogen-related complexes in SiC”, *Phys. Rev*. B **67** 205202(1–7) (2003).

[Goldberg2001] Y. Goldberg, M.E. Levinshtein, S. L. Rumyantsev, “Properties of advanced semiconductor materials GaN, AlN, SiC, BN, SiGe”, M. E. Levinshtein, S. L. Rumyantsev, M. S. Shur (Eds.), John Wiley & Sons Inc., New York, 200,1 pp. 93–148.

[Gubanov2001] V. A. Gubanov, C. Boekema, C. Y. Fong, “Electronic structure of cubic silicon-carbide doped by 3d magnetic ions“, *Appl. Phys. Lett.* **78** 216–218 (2001).

[Hallén2016] A. Hallén, M. Linnarsson, “Ion implantation technology for silicon carbide”, *Surface & Coatings Technol.* **306** 190–193 (2016).

[Huh2006] S. W. Huh, H. J. Chung, S. Nigam, A. Y. Polyakov, Q. Li, M. Skowronski, E. R.

Glaser, W. E. Carlos, B. V. Shanabrook, M. A. Fanton, N. B. Smirnov, "Residual impurities and native defects in 6H-SiC bulk crystals grown by halide chemical-vapor deposition", *J. Appl. Phys*. **99** 013508(1–11) (2006).

[Humphreys1981] R. G. Humphreys, D. Bimberg, W. J. Choyke, "Wavelength modulated absorption in SiC", *Solid State Commun*. **39** 163–167 (1981).

[Ikeda1980] Ikeda, M., H. Matsunami, T. Tanaka, "Site effect on the impurity levels in SiC", *Phys. Rev*. B **22** 2842–2854 (1980).

[Itoh1997] H. Itoh, A. Kawasuso, T. Ohshima, M. Yoshikawa, I. Nashiyama, S. Tanigawa, S. Misawa, H. Okumura, S. Yoshida, "Intrinsic defects in cubic silicon carbide", *Phys. Stat. Sol.* (a) **162** 173–198 (1997).

[Itoh1998] H. Itoh, T. Troffer, C. Peppermuller, G. Pensl, "Effects of C or Si co-implantation on the electrical activation of B atoms implanted in 4H-SiC", *Appl. Phys. Lett*. **73** 1427-1429 (1998).

[Ivanov2005] I. G. Ivanov, A. Henry, E. Janzén, "Ionization energies of phosphorus and nitrogen donor and aluminum acceptors in 4H silicon carbide from the donor-acceptor pair emission", *Phys. Rev*. B **71** 241201(1–4) (2005).

[Jagodzinski1949] H. Jagodzinski, "Eindimensionale Fehlordnung in Kristallen und ihr Einfluss auf die Röntgeninterferenzen. I. Berechnung des Fehlordnungsgrades aus den Röntgenintensitäten", *Acta Crystallogr.* **2** 201–207 (1949).

[Kawasuso1996] A. Kawasuso, H. Itoh, S. Okada, H. Okumura, "Annealing processes of vacancy-type defects in electron-irradiated and as-grown 6H-SiC studied by positron lifetime spectroscopy", *J. Appl. Phys.* **80** 5639–5645 (1996).

[Kimoto1994] T. Kimoto, H. Matsunami, "Surface kinetics of adatoms in vapor phase epitaxial growth of SiC on 6H-SiC{0001} vicinal surfaces", *J. Appl. Phys*. **75** 850–859 (1994).

[Kimoto2015] T. Kimoto, "Material science and device physics in SiC technology for high-voltage power devices", *Jpn. J. Appl. Phys.* **54** 040103(1–27) (2015).

[Knippenberg1963] W. F. Knippenberg, "Growth phenomena in silicon carbide", *Philips Reports* **18** 161–274 (1963).

[Kordina1995] O. Kordina, A. Henry, J. P. Bergman, N. T. Son, W. M. Chen, C. Hallin, E. Janzén, "High quality 4H-SiC epitaxial layers grown by chemical vapor deposition", *Appl. Phys. Lett*. **66** 1373–1375 (1995).

[Kordina1996] O. Kordina, C. Hallin, A. S. Bakin, I. G. Ivanov, A. Henry, R. Yakimova, M. Touminen, A. Vehanen, E. Janzén, "High temperature chemical vapor deposition of

SiC", *Appl. Phys. Lett.* **69** 1456–1458 (1996).

[Kunzer1995] M.Kunzer, U. Kaufman, K. Maier, J. Schneider, "Magnetic circular dichroism and electron spin resonance of the A^- acceptor state of vanadium, V^{3+}, in 6H-SiC", *Mater. Sci. Eng*. (b) **29** 118–121 (1995).

[Kuroda1987] N. Kuroda, K. Shibahara W. Yoo, S. Nishino, H. Matsunami, "Step controlled VPE growth of SiC single crystals at low temperatures", in *Conference on Solid State Devices and Materials*, pp. 227–230 (1987).

[Landolt1987] Landolt-Börnstein, "Numerical data and functional relationships in science and technology, volume 22 – Semiconductors, subvolume A – intrinsic properties of group IV elements and III-V, II-VI and I-VII compounds", O. Madelung, W. Von der Osten, U. Rössler (Eds.), Berlin, Heidelberg: Springer-Verlag, 1987, pp. 46–48.

[Langer1985] J. M. Langer, H. Heinrich, "Deep-level impurities: A possible guide to prediction of band-edge discontinuities in semiconductor heterojunctions", *Phys. Rev. Lett*. **55** 1414–1417 (1985).

[Larkin1997] D. J. Larkin, "SiC dopant incorporation control using site-competition CVD", *Phys. Stat. Sol*. (b) **202** 305–320 (1997).

[Laube2002] M. Laube, F. Schmid, G. Pensl, G. Wagner, M. Linnarsson, M. Maier, "Electrical activation of high concentrations of N^+ and P^+ ions implanted into 4H-SiC", *J. Appl. Phys*. **92** 549–554 (2002).

[LaVia2014] F. La Via, M. Camarda, A. La Magna, "Mechanisms of growth and defect properties of epitaxial SiC", *Appl. Phys. Rev*. **1** 031301(1–36) (2014).

[Lebedev1999] A. Lebedev, "Deep level centers in silicon carbide: A review", *Semiconductors* **33** 107–130 (1999).

[Lebedev2006] A. A. Lebedev, "Heterojunctions and superlattices based on silicon carbide", Semiconductor Science and Technology **21** R17–34 (2006).

[Lely1955] A. Lely, "Darstellung von Einkristallen von Siliziumcarbid und Beherrschung von Art und Menge der eingebauten Verunreinigungen", *Ber. Dtsch. Keram. Ges*. **32** 229-236 (1955).

[Lingner2001] Th. Lingner, S. Greulich-Weber, J. M. Spaeth, "Structure of the silicon vacancy in 6H-SiC after annealing identified as the carbon vacancy-carbon antisite pair", *Phys. Rev*. B **64** 245212(1–10) (2001).

[Linnarsson1999] M. K. Linnarsson, M. S. Janson, S. Karlsson, A. Schöner, N. Nordell, B. G. Svensson, "Diffusion of light elements in 4H- and 6H-SiC", *Mater. Sci. Eng*. (b) **61–62**

275–280 (1999).

[Machado2015] W. V. M. Machado, J. F. Justo, L. V. C. Assali, "Iron and manganese-related magnetic centers in hexagonal silicon carbide: A possible roadmap for spintronic devices", *J. Appl. Phys.* **118** 045704(1–6) (2015).

[Maier1992] K. Maier, J. Schneider, W. Wilkening, S. Leibenzeder, R. Stein, "Electron spin resonance studies of transition metal deep level impurities in SiC", *Mater. Sci. Eng* (b) **11** 27–30 (1992).

[Matsunami1981] H. Matsunami, S. Nishino, H. Ono, "Heteroepitaxial growth of cubic silicon carbide on foreign substrates", *IEEE Trans. Electron Dev.* **28** 1235–1236 (1981).

[Mattausch2001] A. Mattausch, M. Bockstedte, O. Pankratov, "Self diffusion in SiC: the role of intrinsic point defects", *Mater. Sci. Forum* **353–356** 323–326 (2001).

[Medvedeva2003] N. I. Medvedeva, E. I. Yur'eva, A. L. Ivanovskii, "Electronic structure of cubic silicon carbide with substitutional 3d impurities at Si and C sites", *Semiconductors* **37** 1243–1246 (2003).

[Miao2003] M. Miao, W. Lambrecht, "Magnetic properties of substitutional 3d transition metal impurities in silicon carbide", *Phys. Rev.* B **68** 125204(1–10) (2003).

[Miao2006] M. S. Miao, W. R. L. Lambrecht, "Electronic structure and magnetic properties of transition-metal-doped 3C and 4H silicon carbide", *Phys. Rev.* B **74** 235218(1–10) (2006).

[Mitchel1998] W. C. Mitchel, R. Perrin, J. Goldstein *et al*., "Deep levels in SiC:V by high temperature transport measurements", *Mater. Sci. Forum* **264–268** 545–548 (1998).

[Miyata2008] M. Miyata, Y. Higashiguchi, Y. Hayafuji, " *Ab initio* study of substitutional impurity atoms in 4H-SiC", *J. Appl. Phys.* **104** 123702(1–4) (2008).

[Moissan1904] H. Moissan, "Nouvelles recherches sur la météorité de Canon Diablo", *Comptes rendus* **139** 773–786 (1904).

[Momma2011] K. Momma, F. Izumi, "VESTA 3 for three-dimensional visualization of crystal, volumetric and morphology data", *J. Appl. Crystallogr*. 44 1272–1276 (2011).

[Moore1993] W. J. Moore, P. J. Lin-Chung, J. A. Freitas Jr., Y. M. Altaiskii, V. L. Zuev, L. M. Ivanova, "Nitrogen donor excitation spectra in 3C-SiC", *Phys. Rev.* B **48** 12289-12291(1993).

[Nishino1983] S. Nishino, J. A. Powell, H. A. Will, "Production of large-area single-crystal wafers of cubic SiC for semiconductor devices", *Appl. Phys. Lett*. **42** 460–462 (1983).

[Ohshige2014] C. Ohshige, T. Takahashi, N. Ohtani, M. Katsuno, T. Fujimoto, S. Sato, H. Tsuge, T. Yano, H. Matsuhata, M. Kitabatake , "Defect formation during the initial stage of physical vapor transport growth of 4H-SiC in the [1120] direction", *J. Crystal Growth*

408 1–6 (2014).

[Oshima2001] T. Ohshima, A. Uedono, H. Abe, Z. Q. Chen, H. Itoh, M. Yoshikawa, K. Abe, O. Eryu, K. Nakashima, "Positron annihilation study of vacancy-type defects in silicon carbide co-implanted with aluminum and carbon ions", *Physica* B **308–310** 652–655 (2001).

[Patrick1966] L. Patrick, D. R. Hamilton, W. J. Choyke, "Growth, luminescence, selection rules and lattice sums of SiC with wurtzite structure", *Phys. Rev.* **143** 526–536 (1966).

[Pensl1993] G. Pensl, W. J. Choyke, "Electrical and optical characterization of SiC", *Physica* B **185** 264–283 (1993).

[Ramsdell1947] L. S. Ramsdell, "Studies on silicon carbide", *Am. Mineral*. **32** 64–82, (1947).

[Rauls2000] E. Rauls, Th. Lingner, Z. Hajnal, S. Greulich-Weber, Th. Frauenheim, J. M. Spaeth, "Metastability of the neutral silicon vacancy in 4H-SiC", *Phys. Stat. Sol*. (b) **217** R1–R3 (2000).

[Raynaud1994] C. Raynaud, F. Ducroquet, G. Guillot, L. M. Porter, R. F. Davis, "Determination of ionization energies of the nitrogen donors in 6H-SiC by admittance spectroscopy", *J*. *Appl*. *Phys*. **76** 1956–1958 (1994).

[Reshanov2000] S. A. Reshanov, "Growth and high temperature performance of semi-insulating silicon carbide", *Diam. Relat. Mater.* **9** 480–482 (2000).

[Round1907] H. J. Round, "A note on Carborundum", *Electr. World* **19** 309 (1907).

[Rüschenschmidt2001] K. Rüschenschmidt, H. Bracht, M. Laube, N. A. Stolwijk, G. Pensl, "Diffusion of boron in silicon carbide", *Physica* B **308–310** 734–737 (2001).

[Schmid2006] F. Schmid, S. A. Reshanov, H. B. Weber, G. Pensl, M. Bockstedte, A. Mattausch, O. Pankratov, T. Ohshima, H. Itoh, "Deactivation of nitrogen donors in silicon carbide", *Phys. Rev*. B **74** 245212(1–11) (2006).

[Schneider1993] J. Schneider, K. Maier, "Point defects in silicon carbide", *Physica* **B 185** 199–206 (1993).

[Shrader2011] D. Shrader, S. M. Khalil,T. Gerczak, T. R. Allen, A. J. Heim, I. Szlufarska, D. Morgan, "Ag diffusion in cubic silicon carbide", *J. Nucl. Mater*. **408** 257–71 (2011).

[Silva2013] D. J. Silva, U. Wahl, J. G. Correia, J. P. Araujo, Influence of n^+ and p^+ doping on the lattice sites of implanted Fe in Si *J. Appl. Phys.* **114** 103503(1–9) (2013).

[Silva2014] D. J. Silva, U. Wahl, J. G. Correia, L. M. C. Pereira, L. M. Amorim, M. R. da Silva, E. Bosne, J. P. Araújo, "Lattice location and thermal stability of implanted nickel in silicon studied by on-line emission channeling", *J. Appl. Phys.* **115** 023504(1–9) (2014).

[Silva2016] D. J. Silva, U. Wahl, J. G. Correia, L. M. Amorim, M. R. Da Silva, L. M. C. Pereira,

J. P. Araújo, “Direct observation of the lattice sites of implanted manganese in silicon”, *Appl. Phys.* A **122** 241(1–7) (2016).

[Smith1999] S. R. Smith, A. O. Evwaraye, W. C. Mitchel, M. A. Capano, “Shallow acceptor levels in 4H- and 6H-SiC”, *J. Elect. Mater.* **28** 190–195 (1999).

[Stockmeier2009] M. Stockmeier, R. Müller, S. A. Sakwe, P. J. Wellmann, A. Magerl, “On the lattice parameters of silicon carbide”, *J. Appl. Phys.* **105** 0033511(1–4) (2009).

[Sudarshan1997] T. S. Sudarshan, G. Gardinaru, G. Korony, S. A. Gradinaru, W. Mitchel, “High field/high temperature performance of semi-insulating silicon carbide”, *Diamond Relat. Mater.* **6** 1392–1395 (1997).

[Suttrop1992] W. Suttrop, G. Pensl, W. J. Choyke, R. Stein, S. Leibenzeder, “Hall effect and infrared absorption measurements on nitrogen donors in 6H- silicon carbide”, *J. Appl. Phys.* **72** 3708–3713 (1992).

[Svensson1998] B. G. Svensson, M. K. Linnarsson, J. Cardenas, M. Petravic, “SIMS analysis of epitaxial layers of power- and micro-electronics”, *Nucl. Inst. Meth. Phys. Res.* B **136–138** 1034–1039 (1998).

[Tairov1973] Yu. M. Tairov, V. F. Tsvetkov, I. I. Khlebnikov, “Growth of silicon carbide crystals by vapour- liquid-solid (VLS) mechanism in the sublimation method”, *J. Cryst. Growth* **20** 155–157 (1973).

[Tairov1978] Yu. M. Tairov, V. F. Tsvetkov, “Investigation of growth processes of ingots of silicon carbide single crystals”, *J. Cryst. Growth* **43** 209–212 (1978).

[Tairov1981] Yu. M. Tairov, V.F. Tsvetkov, “General principles of growing large-size single crystals of various silicon carbide polytypes”, *J. Cryst. Growth* **52** 146–150 (1981).

[Takano2007] F. Takano, W. Wang, H. Akinaga, H. Ofuchi, S. Hishiki, T. Ohshima, “Characterization of Mn-doped 3C-SiC prepared by ion implantation”, *J. Appl. Phys.* **101** 09N510(1–3) (2007).

[Torpo2001] L. Torpo, M. Marlo, T. E. M. Staab, R. M. Nieminem, “Comprehensive *ab initio* study of properties of monovacancies and antisites in 4H-SiC”, *J. Phys. Cond. Matt.* **13** 6203–6231 (2001).

[Wahl2005] U. Wahl, J. G. Correia, E. Rita, J. P. Araújo, J. C. Soares, “Lattice sites of implanted Fe in Si”, *Phys. Rev.* B **72** 014115(1–8) (2005).

[Wahl2006] U. Wahl, J. G. Correia, E. Rita, J. P. Araújo, J. C. Soares, “Fe and Cu in Si: Lattice sites and trapping at implantation-related defects”, *Nucl. Instruments Methods Phys. Res.* B **253** 167–171 (2006).

[Wang1988] C. Wang, J. Bernholc, R. F. Davis, “Formation energies, abundances and the electronic structure of native defects in cubic SiC”, *Phys. Rev*. B **38** 12752–12755 (1988).

[Williams1998] J. S. Williams, “Ion implantation of semiconductors”, *Materials Science and Engineering* A **253** 8–15 (1998).

[Woodbury1961] H. H. Woodbury, G. W. Ludwig, “Electron spin resonance studies in SiC”, *Phys. Rev*. **124** 1083–1089 (1961).

[Wright2016] E. Wright, J. Coutinho, S. Öberg, V. J. B. Torres, “Mössbauer parameters of Fe-related defects in group-IV semiconductors : First principles calculations”, *J. Appl. Phys.* **119** 181509(1–16) (2016).

[Zubatov1985] A. G. Zubatov, I. M. Zaritskii, S. N. Lukin, E. N. Mokhov, V. G. Stepanov, “Electron spin resonance in boron-doped silicon carbide”, *Sov. Phys. Solid State* **27** 197–201 (1985).

[Zywietz1999] A. Zywietz, J. Furthmüller, F. Bechstedt, “Vacancies in SiC: Influence of Jahn-Teller distortions, spin effects and crystal structure”, *Phys. Rev.* B **59** 15166–15180 (1999).

Chapter 2

Lattice location: electron emission channeling

This chapter presents the emission channeling (EC) technique and discusses its different aspects: from the principle of the technique via the experimental realization to the quantitative data analysis procedures and the difficulties that come along with it.

2.1. The principle

The influence of the crystal lattice on trajectories of charged particles is known as channeling. The atomic rows and planes act as guides that steer energetic particles along the major crystal axes and planes. Figure 2.1 shows a schematic representation of a simple cubic lattice, seen from three particular directions: a crystal axis, a crystal plane and a “random” direction. The motion of energetic charged particles in a solid is mainly determined by their Coulomb interaction with the screened nuclear charges in the lattice. Because of that, it is expected that the particle propagation is very different among these three types of directions.

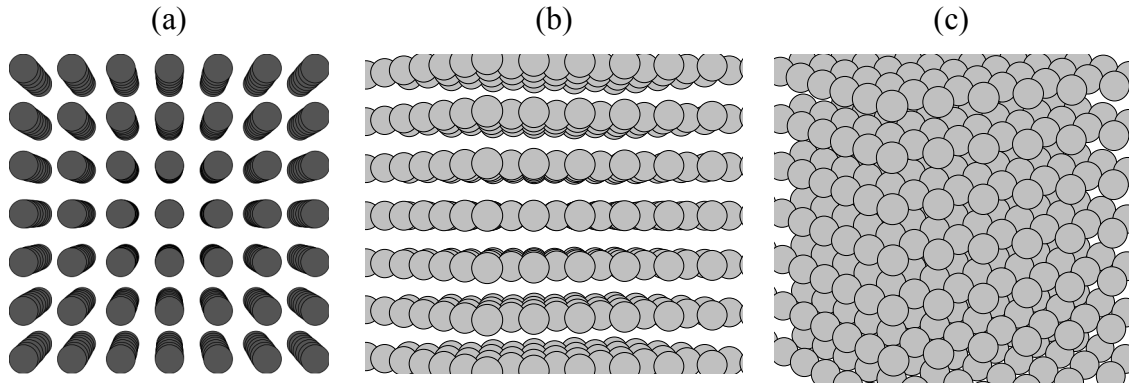

Figure 2.1. Cubic lattice representation seen from three different directions: (a) parallel to a crystallographic axis; (b) parallel to a crystal plane; (c) random orientation.

In 1965, Lindhard [Lindhard1965] provided the theoretical framework for the channeling effect by showing that positively charged particles moving along directions aligned with a crystal axis could be steered by multiple small-angle collisions with the crystal atoms. More specifically, three requirements have to be met for this to happen [Thompson1973]: (1) called *transparency* – the particle must propagate through an open channel between the rows of atoms; (2) called *steering* – the screened repulsive Coulomb potential of the rows of nuclei steers the charged particle towards the middle of the channel (represented by the black arrows located in the upper right image of Fig. 2.2); (3) called *stability* – requires that the charged particle does not approach the atom rows too closely, otherwise the particle experiences wide-angle deflections in head-on collisions with individual atoms. These wide-angle deflections constitute the so-called *blocking* effect. The grey arrows in the upper two panels of Fig. 2.2 identify this blocking effect. The concept of channeling also applies to negatively charged particles; however, they will be attracted to the positively charged rows of nuclei and will thus channel along atomic rows instead of within the open channels in between them (represented by the black arrows of the two bottom panels of Fig. 2.2).

Let us now consider the situation of emission channeling or blocking, i.e. that a charged particle is emitted from a certain position within a single crystal, e.g. by a radioactive impurity, for which the general possibilities are illustrated in Fig. 2.2. If the emission occurs from a substitutional lattice site, a positively charged particle will experience blocking effects along all crystallographic directions (upper left part of Fig. 2.2) while a negatively charged particle will undergo channeling effects (lower left part of Fig. 2.2). On the other hand, emission of a positively charged particle by a non-substitutional impurity will result in channeling effects along those crystallographic directions with respect to which the site is interstitial, while blocking is observed for those with which the site happens to be aligned (upper right part of

Fig, 2.2). For emission of a negatively charged particle from an interstitial site (lower right part of Fig. 2.2) channeling is observed only for those directions with which the site is still aligned, while along the others the trajectories are unstable, leading to a "softer" form of blocking. The general remark that the occupation of interstitial sites cannot lead to the same type of effect (channeling or blocking) along all crystallographic directions is hence true independently of the type of charge the impurity has. Generally speaking, in all cases the particle flux inside the crystal will be redistributed in a very specific way, generating also anisotropic angular yield distributions outside the crystal that uniquely depend on the lattice site of the emitter impurity as well as on the charge of its decay products.

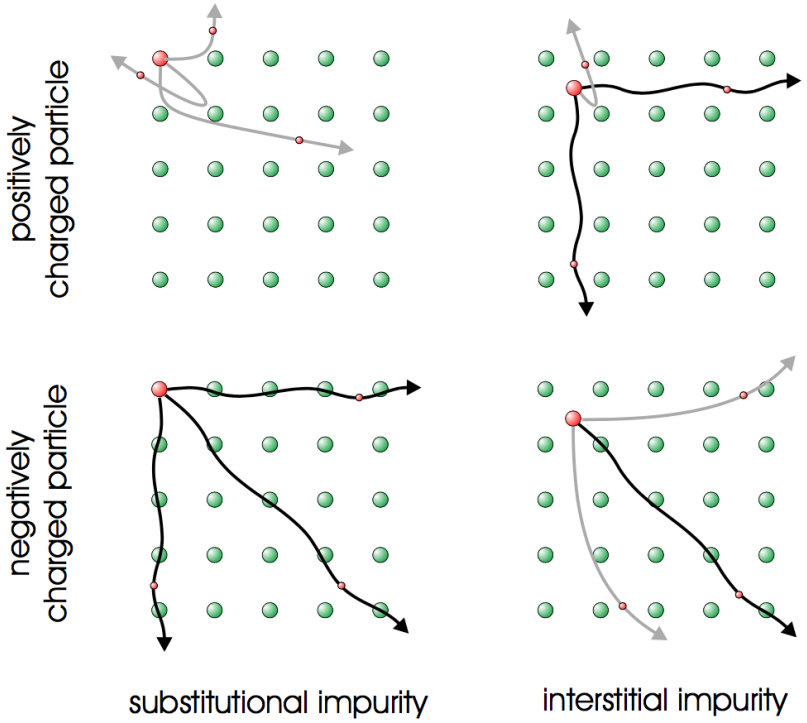

Figure 2.2. Simplified scheme indicating channeling (black arrows) and blocking (grey arrows) effects for positively and negatively charged particles emitted at substitutional and interstitial impurities along different crystallographic directions.

Detailed analysis of anisotropic angular emission yield patterns along a variety of crystallographic directions is hence the basic principle of emission channeling as a lattice location technique.

In contrast, conventional channeling lattice location techniques rely on the use of an external ion beam and how its interaction with the impurity atoms depends on the beam direction with respect to the lattice. Several techniques can be applied in a typical channeling experiment to provide information on lattice location of impurities: Rutherford Backscattering Spectrometry (RBS), Particle Induced X-ray Emission (PIXE) and Nuclear Reaction Analysis (NRA).

However, the principle of emission channeling is different in the sense that the channeled particles are emitted from within the crystal by a radioactive isotope of the impurity element under study. The analysis of angular yields of these two types of channeling techniques has been shown to be equivalent to a large extent. The transition probabilities for direct (charged particle coming from the outside of the crystal) and reverse processes (emission from the interior) are equal. This equivalence is known as Lindhard's reciprocity theorem since it was concluded by Lindhard [Lindhard1965] based on the reversibility of particle tracks.

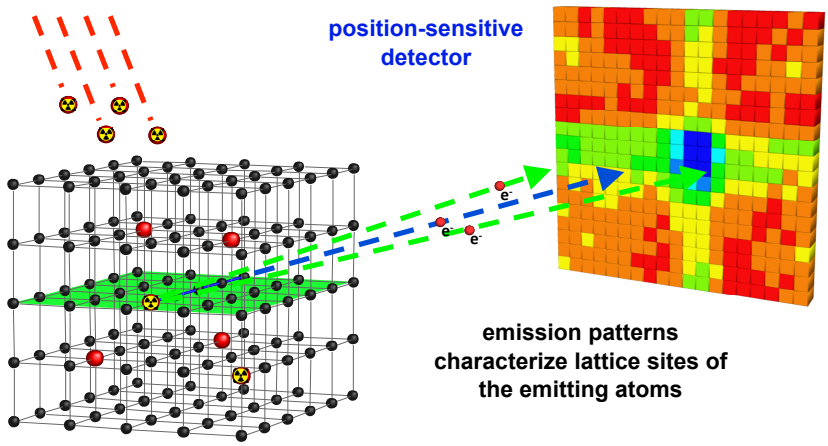

Figure 2.3. Basic principles of emission channeling experiments using 2D position sensitive detectors.

The emission channeling technique is commonly applied using either α or electron (β^- or conversion electron) emitters. In the latter case, the technique is known as electron emission channeling. Note that, while the method also works using positron emission, the number of suitable β^+-emitting radioisotopes is quite small so that this variant is not very common. A typical experiment using electron emission channeling can be summarized in four steps and is schematically described by Fig. 2.3: (1) radioactive electron (β^- or conversion electron) emitting isotopes are implanted in a single crystal or epitaxial film, occupying certain lattice site(s); (2) a fraction of the emitted electrons are channeled along the crystal axes and planes leaving the sample surface describing anisotropic emission patterns which are characteristic of the emission site and channeling axis; (3) the anisotropic patterns are recorded using a 2-dimensional (2D) position-sensitive detector around selected crystallographic axes; (4) the lattice site(s) of the impurities is determined by fitting the 2-dimensional experimental patterns with theoretical ones. All these aspects will be briefly discussed in the following sections of

this chapter. More details on the experimental aspects of EC can be found in [Hofsäss1991, Hofsäss1994, Hofsäss1996, Wahl2000].

A final remark is that emission channeling is especially suited to study the lattice site location of low-fluence implanted isolated impurities, down to 10^{11} cm^{-2}, or in systems where conventional ion beam techniques cannot be applied. As an example, RBS relies on elastic backscattering, which limits the study to impurity elements that are heavier than the major constituents of the host material. Although, for this particular study, this is not a problem because the studied impurity elements are heavier than Si and C, RBS requires typical impurity fluences above 10^{14}–10^{15} cm^{-2}, roughly 3-4 orders of magnitude higher than emission channeling. Probably one of the strongest features of the emission channeling technique is its applicability to those cases where significant fractions of the impurities occupy more than one lattice site. Other techniques, e.g. Mössbauer and perturbed angular correlation (PAC) spectroscopies, are also very sensitive and can in some cases distinguish different lattice sites, however, contrary to electron emission channeling, lattice location can only be indirectly inferred from the spectra.

2.2. Ion implantation

Ion implantation is a convenient way to incorporate foreign atoms into a host material. Atoms or molecules are ionized in an ion source, extracted and accelerated by an electrostatic field to energies of a few thousand electron-volt (keV). While the implantation of stable isotopes is a routine process performed in many laboratories around the world, the implantation of radioactive isotopes is reserved to facilities that have implemented suited radioprotection measures. Moreover, if the radioisotopes are short-lived, it is imperative to combine isotope production and implantation in the same facility. This process is performed at the Isotope Separator On Line Device (ISOLDE) facility located at CERN in Switzerland [Kugler2000, Jonson2000, Deicher2003] where the radioactive probes are produced via spallation, fission or fragmentation reactions in thick targets, induced by proton beams from the Proton Synchrotron Booster (PSB) at energies and intensities up to 1.4 GeV and 2 μA, respectively, as illustrated in Fig. 2.4. The volatile nuclear reaction products are then released from the high temperature target. To accelerate them, the desired species have to be ionized. Three different types of ion sources are used: (i) surface ion source, which consists in the heating of materials in contact with the targets, such as tantalum or tungsten, with a larger work function than the atom to be ionized; (ii) plasma ion source, where electrons are freed from the radioactive isotopes through

collisions with gas ions in plasma discharges; (iii) Resonance Ionization Laser Ion Source (RILIS) – a laser ion source applies the excitation of specific electrons from the radioactive isotopes by photons from lasers [Fedoseyev2000]. Subsequently, the ions are separated by mass, using an analyzing magnet and finally impinge on the desired sample material.

Regarding the implantation process, in SiC crystals typical implanted layers have depths of about 200-300 Å if the energy of the ion beam ranges in between 40-60 keV. The ions come to rest by dissipating the kinetic energy through interactions (i.e, collisions) with electrons and nuclei in the host material, the latter resulting in the displacement of those atoms from their lattice sites. The displaced atoms can then collide with other host atoms, thus creating a collision cascade and producing defects if the host material has a crystalline structure. The creation of crystal defects is usually undesirable because it will alter the electrical, optical and/or mechanical material properties. The amount of damage created depends on several factors, such as the host material, the ion fluence, the mass of the implanted ions, the substrate temperature, the implantation geometry, etc. In the extreme case, accumulation of damage can lead to amorphization of the implanted layer. The standard method for restoring the crystal lattice is high-temperature annealing.

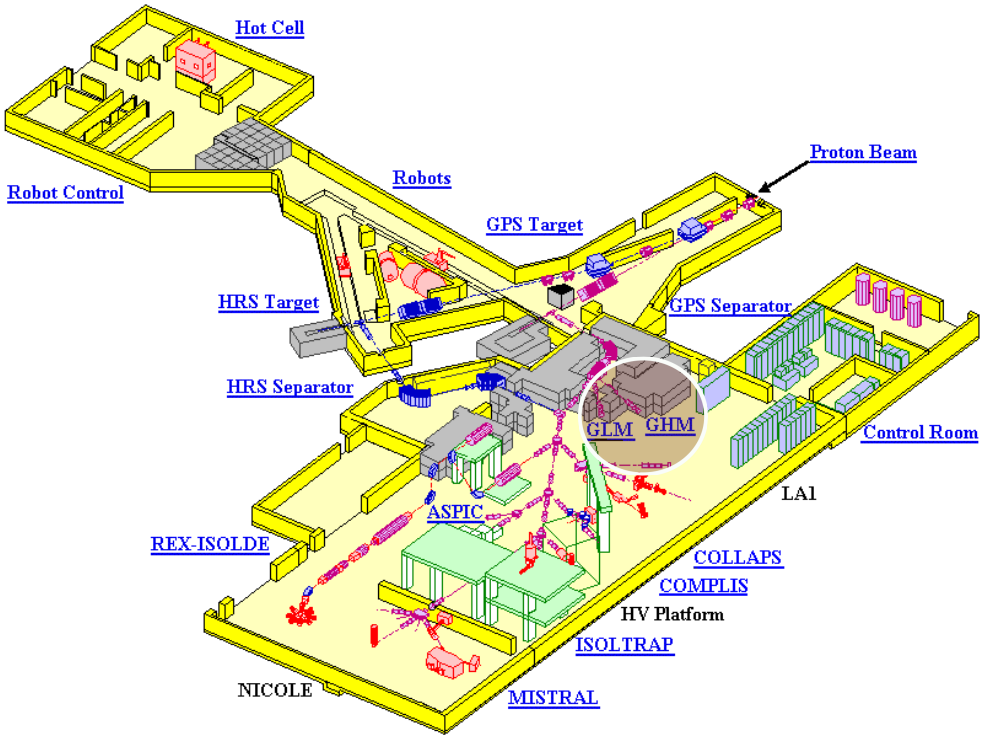

Figure 2.4. Schematic layout of the production process of radioactive ion beams from ISOLDE. These ion beams can be separated with the general purpose separator (GPS) or the high resolution separator (HRS) magnets. The circle indicates the GLM and GHM beam lines where the implantations of the radioisotopes used in this work were performed.

The implantation depth and corresponding straggling (i.e. the variance of the distribution) can be calculated with SRIM (the Stopping Power and Range of Ions in Matter) code, which is a Monte Carlo computer simulation program [Ziegler2010].

Low radioactive probe fluences (10^{12}-10^{13} cm^{-2}) were preferred in all studies in order to keep implantation damage as low as possible. Another advantage of the low-fluence implantation process is that the concentration of the probe atoms in the implanted layer will be very low, avoiding interaction between them (clustering), allowing the lattice site determination as isolated impurities.

Two different SiC polytypes were used to produce all measured samples in this work: undoped single-crystalline cubic 3C-SiC samples with <100> oriented surfaces, all obtained from Hoya Corporation (Japan), and c-axis oriented 6H-SiC single crystal samples, cut from a wafer obtained from CrysTec GmbH. The long-lived isotope implantations were performed, depending on availability, in two distinct implantation chambers connected to the GLM and GHM beam lines (identified in Fig. 2.4). The GLM chamber is a general purpose solid state implantation chamber equipped with beam collimators (producing well defined beam spots of 0.5, 1, 2 or 5 mm in diameter), a secondary electron suppressor plate and a sample holder with nine positions for sample mounting, allowing thus multiple implantations with long-lived isotopes without breaking the vacuum. The suppressor plate placed in front of the sample holder minimizes the emission of secondary electrons from the sample, which would otherwise interfere with the beam current readout (typically 1 pA to 100 pA), performed on the sample holder. The second chamber (named as Small Implantation Chamber – SIC) is located in the GHM beam line, just before the main implantation chamber where on-line EC measurements are performed. It is a compact implantation chamber equipped with a variable diameter beam collimator and a sample holder with 4 positions. Since the SIC chamber does not contain an electron suppressor, due to the emission of secondary electrons the currents measured on the sample holder are significantly higher than the real implantation current: for typical implantation conditions at ISOLDE secondary electron emission increases the measured beam by a factor of ~3.5. While this can be corrected, the implanted fluences calculated for the SIC chamber are subject to a larger error of ± 30%.

2.3. Experimental setups

The implanted samples are subsequently mounted in one of several off-line EC setups, each equipped with a 2-dimensional energy and position sensitive detector that measures the

emission yields when aligned with the major high symmetry crystal directions of the sample, under high vacuum (10^{-5} mbar). However, the transfer of the sample from the implantation chamber to the off-line measurement chamber plus the need for high vacuum and waiting time for sample cool down to RT after the annealing procedure (can go up to 900 °C) before a EC measurement can be made, are all time consuming tasks. They limit the choice to radioisotopes with half-lives of at least several hours. Ideally the chosen radioisotope should have a half-life of several days. A further major constraint is related to the maximum count-rate that the off-line detectors are able to measure, that is limited to 250 events/s by the readout procedure. This is sufficient for typical off-line experiments with long-lived radioactive isotopes implanted at low to moderate fluences, but clearly insufficient if one wants to measure short-lived radioisotopes. These types of isotopes, even implanted at low fluences, produce count-rates of several kHz. To overcome this limitation, detectors with fast readout systems that can produce higher count-rates (several kHz) were acquired along with a new chamber and goniometer and installed at the end of the GHM beam line in 2009. This online setup allows both implantation and measurement at the same time [daSilva2013] enabling the use of short lived isotopes such as ^{56}Mn or ^{65}Ni, being only limited by the time required for thermal treatments.

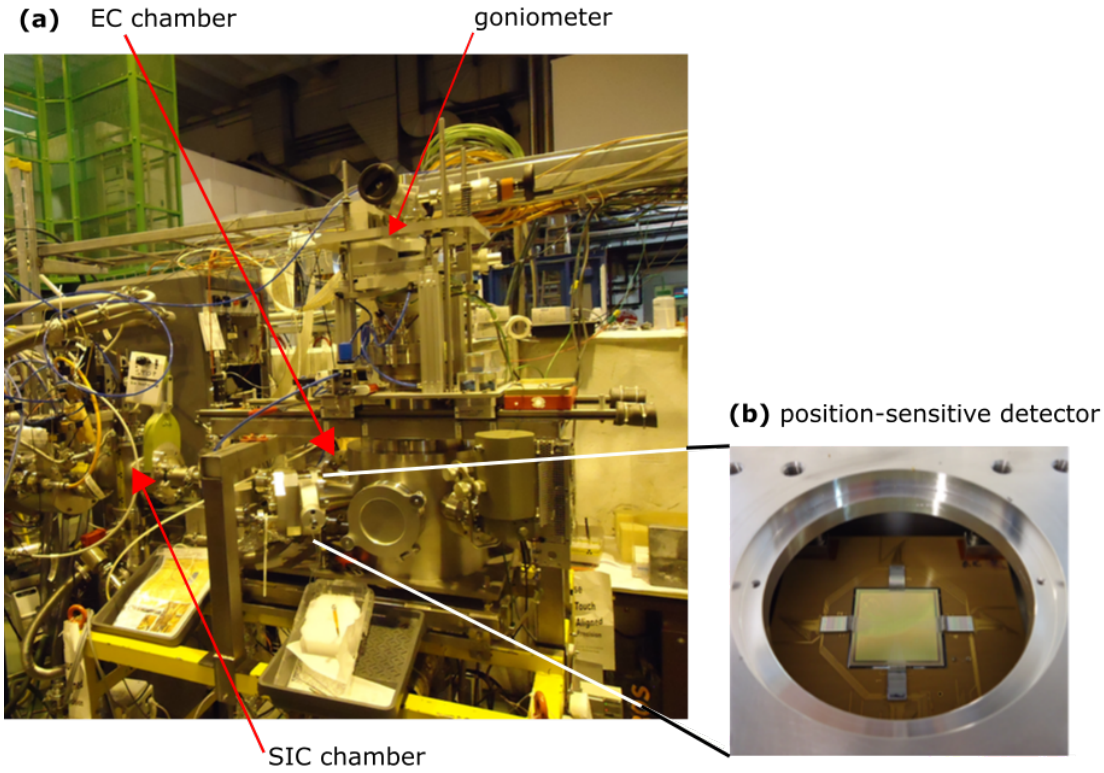

Figure 2.5. (a) Picture of the on-line EC setup with its three components: EC chamber, goniometer and (b) position-sensitive detector. One of the implantations chambers - SIC chamber is also identified.

Each EC setup consists of a high vacuum chamber, a goniometer and a position-sensitive detector, shown in Fig. 2.5, and described briefly below:

(i) High vacuum chamber (identified as EC chamber in Fig. 2.5): with a vacuum around 10^{-6} mbar, the sample is mounted vertically on the sample holder, facing the detector, oriented in such a way that electrons emerging from the sample surface with angles of a few degrees from the measured crystallographic axis reach the position-sensitive detector. The emission yield is recorded as a function of angle in the form of 2-dimensional patterns. (ii) Goniometer: The goniometer allows moving the sample up and down and rotating it around several axes of rotation. While the on-line chamber is equipped with a high precision 3-axes goniometer (reproducibility around 0.05°-0.1°), the off-line chambers contain only simpler 2-axes goniometers of 0.1°-0.2° precision. All sample holders are equipped with resistive heating devices; in the off-line setups folded tungsten wire devices allow in situ vacuum annealing of samples up to 900 °C while in the on-line setup a button heater element allows to reach 800 °C. (iii) Position-sensitive detector: Both off-line and on-line setups use position-sensitive Si detectors of the "pad" type. The principle of operation of the pad detectors is based on integrating an array of separate detector cells on a single Si chip and individually contacting them on the surface by a pattern of conducting and insulating layers [Weilhammer1996]. The term "pad" is used rather than "pixel" since the number of detector cells is comparatively small and in the ~mm size, while typical pixel detectors in high-energy physics consist of several thousand cells with cell dimension typically less than 100 μm. In our case the square-shaped sensitive area of all pad detectors is 30.8×30.8 mm^2 and divided into 22×22 pixels of 1.4×1.4 mm^2 size, while detectors have varying thickness of 0.3, 0.5 or 1 mm.

In case of the off-line detector systems, the readout of all 484 pads is multiplexed to a single analog digital converter (ADC) and triggered if the signal on the detector back plane, which is common to all pads, exceeds an externally set lower threshold. This readout procedure limits the count rate of the device to a maximum of about 250 events/s, sufficient for long-lived isotopes EC experiments [Wahl2004]. The detector used for the on-line EC experiments has similar physical characteristics but with new faster self-triggering readout chips, which allows multiplexing and processing only those pads that have received a signal. This enabled EC measurements during and/or immediately after implantation with count rates up to several kHz. The experimental angular resolution $\sigma_{ang}(\theta)$ (in °) is a key parameter in the quantitative analysis of EC patterns. For a position-sensitive detection system, it depends on the distance d between sample and detector, on the position resolution of the detector σ_{det} (in mm), which may vary

with energy and nature of the incoming particles, and on the resolution σ_{pbs} (in mm) due to the size and shape of the projected beam spot [Wahl2004]. Assuming that both the position resolution of the detector and the projected beam spot distribution can be approximated as two-dimensional isotropic Gaussian distributions with standard deviations σ_{det} and σ_{pbs}, respectively, the total angular resolution σ_{ang} will be

$$\sigma_{\mathrm{ang}}(\theta) \approx \tan^{-1}\left[\frac{\sqrt{\sigma_{\mathrm{det}}^2 + \sigma_{\mathrm{pbs}}^2}}{d}\right] \qquad (2.1)$$

where d is the distance between sample and detector, which typically should be chosen around 30 cm in order to cover an angular range of 5-6°. Once the distance d is fixed the angular resolution σ_{ang} is then determined by both the detector resolution σ_{det}, which is limited by the size of the pixels, and the standard deviation due to the beam spot size σ_{pbs}. The size of the beam is usually dictated by the fact that samples produced by radioactive ion implantation with beam spots smaller than 1mm are difficult to achieve. Typically ISOLDE beams are not highly focused, the amount of beam that is lost due to collimation with a 1 mm aperture amounts to 50-70%. The overall angular resolution in the experiments described in this thesis was $\sigma_{ang}(\theta) \simeq 0.15°$, to which the detector resolution and beam spot size contribute each with ~0.1°.

2.4. Measurements

The EC results presented in this work were obtained after implanting 3C-SiC and 6H-SiC single crystals with electron emitter radioisotopes[1] at CERN's on-line isotope separator facility, ISOLDE. Subsequently, by means of a position-sensitive detector the emission yields were measured around the <100>, <110>, <111> and <211> axes (3C-SiC), and around the [0001], [$\underline{1}$101], [$\underline{2}$201] and [$\underline{4}$401] axes (6H-SiC), in the as-implanted state and after a number of annealing steps. For most isotopes used in this work (except for the short-lived probe ^{124}In), emission channeling patterns were obtained at room temperature after 10 min isochronal annealing steps *in situ* generally up to 900 °C. Exceptionally, some samples were also externally annealed in a furnace up to 1075 °C in 10^{-6} mbar vacuum. Due to the short half-life (3 s) of ^{124}In, for this isotope implantation and measurement had to take place at the same time, i.e. EC patterns were recorded as a function of implantation temperature.

[1] For a detailed description of the probe nuclei used in this work, see appendix C.

2.5. Data analysis

To obtain a quantitative analysis that allows assessing the fraction of several occupied lattice sites, the experimental two-dimensional emission yield patterns have to be fitted with a linear combination of theoretical ones calculated for emitter atoms on different lattice sites. In this section, it is described briefly how theoretical patterns are produced with the so called *manybeam* simulations, and the related fitting procedure.

2.5.1 *Manybeam* calculations

Theoretical emission patterns are calculated using the *manybeam* program developed by Hofsäss and Lindner [Hofsäss1991, Hofsäss1994, Hofsäss1996], a code which was written at a time when, due to the lack of position-sensitive detectors, only one-dimensional angular scans needed to be simulated. Once the treatment of whole 2-dimensional patterns became necessary, in order to speed up the program modifications and code optimization were introduced by Wahl [Wahl2000], which resulted in the final program. In these calculations the crystal potential is approximated by a superposition of atomic Doyle-Turner potentials. Since for a description of the emission channeling effect only electrons moving under relatively small angles with respect to the channeling axis are relevant and these move at relativistic velocities, the potential along the channeling direction can be averaged and the electron wave function split into a longitudinal component along the channeling direction, which obeys a relativistic Klein-Gordon equation, and a transverse component perpendicular to the axis, which is given by the solution of a two-dimensional Schrödinger equation in a periodic potential. The electron flux density inside the crystal can then be calculated after obtaining the transverse electron wave function using standard Fourier decomposition and Bloch wave techniques. The *manybeam* approach has proven to accurately describe emission channeling effects in a multitude of cases.

The *manybeam* program calculates the angle-dependent emission channeling yields for a number of emitter lattice positions that are defined on input along those crystallographic directions that were previously implemented in the code. Within this work, all angular patterns around the respective channeling axes were calculated in *x*- and *y*-direction from –3° to +3° in steps of 0.05°. To account for the continuous β^- spectra of the isotopes studied in this work, *manybeam* simulations were performed for a number of discrete electron energies (step widths of 25 keV in the energy range 25-800 keV, 50 keV in the range 800-1400 keV, 100 keV in the range 1400-1800 keV) and weighting as indicated by the histograms in Fig. 2.6. Note that the step width can be decreased at higher energies *E* since the half width of channeling effects

depends approximately on $E^{-1/2}$ and in addition the electron intensities in the spectra are quite reduced at higher energies. The number of "beams", which is related to the number of Fourier components in one dimension used in the simulations, was 16 in the energy range 25-725 keV, 20 for 750-950 keV, and 24 for 1000-2750 keV. Note that the higher their kinetic energy electrons are less subject to quantum-mechanical diffraction but behave increasingly according to the laws of classical mechanics; more eigenstates are hence required to describe electron motion in the quantum-mechanical approach of *manybeam* and the number of beams needs to be increased at higher electron energies.

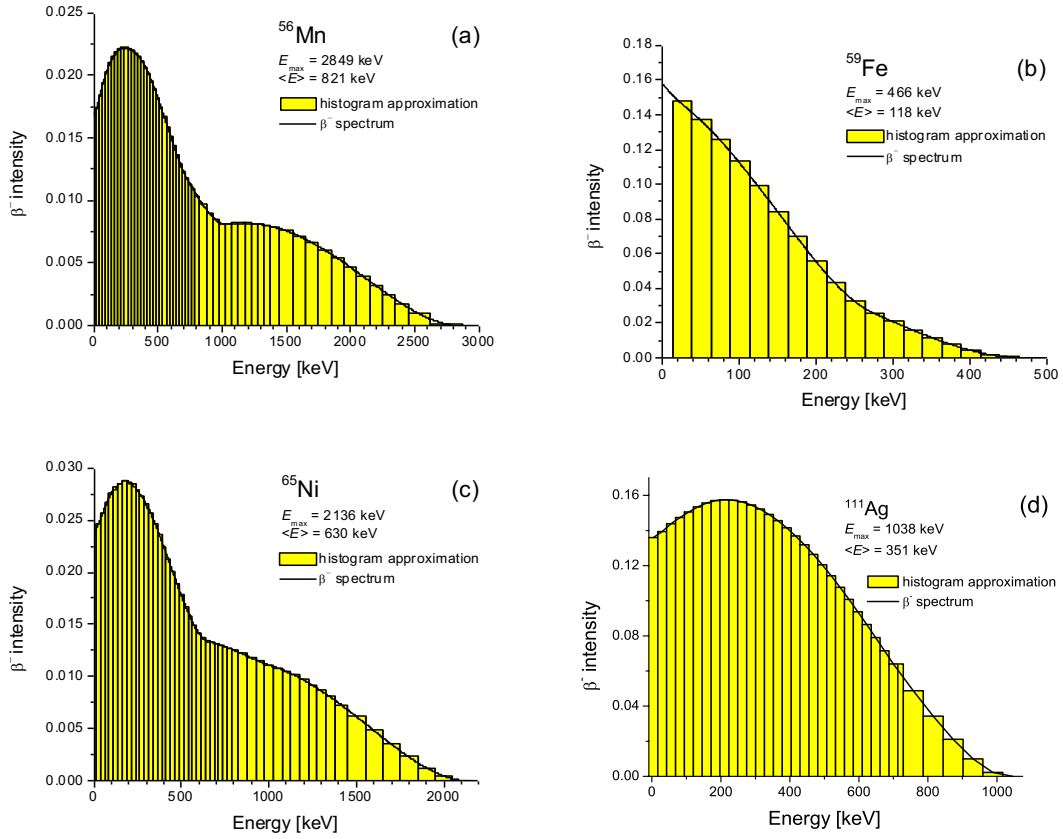

Figure 2.6. Histograms of energy values used to approximate the β^- spectra of ^{56}Mn (a), ^{59}Fe (b), ^{65}Ni (c) and ^{111}Ag (d) in the *manybeam* calculations. β^- spectra were taken from JANIS-JEFF-3.1 [JANIS-JEFF].

The crystal potential was approximated by a superposition of atomic potentials calculated in the Doyle-Turner representation, using the coefficients a_i and b_i for Si and C tabulated in reference [Peng1996] and lattice constants of a=4.3596 Å for 3C-SiC and a=3.081 Å and c=15.117 Å for 6H-SiC. The *manybeam* formalism uses 2-dimensionally projected unit cells with respect to the channeling axes, which can be obtained from the 3-dimensional structures published in the literature. Another important input parameter is the thermal vibration amplitude of the crystal atoms. The one-dimensional root mean square (rms) vibration amplitude u_1 can be calculated from the experimentally determined Debye-Waller factors in

X-ray absorption or diffraction experiments and these u_1 values are preferred as input parameters, rather than rms displacements derived from Debye temperatures that are, for example, estimated from measurements of calorimetric properties, elastic constants or similar techniques, or theoretically calculated from first principles. No experimental data are to be found in the literature on the rms displacements of Si and C atoms in 3C-SiC. They exist only for 2H- [Schulz1979], 4H- [Peng2009] and 6H- [deMesquita1967, Zywietz1996] or unspecified microcrystalline [Stelmakh2007] SiC (Table 2.1). The rms displacements of reference [Schulz1979] were adopted, u_1(Si)=0.0603 Å and u_1(C)=0.0611 Å, for both 3C and 6H polytypes; however, since the published values scatter considerably, for comparison some simulations were also performed using smaller values of u_1(Si)=0.0440 Å and u_1(C)=0.0490 Å (more details about this study can be found in appendix A).

Within the Debye theory the u_1 values at a given temperature T relate to the Debye-temperature T_D via

$$u_1^2 = \frac{3\hbar T}{M k_B \mathrm{T}_D^2}\left[\varphi\left(\frac{T_D}{T}\right) + \frac{T_D}{4T}\right] \qquad 2.2$$

where M is the mass of the element in question, k_B the Boltzmann constant, T_D the Debye temperature and $\varphi(x)$ the Debye function defined as

$$\varphi(x) = \frac{1}{x}\int_0^x \frac{t\,dt}{e^t - 1} \qquad 2.3$$

Eq (2.2) was used to derive T_D(Si) and T_D(C) from the published u_1 values, which results in specific Debye temperatures for the two constituents Si and C. The overall Debye temperature of SiC T_D(SiC) was then estimated according to

$$T_D(SiC) = \frac{1}{2}\left[T_D(Si)\left(\frac{M_{Si}}{M_{av}}\right)^{1/2} + T_D(C)\left(\frac{M_C}{M_{av}}\right)^{1/2}\right] \qquad 2.4$$

with M_{av} = 20. Note that the Debye temperatures are given only for completeness, allowing for comparison to other values found in the literature; they are not needed in our *manybeam* simulations, which depend only on u_1 values as input parameters.

Table 2.1. Room temperature root mean square (rms) displacements u_1 of Si and C atoms in various SiC polytypes according to the cited references. The included Debye temperatures were derived from the u_1 values using the Debye theory.

SiC polytype	u_1(Si) [Å]	u_1(C) [Å]	T_D(Si) [K]	T_D(C) [K]	T_D(SiC) [K]	Reference
2H	0.060	0.061	692	1142	851	[Schulz1979]
4H	0.070	0.070	589	966	723	[Peng2009]
6H	0.041	0.054	1120	1351	1186	[deMesquita1967]
6H	0.051	0.057	843	1254	984	[Zywietz1996]
"microcrystalline"	0.034	0.048	1434	1610	1472	[Stelmakh2007]

Assuming that the displacement of the emitter atoms represents an isotropic Gaussian distribution, its rms is obtained from fitting the experimental patterns with theoretical ones calculated for a set of different rms displacement values. Large deviations (tenths of Å) from these reference values can be associated with static displacements of the impurity due to lattice relaxation in its vicinity.

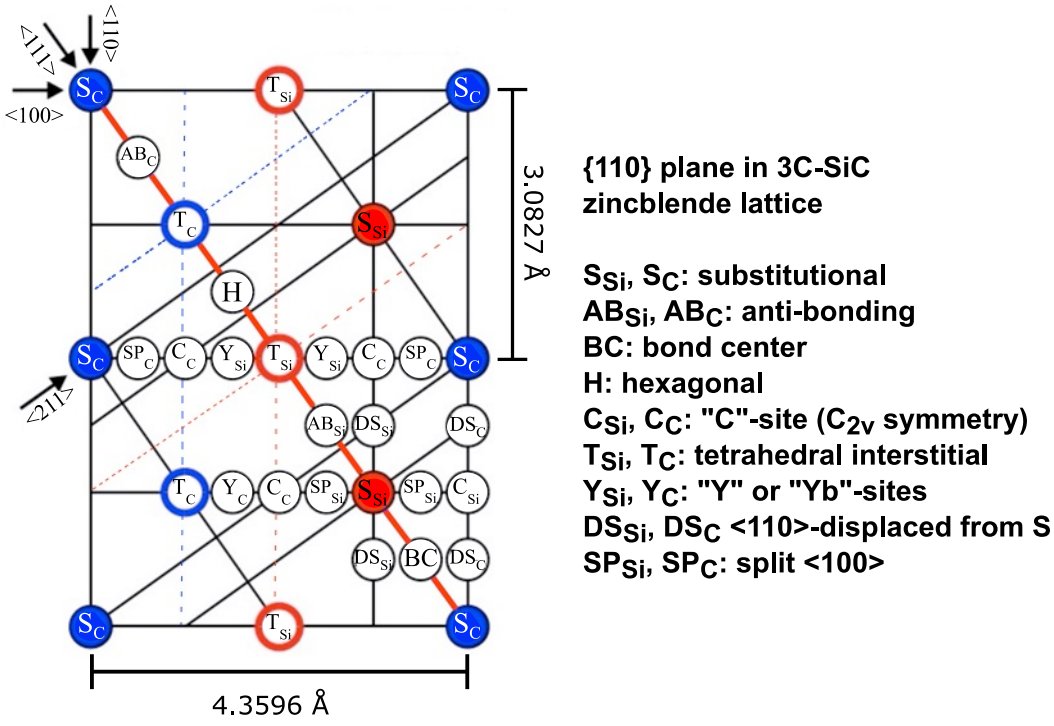

Figure 2.7. Cross-section through the 3C-SiC unit cell along the {110} plane showing the Si and C lattice positions and the main interstitial sites. Note that along the <111> direction the substitutional (S_{Si} and S_C) and tetrahedral interstitial (T_{Si} and T_C) sites are all located on the same row; along the <100> direction S_{Si} is on the same row as T_C while S_C is on the same row as T_{Si}.

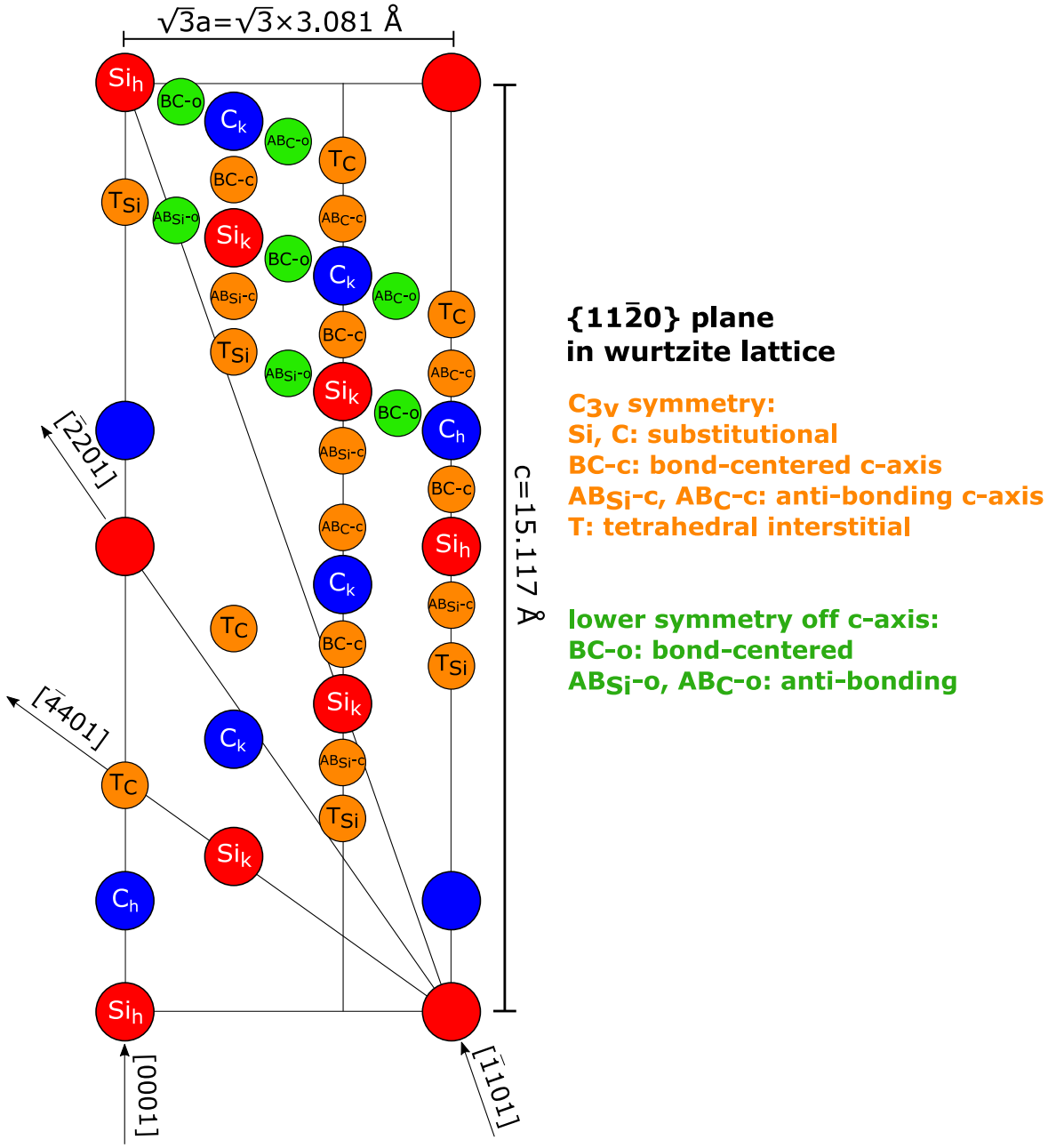

Figure 2.8. Cross-section through the 6H-SiC unit cell along the {11$\underline{2}$0} plane, showing the Si and C atom positions and the major interstitial sites that were investigated as possible lattice sites of TM atoms. Cubic-like and hexagonal-like substitutional sites are indicated by subscripts "*k*" and "*h*". Note that, along the [0001] direction, the substitutional (S_{Si} and S_C) and tetrahedral interstitial (T_{Si} and T_C) sites are all located on the same row.

Such lattice relaxation may be caused by the impurity itself (a foreign atom that disturbs the crystal periodicity) or by the interaction between the impurities and neighbouring native defects (vacancies and interstitials). In principle, such impurity displacements are better described by a static displacement from the high-symmetry site. However, the relaxation effects may displace the impurities in various directions and by various distances, depending on the specific local structure of each impurity. The measured emission pattern can thus be a superposition of

a distribution of displaced sites in the vicinity of a high-symmetry site. In such cases, the occupied site may be relatively well described by the high-symmetry site with an rms displacement larger than the thermal vibration amplitude.

For each experiment, the electron emission yield was calculated for the emitter atom located on various lattice sites, within a range of ±3° of each considered crystal direction. An overview of the most important lattice sites in 3C- and 6H-SiC is given in Fig. 2.7 and Fig. 2.8. A multitude of potential interstitial sites exist for both structures; their yields were also simulated: (i) concerning the 3C-SiC, the tetrahedral interstitial sites with Si (T_{Si}) and C (T_C) nearest neighbours; interstitial sites along the <111> direction - bond center (BC), antibonding Si (AB_{Si}), antibonding C (AB_C), and the hexagonal site (H); interstitial sites along the <100> direction in either Si or C rows, i.e., the split interstitials (SP_{Si} and SP_C), the "C" sites with C_{2v} symmetry (C_{Si} and C_C) and the "Y" sites (Y_{Si} and Y_C) and interstitial sites along <110> direction, i.e. the "DS" sites (DS_{Si} and DS_C); (ii) concerning the 6H-SiC, substitutional Si (S_{Si}) and C (S_C) sites with varying isotropic rms displacements, a diversity of interstitial sites, such as tetrahedral (T), bond-centered (BC) and anti-bonding (AB) were also considered. At this point, it is important to note that for the 6H structure only a limited number of ideal substitutional and interstitial sites was considered and respective displacements between sites only along the c-direction. Displacements along directions basal to the c-axis were not investigated due to the fact that their implementation would have been rather difficult and calculations would have required excessive computing resources because of the elevated number of atoms in the large 6H unit cell. This polytype requires six Si-C bilayers to define the unit cell along the c-axis stacking direction (denoted also by [0001] direction), where two-thirds are cubic bonds and one-third hexagonal bonds. A layer (either Si or C layer) is said to be in hexagonal (*h*) configuration if it is surrounded on either side by layers of the same type. Conversely, it is said to be in cubic (*k*) configuration if it is surrounded on either side by layers of a different type [Lebedev2006, Capitani2007]. As a consequence, probes located on (*h*) and (*k*) substitutional (either Si or C) will produce different patterns. The patterns for ^{111}Ag probes sitting on substitutional Si hexagonal, cubic and a mixture of both (denoted as *h*+*k*), are illustrated in Fig. 2.9(b).

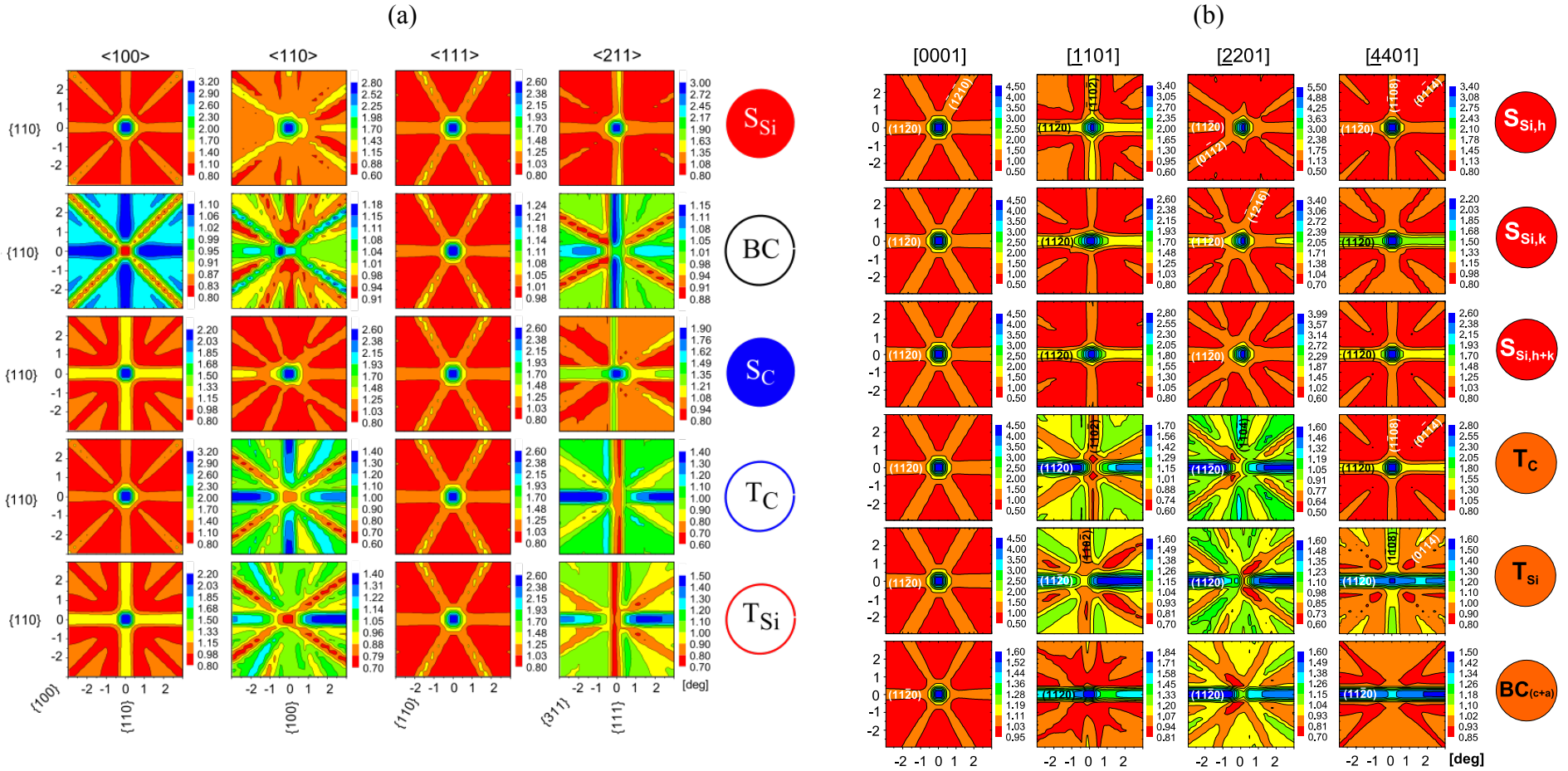

Figure 2.9. (a) Simulated ^{56}Mn β^- emission yield patterns in 3C-SiC for the sequence of sites along the <111> direction, $S_{Si} \rightarrow S_C \rightarrow T_C \rightarrow T_{Si}$, within ±3° from <100>, <110>, <111> and <211> directions. The patterns of S_{Si} and S_C sites are characterized by channeling peaks from all the four axial orientations shown as well as along all planes. For the interstitial T_{Si} and T_C sites one has, depending on the axial or planar direction, channeling or blocking effects. (b) Theoretical ^{111}Ag β^- angular emission yield patterns in 6H-SiC within ±3° of the four major crystallographic directions as simulated for the major substitutional and interstitial sites. The six rows represent the patterns for $S_{Si,h}$ (100% of emitter atoms on substitutional Si hexagonal), $S_{Si,k}$ (100% on substitutional Si cubic), $S_{Si,h+k}$ (mixture of 33.3% hexagonal and 66.7% cubic substitutional Si), T_C (100% on tetrahedral carbon-coordinated interstitial), T_{Si} (100% on tetrahedral silicon-coordinated interstitial) and BC(c+a) sites. These sites are identified in Fig. 2.8 and their definition can be found in [Lebedev2006, Capitani2007].

Note that the (*h*+*k*) mixture implies the presence of the emitter probes in both hexagonal and cubic substitutional Si sites with a statistical weight of 2/3 cubic and 1/3 hexagonal. The output of the *manybeam* calculations, for a given material, channeling axis and impurity isotope, consists of a two-dimensional emission pattern for each impurity lattice site and rms displacement u_1.

In Fig. 2.10(a) and 2.11(a), the emission yield patterns of S_{Si}, S_C, T_{Si} and T_C sites in 3C-SiC are all the same along the <111> direction and the same holds for the corresponding sites and the [0001] direction in 6H-SiC. For the <100> direction (3C-SiC), the same is observed for the pair S_{Si}, T_C sites and for the pair S_C, T_{Si} sites. Since the S_{Si}, S_C, T_{Si} and T_C sites are located on the same row along the <111> axis [figure 2.10(c)], they are all equivalent in the lattice projection onto the plane perpendicular to the <111> direction and, consequently, the corresponding <111> emission patterns are indistinguishable. Similarly, along the <100> direction, since S_{Si} is on the same row as T_C, and S_C is on the same row as T_{Si}, the corresponding <100> emission patterns are indistinguishable.

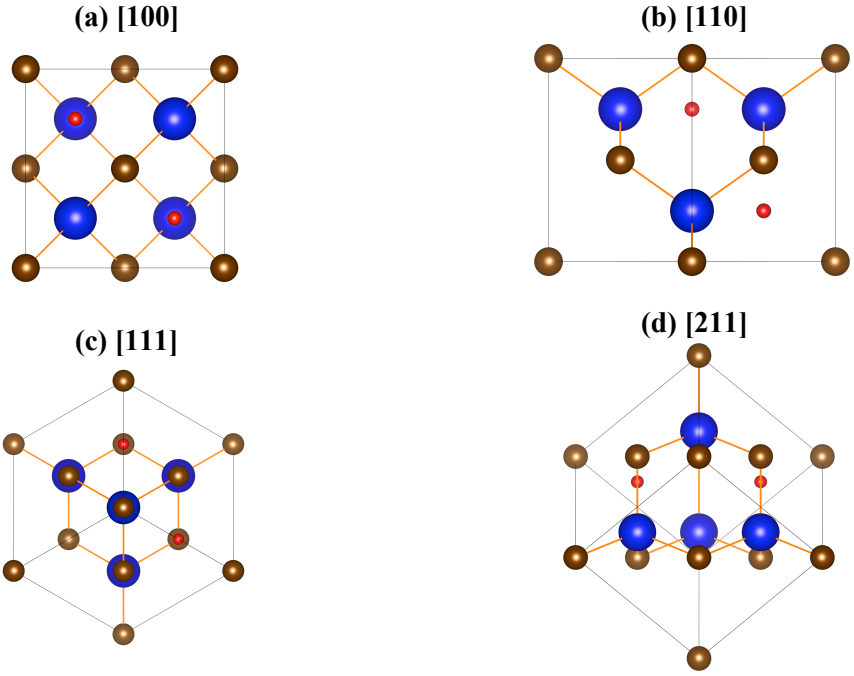

Figure 2.10. Schematic projections along the major crystallographic directions of a 3C-SiC crystal consisting of four unit cells. The positions of the interstitial tetrahedral C-coordinated T_C sites are also shown as small red circles. The bonds between Si (in blue) and C (in brown) atoms are indicated in orange.

In order to distinguish these sites, it is necessary to measure channeling patterns along the <110> and <211> directions, which puts the different sites in different rows [see figures 2.10(b) and 2.10(d)]. This results in emission patterns with clearly distinct anisotropies and thus allows for the unambiguous identification of the occupied lattice sites.

Concerning 6H-SiC, the probes sitting at S_{Si} sites are always aligned with rows and planes of Si atoms, which cause the emitted β^- particles to be channeled. Thus, an increase in the measured β^- count rate is expected along all axial and planar directions. On the other hand, for the interstitial T_C sites, maxima in the β^- count rate are expected along those directions with which the T_C sites are aligned, and minima along those where they are centred in the interstitial region, see Fig. 2.11. For instance, T_C sites are centred within (11$\underline{2}$0) planes and rows of Si and C atoms along the [0001] direction; they are also aligned with rows of Si atoms along [$\underline{4}$401] but are completely interstitial with respect to the [$\underline{1}$101] and [$\underline{2}$201] axis. This means that for T_C sites one expects to observe channeling effects along (11$\underline{2}$0), [0001] and [$\underline{4}$401] but minima along [$\underline{1}$101] and [$\underline{2}$201] directions.

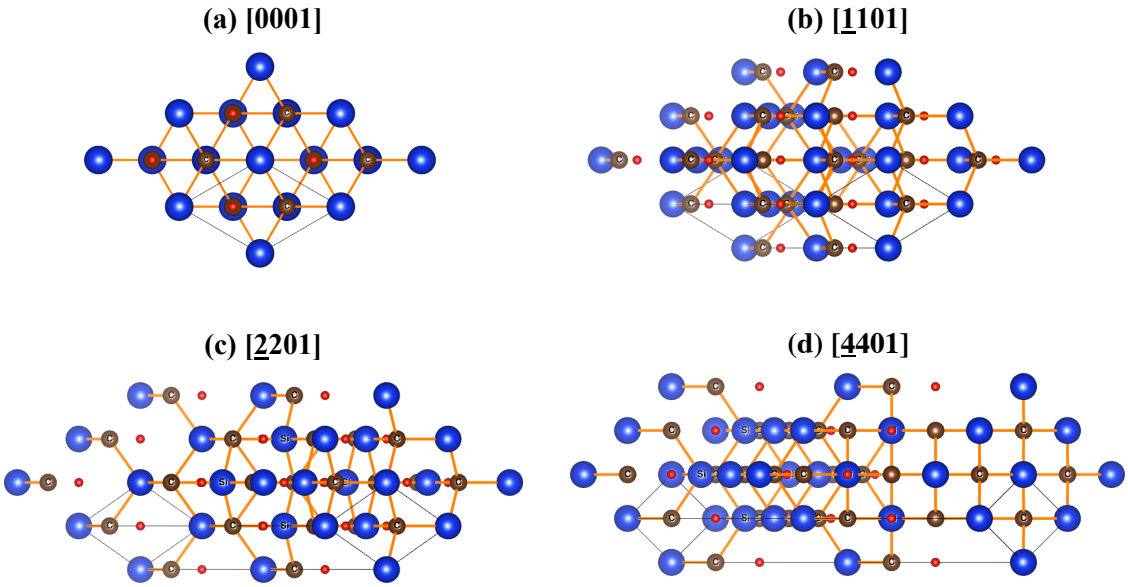

Figure 2.11. Schematic projections along the major crystallographic directions of a 6H-SiC crystal consisting of four unit cells. The positions of the interstitial tetrahedral C-coordinated T_C sites are also shown as small red circles. The bonds between Si (in blue) and C (in brown) atoms are indicated in orange.

The theoretical emission yields patterns are smoothed using a Gaussian with $\sigma \simeq 0.1^\circ$ to account for the contribution of the 1 mm beam spot to the experimental angular resolution. Higher values of σ may be used in order to account for, e.g., crystal mosaicity that may already exist in as-grown, imperfect samples or be a consequence of extended damage due to high fluence implantation. The size and shape of the detector pads is taken into account by averaging over the simulated yield falling within the angular range (0.26°×0.26°) of one pixel, resulting in the final theoretical emission pattern $\chi^{theo}(\theta,\phi)$. Fig. 2.9(a,b) shows the simulated emission patterns for ^{56}Mn and ^{111}Ag β^- emitters, in different sites of 3C- and 6H-SiC structures respectively, around different crystallographic directions, as an example for both structures.

Note that the simulated patterns obtained for the remaining probes used in this work are similar and not shown here.

2.5.2 Fitting procedure

Theoretical emission patterns are fitted to the experimental yields $\chi^{\text{theo}}(\theta, \phi)$, according to

$$\chi^{\exp}(\theta,\phi) = S[f_1\chi_1^{theo}(\theta,\phi) + f_2\chi_2^{theo}(\theta,\phi) + f_3\chi_3^{theo}(\theta,\phi) + 1 - f_1 - f_2 - f_3] \quad 2.5$$

where S is a scaling factor common to all angles in one pattern, which allows normalizing the count rate of experimental patterns and displaying them as normalized yield relative to isotropic emission and f_1, f_2 and f_3 denote the fractions of emitter atoms on up to three different lattice sites. The "random fraction", $f_R = 1 - (f_1 + f_2 + f_3)$, accounts for emitter atoms which cause negligible anisotropies in emission yield, i.e. which are located on sites of very low crystal symmetry or within heavily damaged or even amorphous surroundings or whose electrons are de-channeled by defects. A large random fraction may thus be the consequence of significant crystal damage from the implantation process. Up to seven fitting parameters S, f_1, f_2, f_3, x_0, y_0 and ϕ_0, may be simultaneously optimized using nonlinear least square fitting routines. The parameters S, x_0, y_0 and ϕ_0 are always allowed to vary in order to provide correct normalization of the experimental patterns and to achieve optimum translational and azimuthal orientation with respect to the detector.

2.5.3. Scattered electron background correction

In an emission channeling experiment, two types of electrons reach the detector: direct and scattered electrons. Those with initial direction towards the detector and which are not scattered under a wide angle, are direct electrons. The number of direct electrons is roughly given by the ratio between the solid angle Ω spanned by the detector relative to the beam spot and the full 4π solid angle into which all the electrons are isotropically emitted, i.e. $\Omega/4\pi$ of the total number of decays.

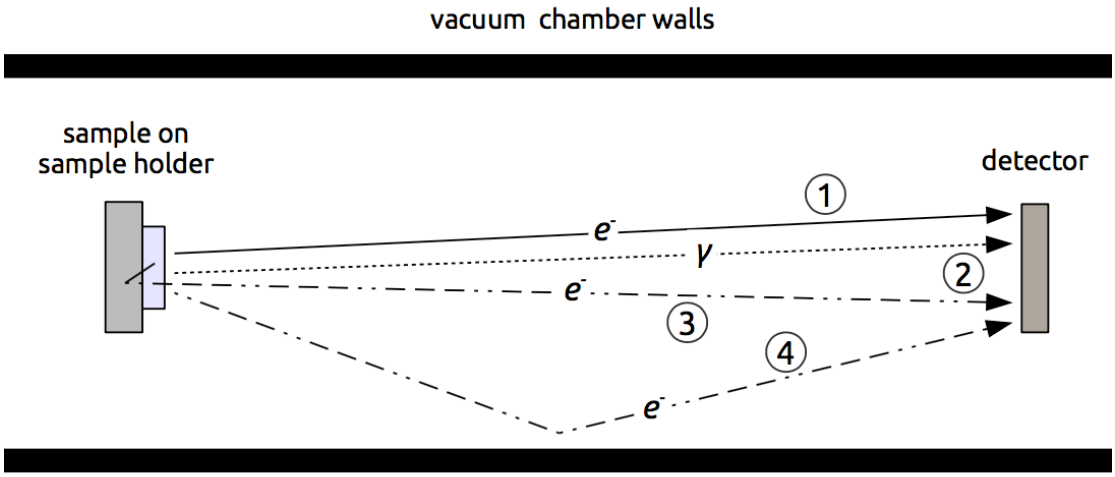

Figure 2.12. Typical particle tracks and related sources of background in electron emission channeling measurements. In (1) the detected electron is emitted from inside the sample directly towards the detector. γ-rays are also taken into account in (2). In (3) the emitted electrons from the probes are backscattered from the sample holder and in (4) from the chamber walls.

However, the number of detected electrons is always larger than this estimate. The additional scattered electrons are not emitted towards the detector initially, but still reach it after being scattered. The scattering event may occur inside the sample, when an electron is scattered by the host atoms, or outside the sample, by parts of the setup (including backscattering from sample holder), Fig. 2.12. These scattered electrons constitute an additional background in the experimental emission yields, which in good approximation is evenly distributed over the whole detector area, i.e. isotropic within the angular range of the measurement. This background cannot be taken into account in the theoretical framework of channeling that is implemented in the *manybeam* program. The problem is different for conversion electrons and β^- particles: (i) for a pure conversion electron decay, it is possible to deduce the total scattering background from the experimental energy spectrum. While, for direct electrons, the energy spectrum consists of a set of narrow peaks at well defined energies, the scattered electrons form tails at lower energies due to the energy lost in the scatter process. It is thus possible to correct for this scattering background by estimating (integrating the counts in the tails) and subtracting it from the experimental yields; (ii) because such a simple estimate is not possible for β^- decays with continuous energy spectra, De Vries [deVries2006] developed a computer program called *Pad* based on the Geant4 toolkit [Agostinelli2003, Allison2006]. Using the Monte-Carlo method, *Pad* simulates the propagation of electrons emitted from the sample and, among the ones that reach the detector, distinguishes the direct from the scattered ones. This requires detailed input information: the sample geometry and composition, the β^- decay energy spectrum (isotope-

specific) and the exact geometry of the setup – the position, shape and composition of the setup parts. From the *Pad* simulations it is possible to estimate the background correction factor *f* as

$$f = \frac{total\ electrons}{total\ electrons - scattered\ electrons} = \frac{total\ electrons}{direct\ electrons} \qquad 2.6$$

This *f* factor can in principle be used to correct the normalized experimental emission yields $\chi^{exp}(\theta, \phi)$ applying the equation:

$$\chi^{exp}_{corr}(\theta, \phi) = 1 + f \times [\chi^{exp}(\theta, \phi) - 1] \qquad 2.7$$

which is equivalent to subtracting the appropriate isotropic background contribution from the patterns before normalization. The more convenient approach, however, is to simply multiply the fitted fractions f_i obtained from eq. 2.5 with the correction factor *f*. Besides this correction factor, for experiments in which there is γ radiation, an extra background correction factor is estimated by comparing the count rate measured with, and without, a closed valve between the sample and the detector.

Table 2.2. The background correction factors f as deduced from simulations with the Pad code, corresponding to all the isotopes used in this work. E_{impl} is the implantation energy used for the various experiments.

3C-SiC				6H-SiC			
Isotope	Corr. Factor *f*	E_{imp} (keV)	Setup	Isotope	Corr. Factor *f*	E_{imp} (keV)	Setup
^{56}Mn	1.75	40	Pad6	^{56}Mn	1.75	40	Pad6
^{59}Fe	1.97	40	Pad1	^{59}Fe	2.12	60	Pad1
^{65}Ni	1.72	50	Pad6	^{65}Ni	1.71	30	Pad6
^{111}Ag	2.49	30	Pad4	^{111}Ag	2.07	30	Pad1
	2.71	30	Pad5		2.71	30	Pad5
^{124}In	1.72	50	Pad6		-	-	-

Table 2.2 gives an overview of the simulated correction factors *f* for all isotopes used in this work. Note that each value was simulated for the specific vacuum chamber (Pad1,…6) in which the actual experiment was conducted, taking into account also the emitter depth profiles resulting from the chosen implantation energy and the lower limit of electron detection used in the experiment, so a direct comparison of these values is not straightforward. As a general rule, however, it can be said that the background is lower in setups with relatively large diameters of the vacuum chamber and the tube leading towards the detector (pad1 and pad6), whereas more compact designs (pad4 and pad5) favour scattering of electrons into the detector.

References

[Agostinelli2003] S. Agostinelli, J. Allison, K. Amako *et al*., "Geant4 - a simulation toolkit", *Nucl. Instrum. Methods Phys. Res.* **506** 250–303 (2003).

[Allison2006] J. Allison, K. Amako, J. Apostolakis *et al*., "Geant4 developments and applications", *IEEE Trans. Nucl. Sci*. **53** 270–278 (2006).

[Capitani2007] G. C. Capitani, S. Di Pierro, G. Tempesta, "The 6H-SiC structure model: Further refinement from SCXRD data from a terrestrial moissanite", *Am. Mineral.* **92** 403–7 (2007).

[daSilva2013] M. R. da Silva, U. Wahl, J. G. Correia, L. M. Amorim, L. M. C. Pereira, "A versatile apparatus for on-line emission channeling experiments", *Rev. Sci. Instrum.* **84** 073506(1–8) (2013).

[Deicher2003] M. Deicher, G. Weyer, T. Wichert, "Solid state physics at ISOLDE", *Hyperfine Interact*. **151** 105–123 (2003).

[deVries2006] B. De Vries, "Lattice site location of impurities in group III nitrides using emission channeling", Ph.D. Thesis, Katholieke Univ. Leuven (2006).

[deMesquita1967] G. De Mesquita, "Refinement of the crystal structure of SiC type 6H", *Acta Crystallogr*. **23** 610–617 (1967).

[Fedoseyev2000] V. N. Fedoseyev, G. Huber, U. Köster, J. Lettry, V. I. Mishin, H. Ravn, V. Sebastian, "The ISOLDE laser ion source for exotic nuclei", *Hyperfine Interact*. **127** 409–416 (2000).

[Hofsäss1991] H. Hofsäss and G. Lindner, "Emission channeling and blocking", *Phys. Rep.-Rev. Sec. Phys. Lett*. **201** 121–183 (1991).

[Hofsäss1994] H. Hofsäss, U. Wahl, S. G. Jahn, "Impurity lattice location and recovery of structural defects in semiconductors studied by emission channeling", *Hyperfine Interact*. **84** 27–41 (1994).

[Hofsäss1996] H. Hofsäss, "Emission channeling", *Hyperfine Interact*. **97** 247–283 (1996).

[JANIS-JEFF] M. A. Kellet, O. Bersillon, R. W. Mills, "The JEFF-3.1/-3.11 Radioactive Decay Data and Fission Yields Sub-Libraries" (Nuclear Energy Agency, Paris, 2009, available from JANIS—Java-based Nuclear Data Information System, a software package from the OECD Nuclear Energy Agency http://www.oecd-nea.org/janis/).

[Jonson2000] B. Jonson, A. Richter, "More than three decades of ISOLDE physics", *Hyperfine Interact.* **129** 1–22 (2000).

[Kugler2000] E. Kugler, "The ISOLDE facility", *Hyperfine Interact*. **129** 23–42 (2000).

[Lebedev2006] A. A. Lebedev, "Heterojunctions and superlattices based on silicon carbide", *Semicond. Sci. Technol.* **21** R17–R34 (2006).

[Lindhard1965] J. Lindhard, "Influence of crystal lattice on motion of energetic charged particles", *Mat. Fys. Medd. Dan.Vid. Selsk.* **34(**14) 1–64 (1965).

[Peng1996] L. M. Peng, G. Ren, S. L. Dudarev, J. Whelan, "Robust parameterization of elastic and absorptive electron atomic scattering factors", *Acta Crystallogr.* A **52** 257–276 (1996).

[Peng2009] T. H. Peng, Y. F. Lou, S. F. Jin, W. Y. Wang, W. J. Wang, X. L. Chen, "Debye temperature of 4H-SiC determined by x-ray powder diffraction", *Powder Diffr*. **24** 311–314 (2009).

[Schulz1979] H. Schulz, K. H. Thiemann, "Structure parameters and polarity of the wurtzite type compounds SiC–2H and ZnO", *Solid State Commun*. **32** 783–785 (1979).

[Stelmakh2007] S. Stelmakh, E. Grzanka, M. Wojdyr, T. Proffen, S. C. Vogel, W. Palosz, B. Palosz, "Neutron diffraction studies of the atomic thermal vibrations in complex materials: application of the Wilson method to examination of micro- and nano-crystalline SiC", *Z. Kristallogr*. **222** 174–187 (2007).

[Thompson1973] M. W. Thompson, "An introduction to Channeling", in D. V. Morgan (Ed.), *Channelling: Theory, observation and applications* 1st ed, Bristol, Great Britain: John Wiley & Sons ltd, 1973, pp. 1–18.

[Wahl2000] U. Wahl, "Advances in electron emission channeling measurements in semiconductors," *Hyperfine Interact*. **129** 349 (2000).

[Wahl2004] U. Wahl, J. G. Correia, A. Czermak, S. G. Jahn, P. Jalocha, J. G. Marques, A. Rudge, F. Schopper, J. C. Soares, A. Vantomme, P. Weilhammer, "Position-sensitive Si pad detectors for electron emission channeling experiments", *Nucl. Instrum. Methods Phys. Res.* A **524** 245–256 (2004).

[Weilhammer1996] P. Weilhammer, E. Nygård, W. Dulinski, A. Czermak, F. Djama, S. Gadomski, S. Roe, A. Rudge, F. Schopper, J. Strobel, "Si pad detectors", *Nucl. Instrum. Methods Phys. Res.* A **383** 89-97 (1996).

[Ziegler2010] J. F. Ziegler, M. D. Ziegler, J. P. Biersack, "SRIM - The stopping and range of ions in matter", *Nucl. Instruments Methods Phys. Res.* B **268** 1818–1823 (2010).

[Zywietz1996] A. Zywietz, K. Karch, F. Bechstedt, "Influence of polytypism on thermal properties of silicon carbide", *Phys*. *Rev*. B **54** 1791–1798 (1996).

Chapter 3

Transition metal impurity lattice location in SiC

This chapter is based on the articles with title "Lattice location of implanted transition metals in 3C-SiC", published in Journal of Physics D: Applied Physics 50 215101 (2017) and "Lattice location of ion-implanted Mn, Fe and Ni in 6H-SiC", published in the journal Semiconductors Science and Technology 33 015021 (2018), and on a manuscript with the title "Lattice location of implanted ^{111}Ag in 3C- and 6H-SiC" (to be submitted). In all cases the emission channeling technique was used to extract crucial information about lattice location of TM atoms and their interaction with defects in their vicinity, as a function of annealing temperature from room temperature up to 900 °C for Mn, Fe and Ni, while Ag implanted samples were annealed as high as 1075 °C. While the motivation for these studies was given in chapter 1 and general experimental procedures discussed in chapter 2, results are presented and summarized in this chapter.

3.1. Lattice location of 3*d* and 4*d* TMs in 3C-SiC and 6H-SiC

The lattice location of the radioactive isotopes ^{56}Mn, ^{59}Fe, ^{65}Ni and ^{111}Ag implanted into 3C-SiC and 6H-SiC single crystals was investigated by means of the EC technique as function of the annealing temperature. ^{56}Mn, ^{59}Fe, ^{65}Ni and ^{111}Ag decay to the stable isotopes ^{56}Fe, ^{59}Co, ^{65}Cu and ^{111}Cd by means of β^- emission, and the EC technique is based on the observation of anisotropic β^- intensity patterns emitted from the radioactive probe atoms embedded in single

crystals (cf. sect. 2.1). Depending on the lattice site of the emitter atoms, the β^- particles may be guided, or channeled, by the crystal potentials within a few degrees of the principal crystallographic axes, on their way out of the crystal. The angular distribution of the emitted β^- particles, which can be measured with a position sensitive electron detector, depends on both the crystallographic axis and on the position of the emitting atoms within the lattice. The resulting experimental angular emission patterns are then compared with *manybeam* simulations [Hofsäss1991] for emitter atoms on substitutional silicon and carbon sites and various interstitial positions, which permits identifying and quantifying the probe atom site occupancy (cf. sect. 2.5). Specifically, for ^{59}Fe:3C-SiC, the results will also be compared with the results obtained from ^{57}Mn$\rightarrow$^{57}Fe emission Mössbauer spectroscopy [Gunnlaugsson2006, Bharuth2008]. Concerning the 6H-SiC material, *manybeam* simulations were previously applied to analyse the lattice location of the rare earth isotope ^{169}Tm in 6H-SiC [Vetter2003], but at that time only substitutional Si sites were considered, and without any distinction between hexagonal (*h*) and cubic (*k*) sites.

Undoped single-crystalline cubic 3C-SiC samples with <100> oriented surfaces were used, all obtained from Hoya Corporation (Japan), and doped *n*-type 6H-SiC single crystal samples were cut from a c-axis oriented wafer obtained from CrysTec GmbH. Mass separated and chemically clean beams of radioactive isotopes were provided by the on-line isotope separator ISOLDE-CERN facility [Jonson2000]. The transition metal radioisotopes were produced by fission of uranium carbide UC_2 targets, induced by 1.4 GeV proton beams from the CERN PSB, followed by chemically selective laser ionization and electromagnetic mass separation. For the Mn, Ni and Ag experiments, the short-lived isotopes ^{56}Mn ($t_{1/2}$=2.58 h) and ^{65}Ni (2.52 h) and the long-lived ^{111}Ag (7.45 d) were implanted directly. Since ISOLDE cannot produce clean beams of Fe isotopes, in order to study the lattice location of this element the short-lived precursor ^{59}Mn (4.6 s) was implanted, which decays into the long-lived ^{59}Fe (44.5 d). Note that during the decay of ^{59}Mn, the ^{59}Fe daughter atoms receive on average a recoil of 200 eV, assuring their re-implantation and thus avoiding any influence from the previous site of ^{59}Mn. The implantations were carried out at room temperature under vacuum better than 10^{-5} mbar and at an angle of 17° from the <0001> surface to avoid channeling implantation and produce well-defined depth profiles. SRIM [Ziegler2010] simulations show that each implanted ^{56}Mn, ^{59}Fe, ^{65}Ni and ^{111}Ag ion produces around 600-800 vacancies and interstitials. The corresponding range, straggle and peak concentrations estimated for Gaussian implantation profiles, for both SiC polytypes, are listed in table 3.1.

Table 3.1. Implantation energy and fluence for the various experiments. The corresponding projected range, straggling and peak concentrations were calculated by SRIM [Ziegler2010].

SiC polytype	TM probe	Implantation energy [keV]	Fluence [cm^{-2}]	Projected range R_p [Å]	Straggling [Å]	Peak concentration [cm^{-3}]
3C	^{56}Mn	40	2×10^{13}	256	93	8×10^{18}
	^{59}Fe	40	3×10^{13}	259	98	1×10^{19}
	^{65}Ni	50	6×10^{13}	298	110	2×10^{19}
	^{111}Ag	30	1×10^{14}	157	43	6×10^{19}
		30	6×10^{12}			4×10^{18}
6H	^{56}Mn	40	9×10^{12}	256	93	4×10^{18}
	^{59}Fe	60	2×10^{13}	362	127	6×10^{18}
	^{65}Ni	30	4×10^{13}	196	73	2×10^{19}
	^{111}Ag	30	1×10^{14}	157	43	6×10^{19}
		30	2×10^{13}			1×10^{19}

The β^- emission yields were measured within ±3° of the crystallographic directions <100>, <110>, <111> and <211> of 3C-SiC and [0001], [$\underline{1}$101], [$\underline{2}$201] and [$\underline{4}$401] of 6H-SiC at room temperature in the as-implanted state and after each annealing step, using a position and energy sensitive electron detector [Wahl2000, Wahl2004]. Effects due to the background from γ-rays and β^- particles scattered by the chamber walls were corrected as follows. The contribution from γ-rays was determined by measuring the background count rate when a shutter was placed in front of the detector, resulting in ~10% of the β^- count rate for the experiments presented here. In order to assess the background of scattered electrons a Monte Carlo computer code based on the GEANT4 toolkit was used [Agostinelli2003], that takes into account the composition and geometry of the sample, the sample holder, the detector and the major parts of the vacuum setup. Combining both estimates showed that for ^{59}Fe only ~50% and for ^{56}Mn and ^{65}Ni ~54% and for ^{111}Ag ~35%-45% of the count rate resulted from β^- particles directly emitted from the sample towards the detector. Since the remaining background events do not contribute to the measured channeling effect, the fractions of probe atoms on specific lattice sites, obtained by the fitting procedures described below, were multiplied by corresponding correction factors.

Theoretical β^- emission yield patterns for ^{56}Mn, ^{59}Fe, ^{65}Ni and ^{111}Ag were obtained with the *manybeam* formalism for electron channeling in single crystals [Hofsäss1991, Wahl2000] for all relevant high symmetry sites in the SiC zincblende and 6H structures such as the substitutional Si and C sites. Regarding these *manybeam* simulations, the reader is advised to consult section 2.5.1, for a more detailed description.

The two-dimensional experimental patterns were fitted by considering different fractions of

TM probe nuclei occupying several different lattice sites. The fitting procedures comparing the theoretical yields and experimental patterns take into account the angular resolution of the detection setup and are described in section 2.3; for a more in-depth description, the reader can consult the reference [Wahl2004]. Note that the experimental results can only be satisfactorily described if, in addition to the fractions of probe atoms on regular sites, also a fraction of probe atoms on low-symmetry (random) sites is allowed, which contributes with an isotropic emission yield.

3.2. Lattice location of the 3*d* TMs ^{56}Mn, ^{59}Fe and ^{65}Ni in 3C-SiC and 6H-SiC

3.2.1. 3C-SiC: ^{56}Mn, ^{59}Fe and ^{65}Ni fitting process

In the fitting process were first considered only single fractions on regular sites and the conclusion was that two main types of sites contribute to the best fits, depending on the annealing temperature. For low annealing temperatures (< 500 °C) the best single fraction fits for all three investigated transition metals were obtained with the ideal tetrahedral, carbon coordinated interstitial site (T_C). In contrast, for the annealing temperatures above 500 °C, the best single fraction fits were obtained for ideal substitutional silicon (S_{Si}) sites. Indeed, it is possible to visually identify this site change for all three measured TM probes by comparing the <110> and <211> direction patterns (Fig. 3.1, 3.2 and 3.3) to the corresponding patterns for the various substitutional and tetrahedral interstitial sites [Fig. 2.9(a)].

The patterns in Fig. 3.1 are best described assuming that the TM probe atoms are in an interstitial site. However, in Fig. 3.2 and 3.3, the patterns are characteristic for probe atoms in substitutional sites. The next step in the analysis was to allow the fitting routine to include simultaneously two ideal lattice sites. In this case the combination of ideal S_{Si}+T_C sites gave the best fit with a 50% improvement of the chi square (χ^2) compared to the single fraction fit.

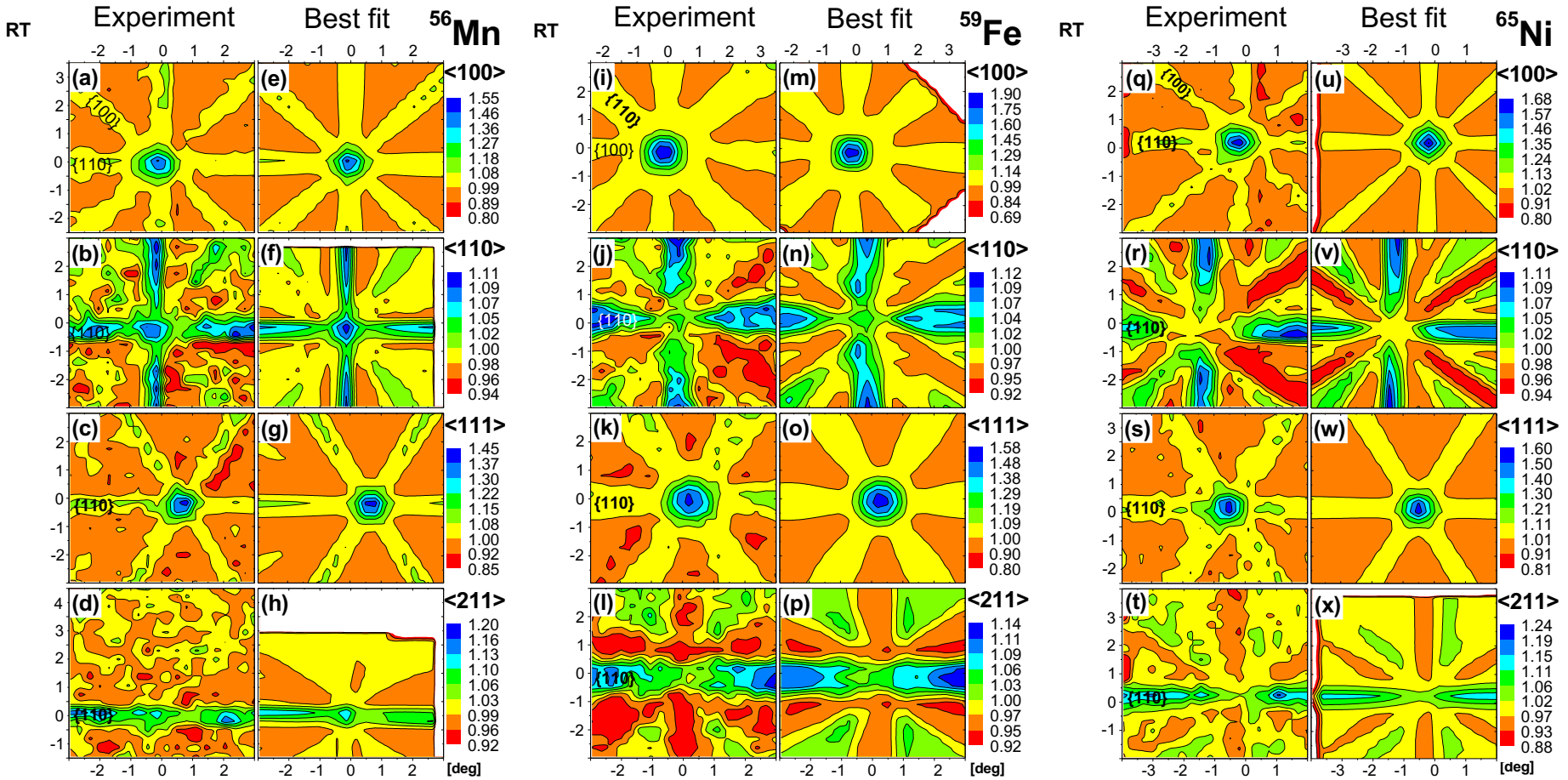

Figure 3.1. Normalized experimental β^- emission channeling patterns and corresponding best fits for a combination of near S_{Si} and ideal T_C sites, along the <100>, <110>, <111> and <211> directions following ^{56}Mn (a-d), ^{59}Fe(i-l) and ^{65}Ni (q-t) implantations in 3C-SiC at room temperature. Note that in some cases the crystal was oriented during the experiment in such a way that the recorded patterns included areas which were further than 3° away from the major crystallographic direction. Since the *manybeam* simulations were restricted to an angular range of ±3° from the axes, the corresponding areas along the edges or corners of the patterns (f), (h), (m), (u) and (x) are shown in white.

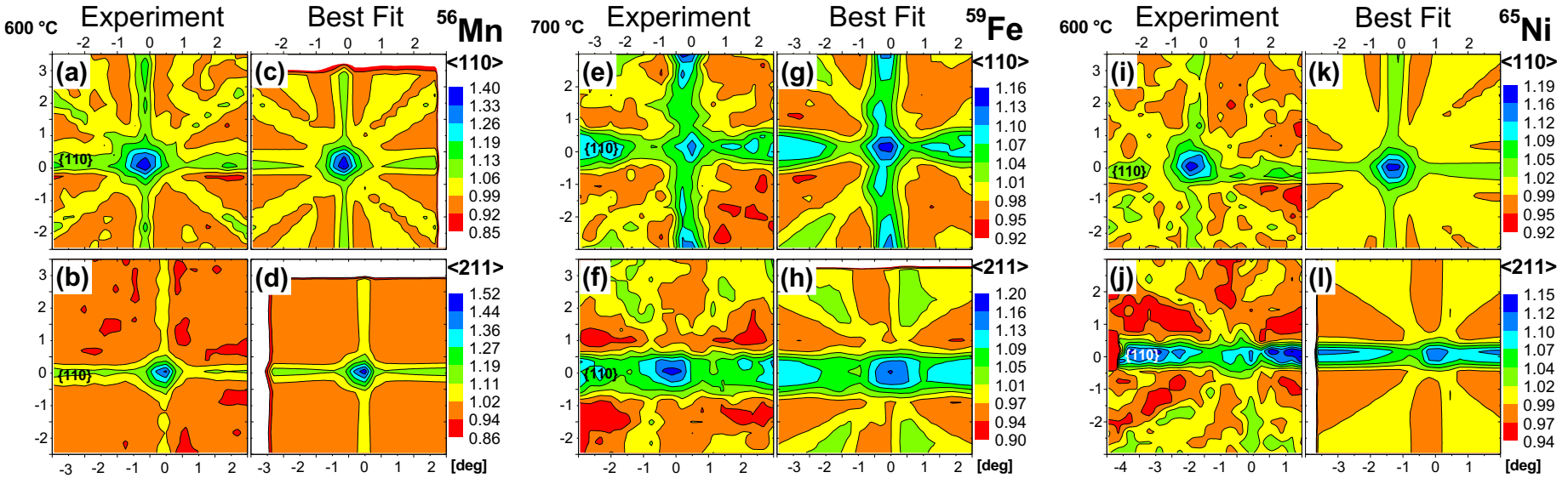

Figure 3.2. Normalized experimental β^- emission channeling patterns from ^{56}Mn (a, b), ^{59}Fe (e, f) and ^{65}Ni (i, j) in 3C-SiC and corresponding best fits for a combination of near S_{Si} and ideal T_C sites, around the <110> and <211> directions following annealing above 500 °C.

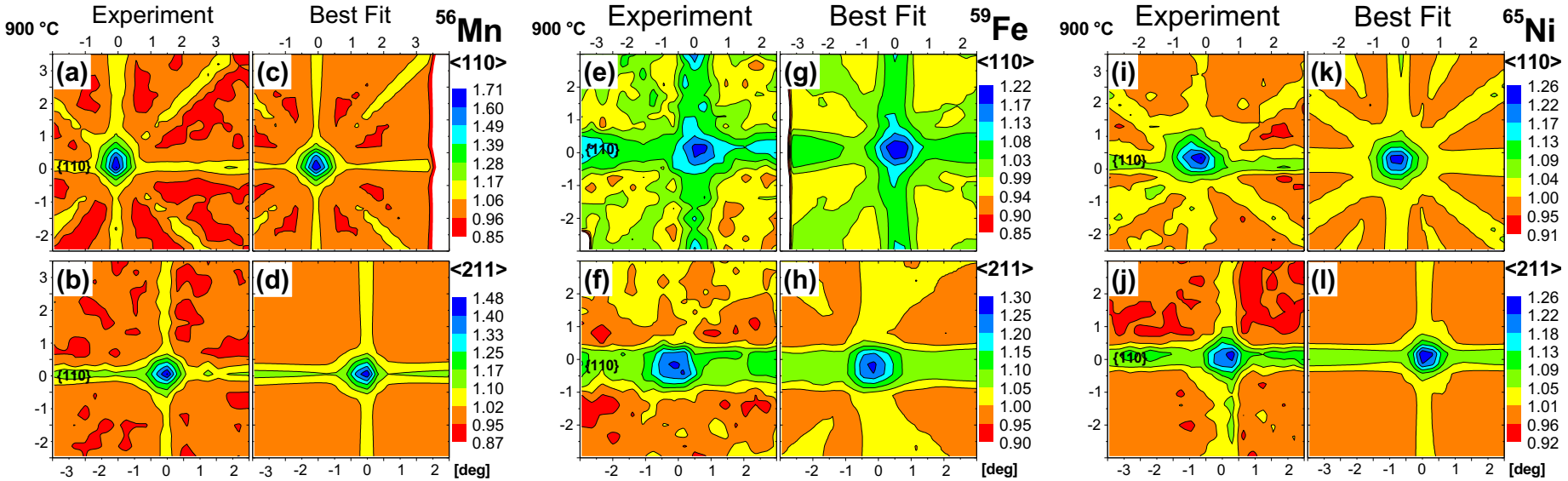

Figure 3.3. Normalized experimental β^- emission channeling patterns from ^{56}Mn (a, b), ^{59}Fe (e, f) and ^{65}Ni (i, j) in 3C-SiC and corresponding best fits for a combination of near S_{Si} and ideal T_C sites, in the vicinity of the <110> and <211> directions following annealing at 900 °C.

In order to further improve χ^2, the possibility for the simultaneous occupancy of sites that are displaced from the ideal S_{Si} or T_C positions was explored. However, displacements from the ideal T_C site did not improve fit quality, in contrast to fixing the T_C site on its ideal position and allowing the other site fraction to move away from the S_{Si} site along <111> directions towards neighbouring AB_{Si} or BC sites, or along <100> directions towards SP_{Si} sites, or along <110> directions towards DS_{Si} sites.

The normalized chi squares obtained from fits to the <110> and <211> patterns as a function of displacement from ideal S_{Si} sites are shown in Fig. 3.4. Note that experimental channeling patterns along the <100> and <111> axial directions are not suitable for such a fit since both T_C and S_{Si} sites are located within rows of Si atoms along those directions. The <100> and <111> channeling patterns resulting from ideal T_C and slightly displaced S_{Si} sites are hence too similar and the fits tend to become unstable. The dashed and full arrows in Fig. 3.4 indicate the TM probe positions which resulted in minimum chi squares of <110> and <211> fits. This suggests that the three transition metal atoms are slightly displaced (~0.1-0.3 Å) from the ideal S_{Si} sites. However, the improvements in the χ^2_{norm} for displacements along the different axial directions were, for all isotopes and annealing temperatures, below 4% and hence not very pronounced. It was therefore not possible to identify unambiguously the direction of the displacements. The χ^2_{norm} values *vs* displacement for Fe are presented as an example in Fig. 3.4(b, d, e); this also applies to the other TM atoms studied in the present investigation.

A detailed analysis for the ^{59}Fe measurements following various annealing temperatures can be found in appendix A. Taking the displacement from S_{Si} to AB_{Si} as an example, Fig. 3.5 shows the site for which the best two-site fit was obtained as a function of annealing temperature for all three isotopes. The displacement decreases in all three cases to values <0.1 Å following annealing at 900 °C, indicating the local recovery of the damaged lattice leading to better incorporation of the TM impurities on the substitutional Si position.

Although the direction of a displacement from substitutional sites could not be pinpointed, our results on the other hand clearly rule out TM atoms on BC positions (which are prominent for some TM atoms in Si [Wahl2005, Wahl2006, Silva2013, Silva2014a, Silva2016]) within the framework of two-site fits.

Possibilities for more than two regular sites being occupied were also explored. In particular, tetrahedral interstitial Si-coordinated (T_{Si}) and carbon substitutional (S_C) sites as well as bond-centred positions were also analysed. For example, a combination of the sites S_{Si}+T_C+T_{Si} yielded for T_{Si} fractions that were always negative or very close to zero. Similarly, three-site

fits allowing for S_C (S_{Si}+T_C+S_C) also gave χ^2 reduced by <5%.

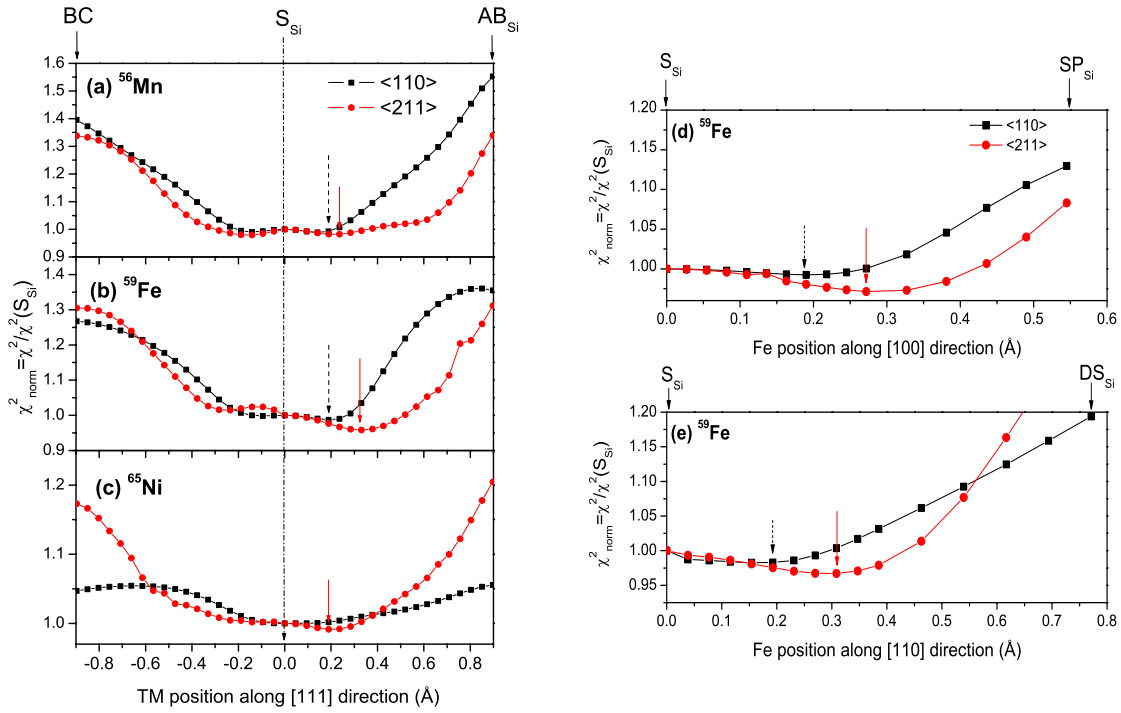

Figure 3.4. Normalized χ^2_{norm} of two-site fits to <110> and <211> patterns as a function of displacement from ideal S_{Si} for ^{56}Mn (a), ^{59}Fe (b) and ^{65}Ni (c) in 3C-SiC. While the first site was kept fixed at the ideal tetrahedral carbon interstitial (T_C), the position of the second site was moved in small steps along the <111> direction from S_{Si} towards AB_{Si} and BC. In the ^{59}Fe case, displacements along <100> towards SP_{Si} (d) and along <110> towards DS_{Si} sites (e) are also presented. The χ^2 was in all cases normalized to that for the two-site fit of ideal T_C and ideal S_{Si}. The dashed and full arrows indicate the displacement positions where the lowest χ^2 was obtained. All graphs in this figure refer to RT as-implanted measurements; in the case of ^{59}Fe corresponding plots for measurements after annealing have been included in the appendix A.

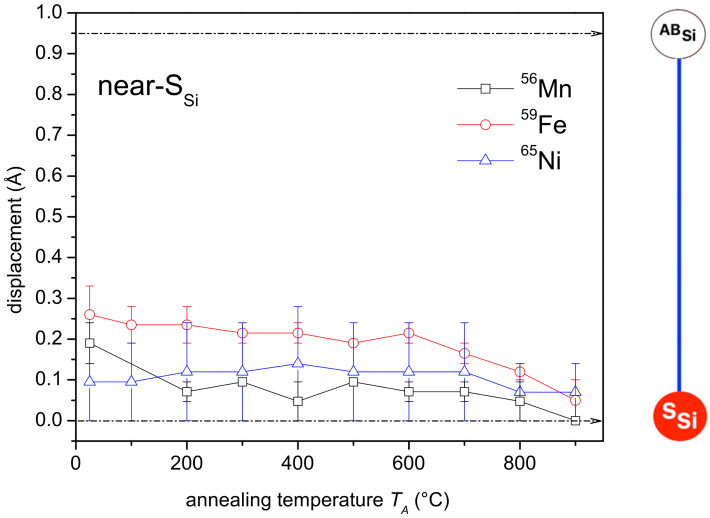

Figure 3.5. Displacements of the TM impurities ^{56}Mn, ^{59}Fe and ^{65}Ni from the ideal S_{Si} towards the AB_{Si} site in 3C-SiC as a function of annealing temperature as derived from best two-site fits with the first site kept fixed at the ideal T_C position.

3.2.2. 6H-SiC: ^{56}Mn, ^{59}Fe and ^{65}Ni fitting process

The experimental angular-dependent β^- emission patterns for all crystallographic directions measured for the three probes ^{56}Mn, ^{59}Fe and ^{65}Ni in the RT as-implanted state are shown in Fig. 3.6, while Fig. 3.7 displays [$\underline{1}$101] and [$\underline{2}$201] patterns following annealing at 400 °C for Mn and Ni and at 600 °C for Fe, and Fig. 3.8 following annealing at 600 °C for Mn and Ni and at 900 °C for Fe. Direct comparison of Fig. 3.6 to the theoretical patterns in Fig. 2.9(b) shows that T_C sites provide the best visual match to the RT as-implanted experimental results.

According to what has been said above, the T_C site preference is best visible from the [$\underline{1}$101] and [$\underline{2}$201] patterns since the T_C sites are not aligned with these directions. However, there are certain features in the experimental patterns for which a mere T_C site occupancy cannot account, in particular the fact that weak central axial peaks remain along [$\underline{1}$101] and [$\underline{2}$201] directions. A more quantitative analysis is achieved by fitting the experimental yields with linear combinations of up to three theoretical patterns from high symmetry sites plus a constant angular distribution from so-called "random sites". Note that this "random fraction" corresponds to probe atoms on low-symmetry sites, e.g. in highly damaged surroundings, which causes isotropic electron emission. In the fitting process, first only single fractions on regular sites were considered, to find that two main types of sites contribute to the best fits, depending on the annealing temperature. For low annealing temperatures (<400 °C) the best fits for all three investigated TMs were obtained with the tetrahedral, carbon coordinated, interstitial site T_C. For annealing temperatures above 400 °C, the best fits resulted from the probe atoms occupying ideal $S_{Si,h+k}$ sites. The next step was to allow the fitting routine to include simultaneously two ideal lattice sites. For all studied TM probes, the combination of $S_{Si,h+k}$+T_C gave the best fit and considerably improved the chi square of fit (χ^2) compared to the single fraction fit by up to 50%. Hence no indications were found that the TM site preference deviates from the statistical mixture of 1/3 (*h*) hexagonal- and 2/3 (*k*) cubic-like substitutional sites in the 6H crystal, and in the following, when S_{Si} is mentioned, this is always to be understood as a statistical mixture of Si sites. Next, the situation was explored where more than two sites are being occupied. In particular, tetrahedral interstitial Si-coordinated (T_{Si}) and carbon substitutional S_C, either (*h*), (*k*) or a mixture of both (*h*+*k*) were used as third fraction in the fits. While this reduced χ^2 somewhat further, but always <5%, the combinations S_{Si}+T_C+T_{Si} and S_{Si}+T_C+S_C resulted in T_{Si} and S_C fractions that were close to zero or negative. Hence the conclusion is that large fractions on T_{Si} or S_C sites can be excluded.

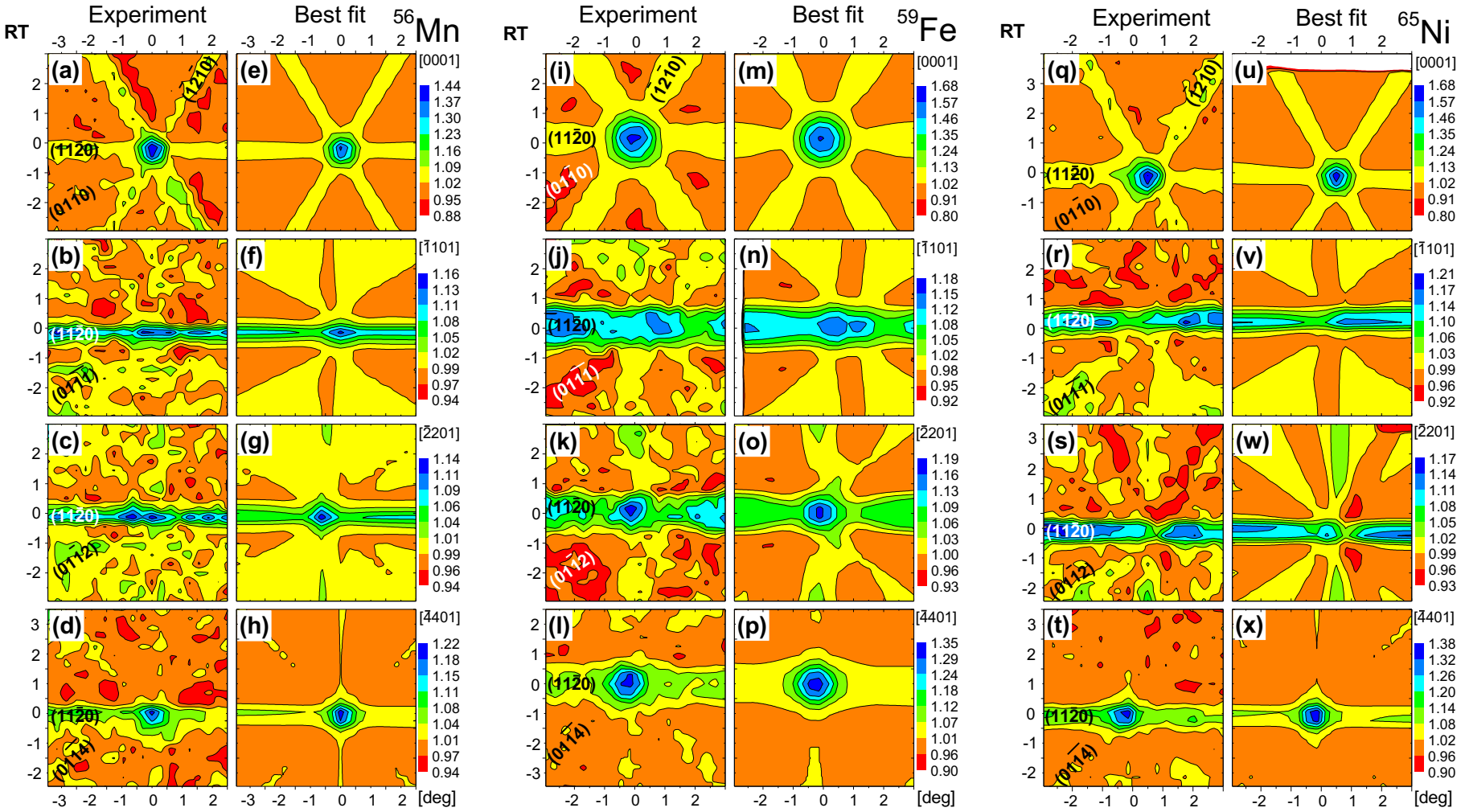

Figure 3.6. Normalized experimental β^- emission channeling patterns and corresponding best fits for a combination of ideal $S_{Si,h+k}$ and T_C sites, in the vicinity of [0001], [1̲101], [2̲201] and [4̲401] directions following ^{56}Mn (a)-(h), ^{59}Fe (i)-(p) and ^{65}Ni (q)-(x) implantation at RT.

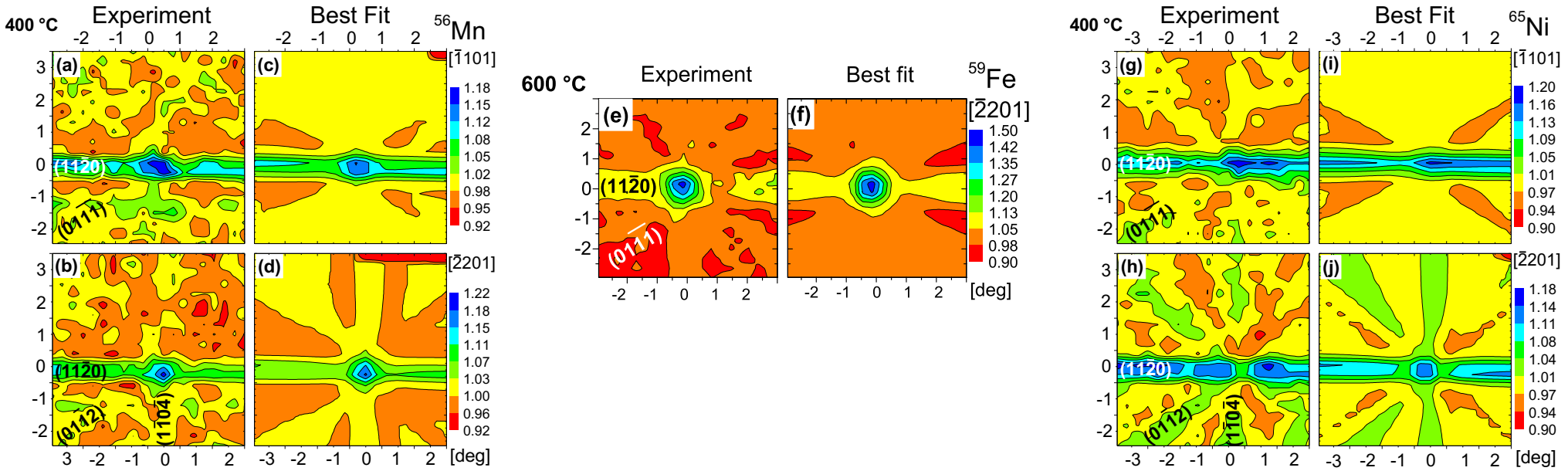

Figure 3.7. Normalized experimental β^- emission channeling patterns from ^{56}Mn (a), (b), and ^{65}Ni (g), (h) in 6H-SiC and corresponding best fits for a combination of ideal $S_{Si,h+k}$ and T_C sites in the vicinity of [1̲101] and [2̲201] directions following annealing at 400 °C. In the ^{59}Fe (e) case, the pattern was collected only in the vicinity of the [2̲201] direction after annealing at 600 °C (e), and also the best fit (f) using the ideal (S_{Si}+T_C) sites combination.

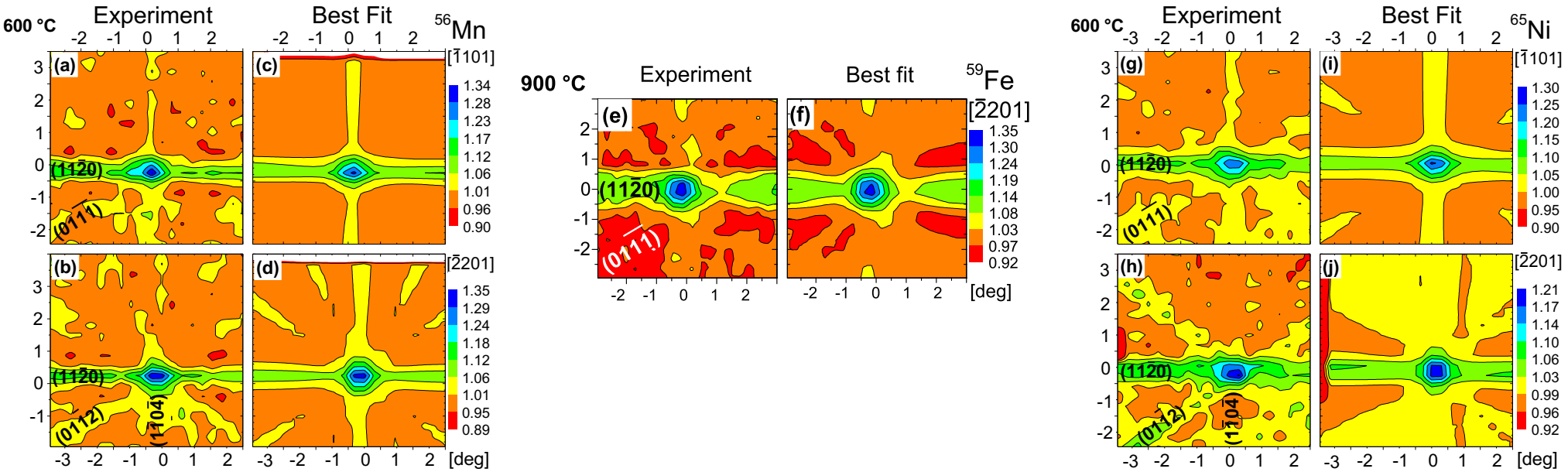

Figure 3.8. Normalized experimental β^- emission channeling patterns from ^{56}Mn (a), (b) and ^{65}Ni (g), (h) in 6H-SiC and corresponding best fits for a combination of ideal S_{Si} and T_C sites, in the vicinity of the [1101] and [2201] directions following annealing at 600 °C. In the ^{59}Fe (e) case, the experimental β^- emission channeling pattern was collected only in the vicinity of [2201] direction after annealing at 900 °C, and also the best fit (f) using the ideal (S_{Si}+T_C) sites combination.

3.2.3. Discussion

For the fraction analysis of the TM:3C-SiC samples as a function of annealing temperature presented in Fig. 3.9 and discussed in the following, the fits were confined to two lattice positions: ideal interstitial T_C sites and near substitutional Si sites plus random sites. However, since the analysis results with S_C, T_{Si} or BC as third sites are inconclusive, one cannot exclude the possibility that these positions are occupied to some smaller extent by the TM probes. Fig. 3.9(d)-(f) show the fitted fractions for the two considered sites, ideal tetrahedral carbon-coordinated interstitial T_C, and near substitutional Si, and 'random' sites that give isotropic emission distribution, as a function of annealing temperature for all three transition metals. The ideal T_C sites dominate the patterns in the as-implanted state with 28% for ^{56}Mn, 50% for ^{59}Fe and 40% for ^{65}Ni, in contrast to only 15%, 11% and 7%, respectively, on near S_{Si} sites. This situation remains unchanged following annealing up to 400 °C for ^{65}Ni, 500 °C for ^{56}Mn and 600 °C for ^{59}Fe. Then the TM fractions on ideal T_C sites decrease with further annealing, visible by the vanishing of the blocking planes around the <110> and <211> directions, whereas the TM fractions on near S_{Si} sites increase, visible by the presence of electron channeling anisotropy peaks in both directions (Fig. 3.2 and 3.3). In all samples the sum of the two fitted fractions stays below 100% throughout the measurements, with the remaining fraction located at random sites. While the increase of the fractions on near substitutional Si sites follows the decrease of the ideal T_C site fractions to some extent, at the same time the sum fractions decrease, which means that some of the TM atoms are moving to random positions instead of occupying S_{Si}. This observation suggests that the TM atoms located at T_C positions are probably isolated, with no Si vacancies available in their vicinity.

For the TM:6H-SiC fraction analysis as a function of annealing temperature, shown in Fig. 3.9(a)-(c), the fits were confined to the two regular lattice positions ideal interstitial T_C and ideal substitutional S_{Si}, plus random sites. While the best fit results for the TM emission channeling patterns contain always a mixture of the TM probes on these two lattice sites, the contributions change considerably as a function of annealing temperature.

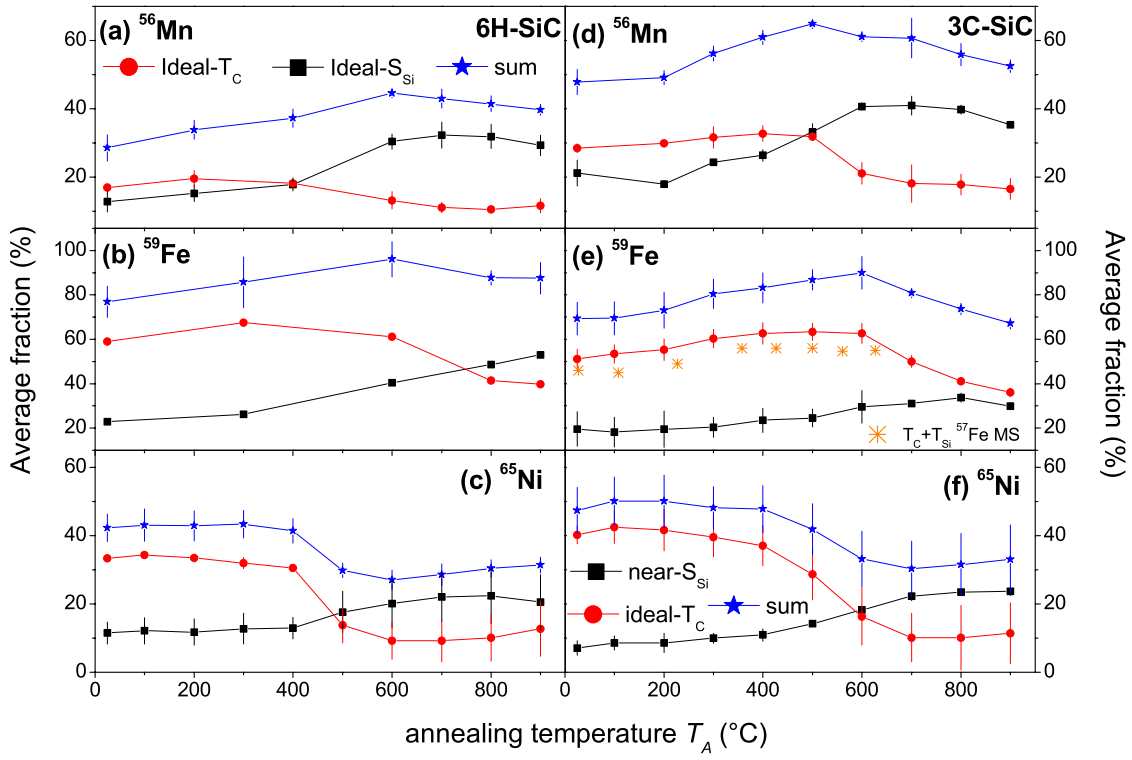

Figure 3.9. 6H-SiC fitted fractions of ^{56}Mn (a), ^{59}Fe (b) and ^{65}Ni (c) emitter atoms on ideal substitutional Si (in black) and ideal tetrahedral T_C sites (in red) plus the sum of both site fractions (in blue) as a function of the annealing temperature, averaged for the four measured crystallographic directions. The error bars represent the spread in fitted fractions for the different crystallographic directions. Fitted fractions for ^{56}Mn (d), ^{59}Fe (e) and ^{65}Ni (f) in 3C-SiC are also plotted for comparison, and have the same colour schematics. In panel (e) the sum fraction of ^{57}Fe* on interstitial (T_{Si}+T_C) sites derived from the Mössbauer experiments of reference [Bharuth2008] is shown by the orange stars.

In case of the 6H sample, for the as-implanted state the best fits for the ^{56}Mn probe are shown in Fig. 3.6(e)–(h) with 17% on T_C sites and 13% on $S_{Si,h+k}$, in Fig. 3.6(m)-(p) for ^{59}Fe with 59% on T_C and 23% on S_{Si}, and in Fig. 3.6(u)–(x) for ^{65}Ni with 33% on T_C and 12% on S_{Si}. Hence in all three cases the T_C sites dominate in the as-implanted state and this situation remains rather unchanged for annealing up to 400 °C for Mn and Ni, and up to 600 °C for Fe, cf Fig. 3.7 and 3.8. With further annealing, the TM fractions on T_C sites decrease whereas the fractions on $S_{Si,h+k}$ sites increase, so that presently in the [1̲101] and [2̲201] patterns of Fig. 3.8 electron channeling effects are visible for all axial and planar directions.

As can be seen from Fig. 3.9, the lattice site preferences as a function of annealing temperature are very similar for the two polytypes. In both 6H and 3C for ^{56}Mn and ^{59}Fe the sum fractions increase for annealing temperatures up to 550-600 °C, while no such increase is observed for ^{65}Ni and the sum fractions decrease simultaneously with the site change from T_C to S_{Si}. In emission channeling, growth of the sum fraction on regular sites, i.e. a reduction of the random fraction, is most commonly associated with the annealing of implantation damage. It hence

seems as if this damage annealing was much less pronounced in the Ni-implanted samples, possibly as a consequence of the fact that they received the highest fluences and damage was more persistent against annealing. The sum of the fractions on S_{Si}+T_C sites in both ^{59}Fe experiments was a factor of 1.5-2 higher than in case of ^{56}Mn and ^{65}Ni, with ^{59}Fe sum fractions reaching above 90% at T_A=600 °C. While this could in principle be a consequence of the different chemical properties of the TMs, there may be other explanations. The total fluences of both ^{59}Fe experiments were a factor of 2-3 lower than in case of ^{65}Ni but overlapping with those of ^{56}Mn, so fluence-related effects may have played a minor role, although there must be other factors that come into play. A major difference between the ^{59}Fe and ^{56}Mn or ^{65}Ni experiments is that samples with the long-lived isotope ^{59}Fe (44.5 d) were produced via the implantation of the short-lived (4.6 s) precursor ^{59}Mn and that the samples were then stored for several weeks at RT before the measurements started. The decay of ^{59}Mn happens several seconds after the actual implantation that creates the damage in the sample. Since the ^{59}Fe nucleus receives ~200 eV of recoil, it will leave the original lattice site of ^{59}Mn and then find its new lattice site when a large part of the initial radiation damage has already been removed during the cool down of the damage cascade to RT. Further annealing may then have occurred during the prolonged sample storage at RT before the measurements started. In contrast, the short-lived probes ^{56}Mn and ^{65}Ni are directly introduced into their lattice during the cool-down of the damage cascade, which may favour their incorporation in sites of low symmetry that are not resolved as specific regular lattice sites in the channeling measurements and therefore form part of the "random" fraction of emitter atoms.

Several theoretical works [Miao2003, Medvedeva2003, Machado2015, Wright2016] have suggested that the 3*d* transition metal impurities, from a thermodynamic point of view, should preferentially replace the host lattice Si atoms. It is estimated from SRIM [Ziegler2010] (for a temperature of 0 K, i.e. neglecting dynamic thermal annealing) that each implanted TM atom creates around 300-400 Si vacancies, as well as a similar number of C vacancies and the corresponding interstitials. The initial vacancy distribution is approximately described by a Gaussian profile centred at somewhat more than half of the projected range of the implantation. The created damage therefore offers ample possibilities for TMs to be incorporated in various types of lattice sites and forming complexes with other crystal defects. Especially, since ion implantation is a process that happens far from thermodynamic equilibrium, implanted impurities may therefore also occupy sites that are not the most stable from an energetic point of view. As mentioned above, a smaller fraction of TM atoms were found occupying S_{Si} sites in the as-implanted state, while the major fraction remained on interstitial sites. It is thus

feasible that during annealing interstitial TM atoms may react with Si vacancies, leading to their incorporation on substitutional Si lattice sites. Indeed, concerning the TM atoms found on S_{Si} sites, their fractions increase with annealing temperature but, as mentioned before, this increase does not totally reflect the observed loss in the T_C fraction after annealing above 400-500 °C. Furthermore, the total fitted TM sum fractions stay always below 100% (Fig. 3.9). The following aspects contribute in providing a possible explanation for this behaviour.

First, irradiation-induced silicon mono-vacancies (V_{Si}) have been theoretically predicted [Wimbauer1997, Petrenko2001] and experimentally observed [Kawasuso1998, Itoh1997]. Itoh *et al*. [Itoh1989], by using electron spin resonance, had found three annealing stages for the so called T1-center, which was later [Kawasuso1998, Itoh1997] identified by the same authors as a negatively charged silicon vacancy: at 150 °C, 350 °C and 750 °C. Based on *ab initio* theoretical modeling, Bockstedte *et al.* proposed the following mechanisms for the V_{Si}^- annealing stages [Bockstedte2004]: (i) initial recombination of Frenkel pairs with small separation between the Si vacancy and interstitial, having a low activation energy barrier of 0.2 eV; (ii) recombination of vacancies and interstitials with a larger separation that is limited by diffusion of the interstitials with a migration barrier of 1.4 eV; (iii) in intrinsic or compensated material V_{Si}^- was predicted to be metastable, transforming into a carbon vacancy-antisite complex ($V_{Si} \rightarrow V_C$-C_{Si}) with an energy barrier of 2.5 eV. This latter value was in reasonable agreement with the activation energy of 2.2 eV observed by Itoh *et al.* [Itoh1989] related to the final annealing stage of the T1 center. Also, since irradiated SiC will eventually become compensated due to the electrical activity of deep defects, the transformation $V_{Si} \rightarrow V_C$-C_{Si} may also occur in samples that were initially *n*-type and hence be a general characteristic of heavily irradiated SiC.

Second, reports on transition metal diffusion in SiC are scarce [Danno2012, Takano2001]; the most detailed work available [Takano2001] studied the tracer diffusion of Fe, Cr and Co in microcrystalline 3C-SiC using macroscopic characterization of the diffusion profiles in the temperature range 700-1600 °C. In the case of Fe, the temperature dependence of the diffusion coefficient D was expressed by $D=8.7\times10^{-11}\ \mathrm{cm^2\ s^{-1}}\ \exp(-1.15\ \mathrm{eV}/k_BT)$. As was noted by the authors of reference [Takano2001], the small value of the activation energy E_D=1.15 eV points towards an interstitial mechanism of diffusion. However, the pre-exponential factor $D_0=8.7\times10^{-11}\ \mathrm{cm^2\ s^{-1}}$ which they derived is many orders of magnitude smaller than what one expects for typical interstitial migration, where D_0 should be in the range $1\text{-}10^{-3}\ \mathrm{cm^2\ s^{-1}}$ [Mehrer2007]. Below, arguments will be given to why the activation energy for TM diffusion

E_D is likely to be higher than 1.15 eV. Nonetheless, the finding that Fe long range diffusion was observed at temperatures around 700 °C remains valid, and if one uses the above formula from reference [Takano2001] one estimates that the mean diffusion width $(6Dt)^{1/2}$ during a 10 min anneal at 700 °C would be ~59 Å.

Third, there are effects related to implantation damage and its annealing. Due to this damage, some of the implanted TM dopants are embedded in defective regions. Also, electrons emitted by probe atoms located in defect-free crystalline surroundings may travel through regions of extended damage, both of which increases the de-channeling probability and thus cause the electron emission to be more isotropic. SiC has strong chemical bonds and hence implantation-induced defects have reduced mobility, thus requiring annealing at temperatures above 1400 °C for near-perfect crystal lattice recovery. Nevertheless, several experimental studies [Jiang2001, Jiang2009, Usman2010] showed that for low fluences of implanted heavy ions ($<10^{15}$ cm^{-2}) considerable recovery is already achievable at annealing temperatures below 600 °C. So, the overall fraction increase observed up to 500 °C does not necessarily mean that more TM dopants occupy the corresponding lattice sites but likely is a sign of the local recovery of the defective host lattice.

If it is assumed that the decrease of the fractions on T_C sites is caused by the onset of interstitial TM diffusion, one can estimate the activation energy E_M for this migration process by using an Arrhenius model as described e.g. in references [Wahl2006, Silva2013, Silva2014a]:

$$E_M = k_B T \ln\left[\frac{\nu_0 \Delta t_{ann}}{N \ln\left(\frac{f_{n-1}}{f_n}\right)}\right]$$

Here ν_0 is the attempt frequency, which is taken here as 10^{12} s^{-1}, i.e. of the order of the lattice vibrations, Δt_{ann} the annealing time, T the annealing temperature, f_n the interstitial fraction after annealing at T, f_{n-1} the fraction before the annealing at T and N the required number of steps before an interstitial TM atom combines with a silicon vacancy or reaches a random position. Two opposite scenarios for N were considered: (1) an upper limit estimate for the migration energy E_M is obtained if one jump is considered enough to move a TM atom into a Si vacancy or a random position; (2) reaching a lower limit estimate for E_M requires making reasonable assumptions on the maximum number of jumps N_{max} that take place before the TM_i reaches a Si vacancy or a random position. Here one may assume that this is quite likely if the diffusion induced broadening of the TM depth profile would reach a value that corresponds to the projected range R_p of the implantation. This would mean that a large fraction of TM probes

would reach the surface or diffuse so deep into the sample that the channeling effects would be damped considerably due to de-channeling. Both cases, diffusion to the surface and into the depth of the sample, lead to a loss of channeling effects, which shows as decrease in the sum fraction of emitter atoms. Note that since such a decrease in the sum fractions is as a matter of fact observed in SiC for temperatures above 500-600 °C, this scenario with N_{max} is actually not unlikely. The diffusion-induced broadening resulting from a number of N jumps can be estimated by $(r_M^2 N/3)^{1/2}$, where r_M is the mean jump width. If one assumes that r_M is given by the closest distance between two interstitial C-coordinated T_C sites, which is 3.08 Å along 3C-SiC <110> and along 6H-SiC [$\underline{2}$201] directions, one estimates N_{max} from R_p via $N_{max}=3[R_p/r_M]^2$.

Looking at the estimated values for the TM_i migration energies E_M presented in table 3.2, the following comments are appropriate. First, since the fraction of interstitial Fe(T_C) decreases only at higher annealing temperatures (T_A=600-900 °C) than in the case of Mn and Ni (T_A=400 °C-700 °C), the estimated E_M for Fe (3.0 eV) is higher than for Mn and Ni (2.6 eV and 2.4 eV). Second, the range of TM_i migration energies overlaps with the activation energy of the third V_{Si} annealing stage (2.2 eV [Itoh1989] - 2.5 eV [Bockstedte2004]), where the metastable Si vacancy supposedly converts to a complex V_C-C_{Si} antisite defect. This could provide an explanation why not all of the TMs that were initially interstitial are incorporated in substitutional Si sites: if Si vacancies are depleted and there are no other stable lattice sites for diffusing TMs to be found, long-range diffusion and subsequent incorporation in random sites will occur.

Table 3.2. Estimates for the interstitial migration energy E_M of the TMs considering two different scenarios for the number of jumps: N=1 and N=N_{max}. For the last scenario, the value of N_{max} is estimated using the assumptions described in the text.

	6H-SiC			3C-SiC		
TM element	$E_M(N=1)$ [eV]	$E_M(N=N_{max})$ [eV]	N_{max}	$E_M(N=1)$ [eV]	$E_M(N=N_{max})$ [eV]	N_{max}
Mn	2.7	1.9	20720	2.6	1.9	
Fe	3.2	2.3	41440	3.0	2.2	≈16180
Ni	2.3	1.7	12150	2.4	1.7	

Fe in SiC has also been investigated using $^{57}Mn \rightarrow ^{57}Fe$ Mössbauer spectroscopy (MS) studies, in 3C-SiC by Bharuth-Ram *et al*. [Bharuth2008] and in 6H-SiC by Gunnlaugsson *et al.* [Gunnlaugsson2006]. The MS technique gives information on the charge distribution in the local environment of the probe atom via the hyperfine interaction and can thus be seen as a complementary technique to the EC method, which reveals the position of the probe atoms

with respect to the three-dimensional lattice but lacks sensitivity to their immediate local environment. The comparison of ^{59}Fe lattice location (via EC of emitted electrons) and ^{57}Mn$\rightarrow$^{57}Fe hyperfine interaction (via MS of emitted gamma particles) thus offers the possibility of obtaining a more detailed understanding. In the MS experiments, the radioactive probe ^{57}Mn ($t_{1/2}$=1.45 min) was implanted at ISOLDE as a function of temperature, simultaneously to MS measurements taking place during the subsequent decay of the well-known 14.4 keV excited Mössbauer state ^{57}Fe* (98 ns), which is populated by β^- decay of ^{57}Mn.

Following room temperature implantation into 3C-SiC Bharuth-Ram *et al*. [Bharuth2008] report on the presence of ~15% of ^{57}Fe probes at substitutional sites (with no possibility of distinguishing between C and Si sites) and ~20% each on tetrahedral interstitial C and Si sites. The site fractions were evaluated up to ~600 °C implantation temperature, where the substitutional fraction had increased to ~20%, the fraction at T_C sites to ~50% and the fraction at T_{Si} sites almost disappeared to ~5%. The site change from $T_{Si}\rightarrow T_C$ was explained as a thermally activated jump to a more stable position during the 140 ns life time of the ^{57}Fe* Mössbauer state, which allowed deriving an activation energy of 0.8(2) eV for this jump. Similar results had been obtained earlier in 6H-SiC [Gunnlaugsson2006]. Starting the comparison between results by addressing first Fe on T_{Si} sites, as already stated before, EC experiments were unable to detect the occupation of more than two sites. Although a combination of three sites was tried (S_{Si}+T_C+T_{Si}), in this case the T_{Si} fraction was close to zero (<5%) after implantation and then reached a negative fraction in the earlier annealing stages. According to the MS results, the absence of Fe on T_{Si} sites would be perfectly understandable since, with an activation energy of 0.8 eV, the transformation to the more stable T_C sites would require only ~1 min at room temperature, thus taking place already during the implantation, which took about one hour for this sample, and in any case long before the start of the measurements with the ^{59}Fe isotope of 45 d half-life. On the other hand, the total interstitial fraction (T_{Si}+T_C) seen by MS, which has also been included in Fig. 3.9(e), remains relatively constant at 45-56% in between RT and 600 °C, which is rather similar to the value obtained by EC, i.e. 50-60% for the T_C site. Finally, concerning the substitutional site, EC also finds a similar fraction at RT with 11%, on the near S_{Si} site and similar annealing trend reaching also a fraction of ~20% at 600 °C. Note that site changes from T_C to S_{Si} with E_M=2.2-3.0 eV, as were observed by ^{59}Fe EC around 700 °C, should not be visible by MS, since, for ^{57}Fe* to make one such jump during its 140 ns life time, temperatures above ~1900 °C would be

required. Summarizing, taking into account the different annealing time scales to which the experimental methods are sensitive, in the case of Fe it was found good agreement with the results of ^{57}Mn→^{57}Fe Mössbauer spectroscopy.

Finally, a comparison between the current experiments on ^{56}Mn, ^{59}Fe and ^{65}Ni in 3C-SiC to previous lattice location results that were obtained for the same probe atoms in silicon [Wahl2005, Wahl2006, Silva2013, Silva2014a, Silva2016] and to ^{59}Fe in diamond [Bharuth2003], will also be made. A striking difference is that in Si (with the exception of highly p^+-doped Si, cf the remark below), the major lattice sites in the RT as-implanted state were sites that in a perfect lattice would be located in the vicinity of the bond-center positions. The understanding of the authors of [Wahl2005, Wahl2006, Silva2013, Silva2014a, Silva2016] was that these are TMs that are located within multi-vacancy defects such as divacancies and hexa-vacancy rings. As was discussed above, although one cannot rule out a smaller fraction of TMs in such positions in SiC, they are certainly not the dominating lattice sites. In contrast, in SiC the dominating lattice sites in the RT as-implanted state were in all cases ideal C-coordinated interstitial T sites. The type of site changes from interstitial to substitutional sites that were obvious in SiC were probably not observed in Si since they would take place at much lower temperatures: the interstitial TMs obtained during RT implantation in Si should be diffusing so rapidly [E_M(Mn)=0.7 eV, E_M(Fe)=0.67 eV, E_M(Ni)=0.47 eV] that they immediately get attached to traps in the lattice. The interpretation presented in this thesis is that in SiC this interstitial migration process is much slower, with activation energies in the 2-3 eV range, so that it is promoted during annealing well above RT and then leads to the increased incorporation of TMs in substitutional Si but also in random sites. In contrast, interstitial sites near the tetrahedral position were generally not observed as dominating TM lattice sites in Si unless the samples were annealed to 600-700 °C. Although the nature of this type of interstitial sites in Si is not entirely clear, they seem to be associated with long-range TM diffusion and subsequent trapping in the $R_p/2$ region around half of the implanted range. It should be mentioned that highly p^+-doped Si is a special case since positively charged TM metals are stabilized on or close to tetrahedral interstitial sites also at room temperature as a consequence of pairing reactions with negatively charged B^- acceptors.

In case of diamond, lattice location data only exist for ^{59}Fe [Bharuth2003]. In stark contrast to both SiC and Si, no interstitial Fe could be seen in diamond, whereas the type of substitutional

site was similar to the case of both SiC polytypes, i.e. characterized by displacements smaller than ~25% of the distance to the BC site.

3.2.4. Conclusions

In this work the TM impurity lattice location in both 3C-SiC and 6H-SiC polytypes was experimentally determined. Following ion implantation into 3C-SiC, the 3*d* transition metals Mn, Fe and Ni show similar behaviour. Similar results were also observed after ion implantation into 6H-SiC. Despite the existence of two different sublattices in SiC, in all cases the TMs are preferentially found on interstitial T_C and substitutional S_{Si} sites. This confirms those theoretical predictions, which have suggested that TMs in SiC are most stable in C-coordinated positions [Miao2003, Medvedeva2003, Machado2015, Wright2016]. Specifically, for 6H-SiC no indications were found for a deviation of the TM distribution on the substitutional Si sites from the statistical mixture of 1/3 hexagonally (*h*) and 2/3 cubically (*k*) coordinated positions. Whereas in the RT as-implanted state 3*d* TMs on ideal T_C sites were the prominent species, thermal annealing induced site changes from T_C to both S_{Si} and random sites. These site changes are attributed to the onset of migration of interstitial TMs, for which activation energies of E_M=1.7 eV-3.2 eV are estimated in this work, valid for both polytypes. There are strong indications that a major feature that can explain characteristic differences in the lattice sites of 3*d* TMs in Si and SiC, is that the migration of interstitial TMs occurs much slower in SiC than in Si. Also, in contrast to Si, incorporation of TMs in sites near the BC position (which are associated with TMs within multi-vacancy complexes) seems to be largely absent. At the highest annealing temperatures, the TM atoms increasingly populate random sites in both 6H and 3C-SiC. Consequently, it is considered that the transformation of V_{Si} to the V_C-C_{Si} complex is as important for TMs in the 6H as in the 3C polytype and provides in both cases a possible explanation of why silicon vacancies are unavailable as major traps following annealing at higher temperatures, since this happens in a temperature regime where the transformation of $V_{Si} \rightarrow V_C$-C_{Si} has been suggested.

Overall, no indication was found that the wider band gap and the existence of hexagonally and cubically coordinated sites in 6H-SiC alter the behaviour of implanted transition metals in comparison to its cubic 3C counterpart.

In summary, the lattice location of 3*d* TMs in SiC is influenced to a large extent by their ability to interact with other defects and form complexes with them, which will also determine their deep level properties. The Si site was directly and unambiguously identified as the preferred

3*d* TM lattice site. Consequently, the interaction of interstitial TMs with Si vacancies is of particular relevance and any mechanism that depletes or introduces V_{Si} in SiC will play also a critical role for the TM lattice site occupation.

3.3. Lattice location of the 4*d* TM ^{111}Ag in 3C-SiC and 6H-SiC

3.3.1. 3C-SiC: ^{111}Ag fitting process

Similar to the cases of ^{56}Mn, ^{59}Fe, and ^{65}Ni described above, also for the ^{111}Ag fitting process initially only one single fraction on regular sites was considered. However, while for Mn, Fe and Ni at lower annealing temperatures interstitial T_C sites were found as dominating positions, for Ag at all annealing temperatures the best fits were obtained with near substitutional Si sites. As already observed for the other TMs, the improvements in the χ^2_{norm} for displacements along different axial directions from the ideal Si site were below 4% and therefore it was not possible to unambiguously identify the direction of the displacements. On the other hand, for both of the ^{111}Ag:3C-SiC samples visual comparison of the experimental patterns with the best fit for near substitutional Si sites (Fig. 3.10 and Fig. 3.11) shows that not all details in the experimental results are being reproduced by the single-site fits. The experimental patterns for the lowest fluence (6×10^{12} cm^{-2}) Ag sample in the vicinity of <110> and <211> directions are shown in Fig. 3.10(a)-(b) in the as-implanted state and after annealing at 700 °C in Fig. 3.10(e)-(f). When comparing with the corresponding best fit plots Fig. 3.10(c)-(d) and Fig. 3.10(g)-(h) one notices that the maxima of axial channeling yields in the best fit patterns are generally smaller than the experimental ones and also the shape and intensity of the effects do not reproduce all experimental details. These visually observed discrepancies point to the possibility that a second site might be populated by the Ag probes.

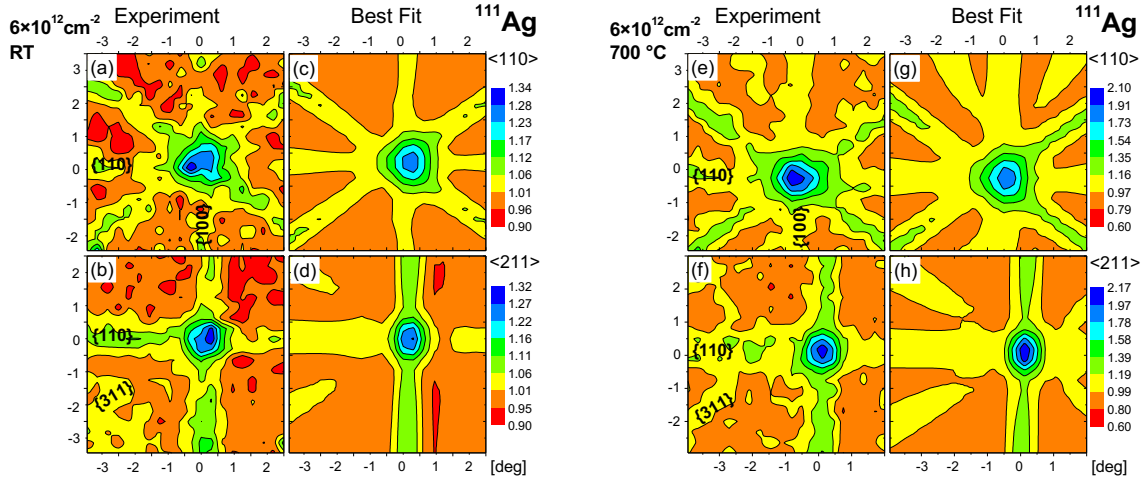

Figure 3.10. Normalized ^{111}Ag:3C-SiC (lowest fluence, 6×10^{12} cm^{-2}), experimental β^- emission channeling patterns at room temperature (a)-(b), and after annealing at 700 °C (e)-(f) and corresponding best one-site fits with near S_{Si} sites in the vicinity of <110> and <211> directions. Note that the maxima of the axial channeling yields in the simulations are generally smaller than the experimental ones and also that the shape and intensity of the planar effects do not show perfect matches. These visually observed discrepancies point to the existence of a second site populated by the Ag probes.

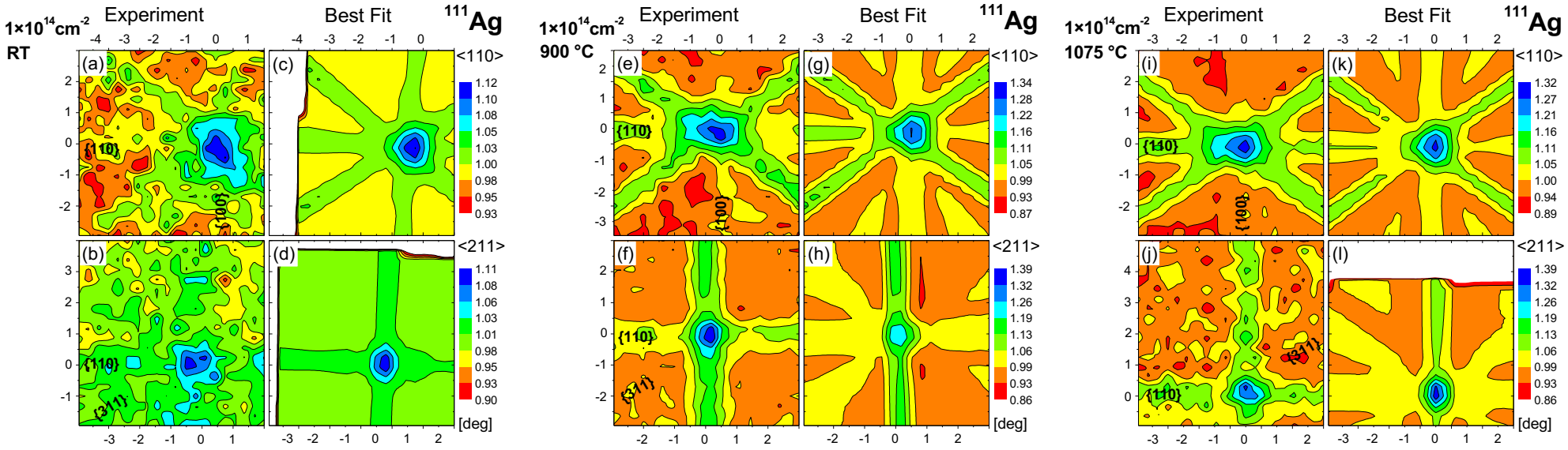

Figure 3.11. Normalized ^{111}Ag:3C-SiC (highest fluence, 1×10^{14} cm^{-2}) experimental β^- emission channeling patterns at room temperature (a)-(b), and after annealing at 900 °C (e)-(f) and 1075 °C (i)-(j) and corresponding best one-site fits with near S_{Si} site in the vicinity of <110> and <211> directions. Note that for this experiment, the ^{111}Ag:3C-SiC experimental patterns at room temperature are well described by one-site fits with Ag probes sitting at near S_{Si} site. Similarly to the ^{111}Ag:3C-SiC implanted sample with lowest fluence (Fig 3.10), at high annealing temperatures discrepancies are observed between the experimental and best fit patterns, which point to the existence of a second site populated by the Ag probes. In particular, maxima of axial channeling yields in the best fit patterns tend to be smaller than the experimental ones and also the shape and intensity of the effects (most notably <211>) do not entirely well reproduce experimental results.

Similarly, the experimental patterns for the 1×10^{14} cm^{-2} Ag implanted sample are shown in Fig. 3.11(a)-(b) after implantation, (e)-(f) after 900 °C annealing and (i)-(j) after 1075 °C annealing. Here one notices that in particular following the 900 °C and 1075 °C annealing steps the one-site fits fail to describe all details of the experimental patterns. Most striking is the fact that the best fit patterns show channeling effects for some planes which are quite weak or absent in the experimental results, e.g. along the {100} plane [vertical in panels 3.11(g) and 3.11(k)] or the {311} planes [diagonal in panels 3.11(h) and 3.11(l)]. Also, the shape of the <110> axial effects is rather poorly reproduced by the one-site fits. On the other hand, for the as-implanted patterns, discrepancies are not that obvious since in this case the overall anisotropy of the effects is quite weak (less than half in comparison to after annealing), resulting in the fact that statistical fluctuations become much more prominently visible and complicate a detailed comparison. As we will briefly discuss in the following the considerable difference in Ag fluence is a decisive factor that must always be taken into account when assessing these two experiments.

Several authors [Jiang1999, Jiang2009, Jiang2010, Debelle2010, Miranda2012], studied the damage build-up in the most common SiC polytypes following the implantation of ions such as He^+, C^+, Si^+, Fe^+ or Au^{2+}, in the hundred keV to MeV range and implanted at different temperatures. Jiang *et al*. [Jiang1999], implanted three ions of different masses (He^+, C^+, Si^+) with energies ranging between 390-550 keV, in 6H-SiC single crystals in the temperature range of 180-190 K. Their results suggested that the permanent damage that is actually retained in the sample for similar values of initial displacements per atom (dpa), increased with the ion mass. Also, it was observed that, for example, an implanted fluence of 10^{15} C^+ cm^{-2} was enough to amorphize the 6H-SiC host lattice at a temperature of 180 K. In other works done by Jiang *et al*. damage build-up studies in nanocrystalline and single crystal 3C-SiC films were made using 2 MeV Au^{2+} and 1 MeV Si^+ ions, implanted at ~160 K and RT, respectively [Jiang2009, Jiang2010]. In those cases, the authors observed the amorphization of the 3C-SiC single crystal film at fluences of $\sim2\times10^{13}$ Au^{2+} cm^{-2} (160 K) and $\sim6\times10^{14}$ Si^+ cm^{-2} (RT). Debelle *et al*. [Debelle2010] implanted 100 keV Fe^+ ions in both 6H- and 3C-SiC single crystals at RT. Both structures were amorphized by a fluence of $\sim3\times10^{14}$ Fe^+ cm^{-2}. Amorphization of 6H-SiC was also reported following 150 keV RT implantation of 5×10^{14} Fe^+ cm^{-2} [Miranda2012]. All these experiments are helpful in providing a general idea how the damage build-up can evolve in Ag:SiC samples and estimate the order of magnitude of Ag fluence where SiC amorphization is expected. Taking into account these results, it is clear that the fluence of 1×10^{14} Ag^+ cm^{-2}

used for one of the samples is high enough to expect, at least, partial amorphization of the SiC structure. Indeed, comparing the experimental patterns of Fig. 3.10(a)-(b) with Fig. 3.11(a)-(b), the ones with higher implanted fluence [Fig. 3.11(a)-(b)] are considerably weaker and show broader structures, which corresponds to a heavily damaged lattice where the axial and planar directions are not well defined any more. The channeling effect still occurs but the anisotropy is lower when compared with the sample implanted with lower Ag fluence, which results in a lower maximum yield value.

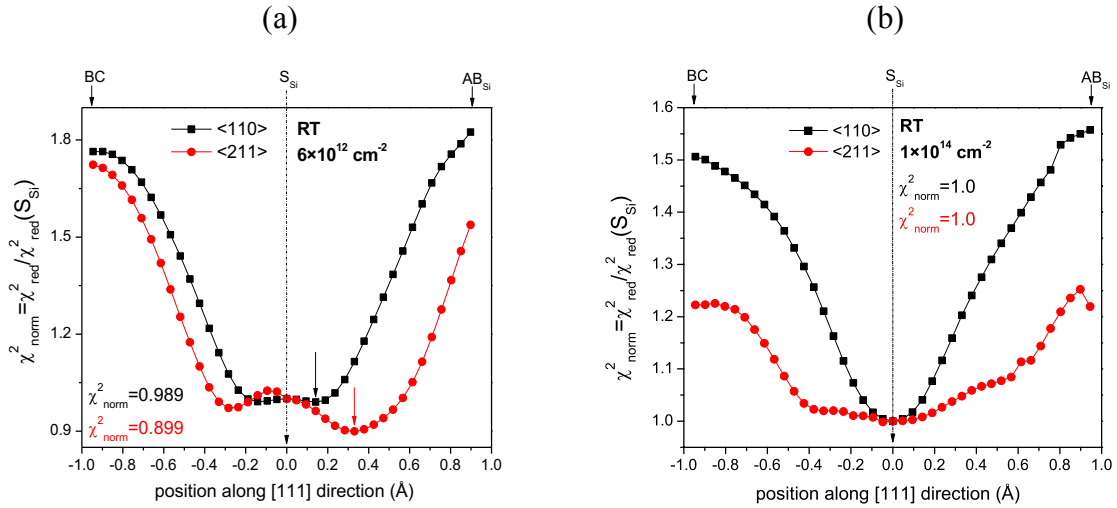

Figure 3.12. Normalized χ^2_{norm} of ^{111}Ag:3C-SiC (a) with 6×10^{12} cm^{-2} and (b) with 1×10^{14} cm^{-2} one-site fits to <110> and <211> patterns as a function of displacement from ideal S_{Si} after RT implantation. The χ^2_{norm} was in all cases normalized to that for the ideal S_{Si} site. The full arrows indicate the displacement positions where the lowest χ^2_{norm} was obtained.

A severely damaged lattice is thus the most likely explanation for the observed discrepancy among the results for the two samples in the displacement study from Si sites at RT, plotted in Fig. 3.12, while for the sample implanted with lowest fluence (6×10^{12} cm^{-2}) the best one-site fit is obtained for displacements of 0.2–0.3 Å from the ideal Si site. In the case of the higher fluence sample (1×10^{14} cm^{-2}) the results point towards no displacement at all. The fitting program is unable to provide a better fit using displaced positions due to the badly defined and broadened experimental patterns [Fig. 3.11(a)-(d), cf also Fig. 3.15(a)-(d)].

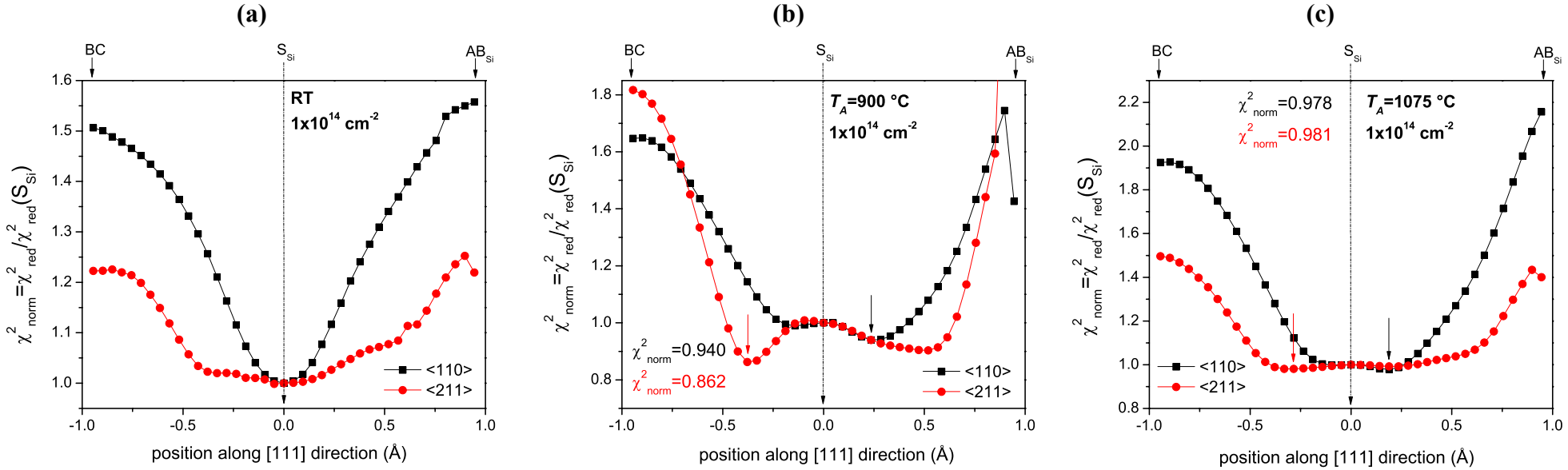

Figure 3.13. Normalized χ^2_{norm} of ^{111}Ag:3C-SiC (1×10^{14} cm^{-2}) one-site fits to <110> and <211> patterns as a function of displacement from ideal S_{Si} after RT implantation (a), after 900 °C annealing (b) and after 1075 °C annealing (c). The ^{111}Ag site was moved in small steps along the <111> direction from S_{Si} towards AB_{Si} and BC. The χ^2_{norm} was in all cases normalized to that for the ideal S_{Si} site. The full arrows indicate the displacement positions where the lowest χ^2 was obtained.

This explanation is supported with the observation of the χ^2_{norm} plot in Fig. 3.13(b), where the best fit is obtained, after annealing at 900 °C, for a displaced Si site (~0.3-0.4 Å). It is not expected that impurities located at stable positions, from an energetic point of view, such as substitutional Si site, move to a less stable interstitial position with successive annealing steps. A more appropriate explanation is the recovery of the lattice crystallinity, which in turn, corresponds to experimental patterns with higher anisotropy, clearly visible in Fig. 3.15(i)-(l).

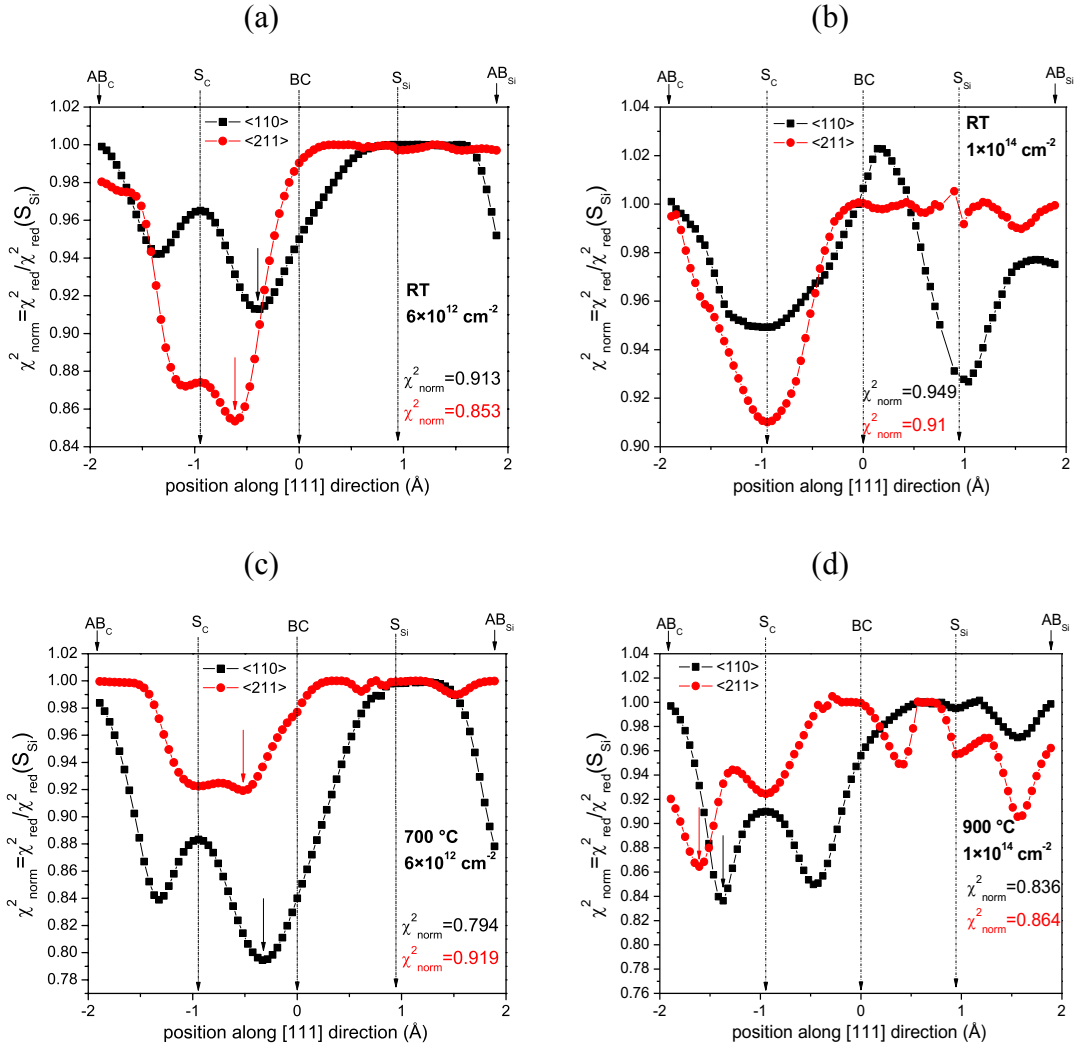

Figure 3.14. Normalized χ^2_{norm} of ^{111}Ag:3C-SiC (both fluences, 6×10^{12} cm^{-2} and 1×10^{14} cm^{-2}) two-site fits of <110> and <211> patterns as a function of displacement along [111] direction after RT implantation (a) and (b), after 700 °C (lowest implanted fluence sample) (c) and after 900 °C (highest implanted fluence sample) annealing (d). The first ^{111}Ag site was kept fixed on the S_{Si} position (displaced or not) from which resulted the best one-site fit. The position of the second site was moved in small steps along the <111> direction. The χ^2_{norm} was in all cases normalized to that for the one-site fit. The full arrows indicate the displacement positions where the lowest χ^2_{norm} was obtained.

Note that, while Figure 3.13 shows only the displacements towards AB_{Si} and BC for the highest fluence Ag:3C-SiC implanted sample, the χ^2_{norm} obtained from one-site fits to the <110> and <211> patterns as a function of displacement from Si site towards BC, AB_{Si}, DS_{Si} and SP_{Si}

sites were also tested. The displacement study for the remaining positions as well as for the other Ag:3C-SiC sample can be found in appendix B. The visual discrepancies observed in the lower fluence Ag:3C-SiC sample are also detected in the best fits of Fig. 3.11(g)-(h) after 900 °C and (k)-(l) after 1075 °C. To tackle this, the next step in the analysis was to allow the fitting routine to include a combination of two lattice sites. By fixing the first position on the Si position (displaced or not) obtained from the corresponding best one-site fit, the position of the second site was moved in small steps along the <111> direction. Fig. 3.14(a, c) shows the results for RT and after 700 °C annealing, for the lowest implanted fluence sample, and Fig. 3.14(b, d) for RT and after 900 °C annealing, for the highest fluence sample. In all plots of Fig. 3.14 χ^2_{norm} was normalized to that obtained from the corresponding one-site best fit. The best fits show that the second site is displaced from S_C towards BC (for the 6×10^{12} cm^{-2} sample case) or towards AB_C (for the 1×10^{14} cm^{-2} sample case). Due to these ambiguous results, a more in depth study was made, exploring also displacements from S_C along [100] towards SP_C and along [110] towards DS_C and can be found in appendix B. The combination (near S_{Si}+displaced S_C) towards BC gave slightly better fits, although the combinations (near S_{Si}+displaced S_C) towards AB_C, SP_C or DS_C produced also fits of similar quality. It was also found that the Ag probes sit at a displaced position of ~0.5–0.7 Å from ideal S_C with a 10%-20% improvement in the χ^2_{norm} compared to the single fraction fit. However, due to similar χ^2_{norm} values for the displacements towards BC, AB_C, SP_C or DS_C sites, no preferential displacement from S_C can be clearly pinpointed. Concerning the highest implanted fluence sample due to the high lattice damage, the best fits were obtained with a combination of ideal S_{Si} and ideal S_C sites until annealing up to 700 °C. Only after annealing at 800 °C, the best fits obtained present similar results to the ones corresponding to the sample with lowest implanted fluence.

The lattice recovery in both Ag:3C-SiC samples with the consecutive annealing is clearly visible by the improvement of the best-fit patterns anisotropy (Fig. 3.15 and 3.16).

Shrader *et al*. [Shrader2011] predicted the most stable configuration for Ag impurities in 3C-SiC to be formed when a Ag atom on a substitutional Si site is paired with a next neighbour C vacancy, i.e. forming the complex Ag_{Si}-V_C. Letting the defect configuration relax they calculated that the Ag displacement from the ideal Si position towards the C vacancy should be 37% of the Si–C bond length of 1.89 Å, which corresponds to ~0.70 Å. This means one should expect to find a Ag atom displaced of 0.70 Å from ideal Si site towards BC site. The results from this work do not confirm this prediction. As stated above, the Ag probe is found

near substitutional Si site, which is displaced of 0.2–0.3 Å towards AB_{Si} site [Fig. 3.12(a)], and in the vicinity of S_C site, which is displaced of 0.5-0.7 Å towards BC site [Fig. 3.14(a) and (c)], both far from the predicted value.

Finally, a fraction analysis, as a function of annealing temperature, was made by confining the fits to two lattice positions: displaced S_{Si} and S_C sites, obtained from the previous analysis, plotted and discussed in section 3.3.3.

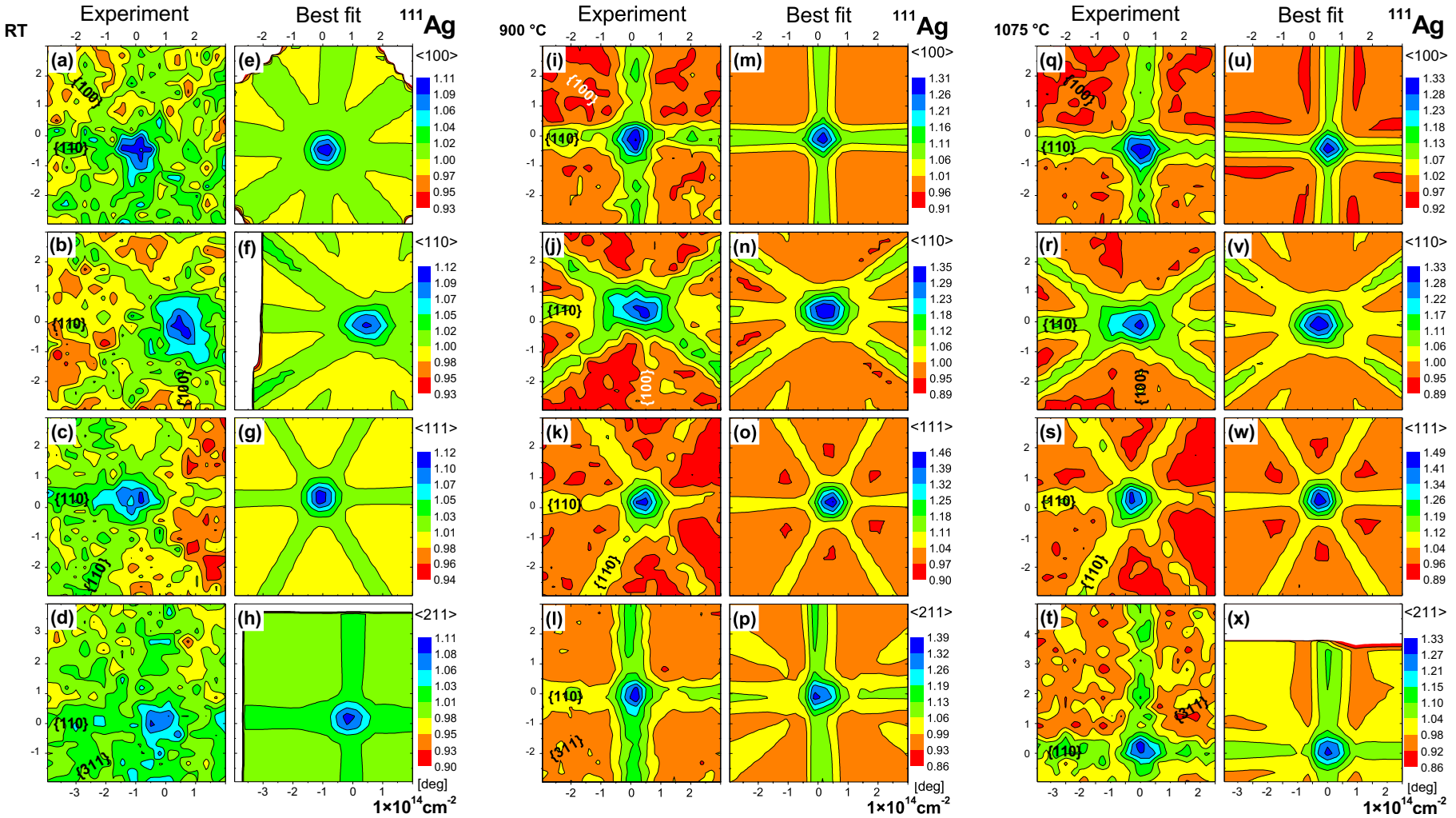

Figure 3.15. Normalized ^{111}Ag:3C-SiC (highest fluence, 1×10^{14} cm^{-2}), experimental β^- emission channeling patterns and corresponding best two-site fits for a combination of displaced S_{Si} and S_C sites, in the vicinity of <100>, <110>, <111> and <211> directions following implantation at room temperature (a)-(h), after annealing at 900 °C (i)-(p) and after annealing at 1075 °C (q)-(x).

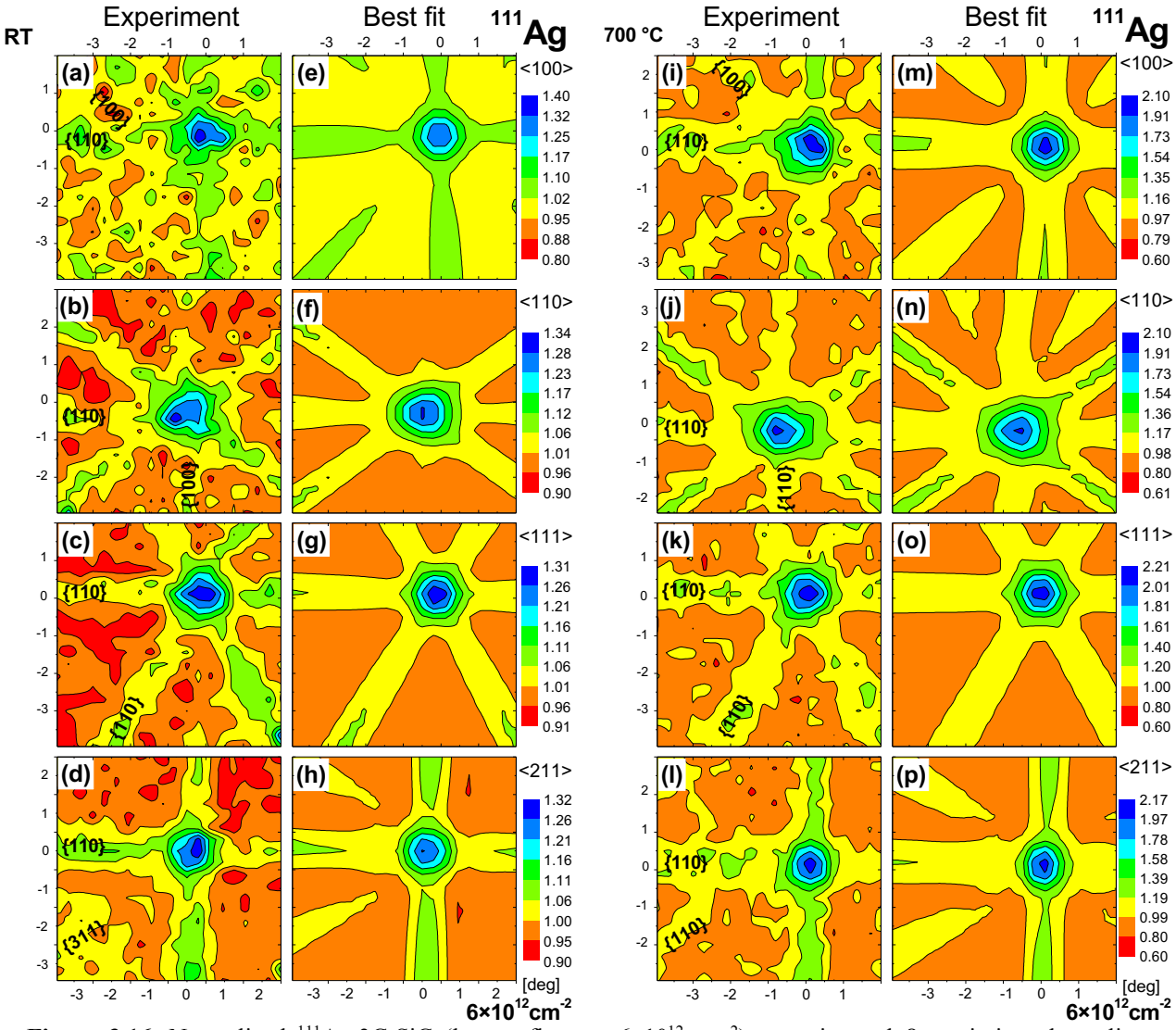

Figure 3.16. Normalized ^{111}Ag:3C-SiC (lowest fluence, 6×10^{12} cm^{-2}), experimental β^- emission channeling patterns and corresponding best fits for a combination of displaced S_{Si} and S_C sites, in the vicinity of <100>, <110>, <111> and <211> directions following implantation at room temperature (a)-(h) and after annealing at 700 °C (i)-(p).

3.3.2. 6H-SiC: ^{111}Ag fitting process

Quantitative information is obtained from experimental angular-dependent β^- emission patterns for all crystallographic directions, by fitting the experimental emission yields with theoretical patterns for the various possible lattice sites, calculated using the *manybeam* formalism for electron channeling. Fig. 3.17 displays [1̲101] and [2̲201] ^{111}Ag:6H-SiC patterns following Ag implantations (both for lower and higher fluences), at RT. Direct comparison of Fig. 3.17 to the theoretical patterns in Fig. 2.9(b) shows that, contrary to the observation for the other TMs, there is no indication for the existence of T_C sites in the RT as-implanted experimental results. In fact, these experimental patterns, visually, point to the occupation of substitutional sites, similar to the ones observed in ^{111}Ag:3C-SiC. As a first step, single fractions on regular sites were tested. It was concluded that the best one-site fits, for both Ag fluences, were obtained with the probes located at ideal substitutional Si sites for all annealing temperatures up to 900 °C.

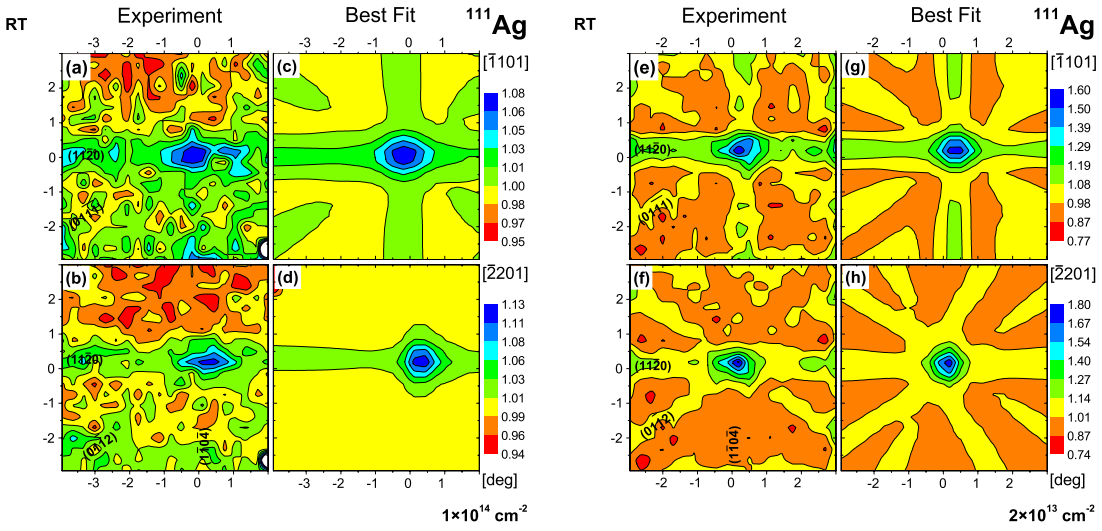

Figure 3.17. Normalized experimental β^- emission channeling patterns from highest (1×10^{14} cm^{-2}) (a)-(b) and lowest (2×10^{13} cm^{-2}) (e)-(f) implanted ^{111}Ag fluence, and corresponding best one-site fits using ideal $S_{Si,h+k}$ sites in the vicinity of [1̲101] and [2̲201] directions after RT implantation into 6H-SiC.

For annealing temperatures above 900 °C, single fraction fits fail to describe the experimental data well, an indication that a second site is at play. This result is visible in Fig. 3.18, where the best fits for T_A = 1075 °C are plotted. For both Ag fluences, in [1̲101] and [2̲201] directions, the fitting routine overestimated the fraction located at ideal S_{Si} sites, which is manifested by the central strong axial peak (dark blue colour), that is not present to the same extent in the corresponding experimental patterns. In particular the [2̲201] patterns illustrate that the relative intensity of axial [2̲201] and planar (11̲20) channeling effects calculated for S_{Si} sites does not

match well the experimental data. The next step was to allow the fitting routine to include simultaneously two ideal lattice sites. For both Ag fluences, the combination of $S_{Si,h+k}$+BC(c+a) gave the best fit and improved the χ^2_{norm} compared to the single fraction fit by ~10%-20%. Note that in the 6H structure the BC(c+a) sites provided better fits as second fraction than the C substitutional. BC(c+a) sites are the statistical combination of all possible bond-centered sites in the 6H crystal, i.e. those that are located along the c-axis (statistical weight 1/4), as well as those that are basal to it (statistical weight 3/4). The best fits with this 2-site combination, are plotted in Fig. 3.19 (for RT results), and Fig. 3.20 (after the 1075 °C annealing). Once more, no indications were found that the Ag substitutional Si site preference deviates from the statistical mixture of 1/3 (*h*) hexagonal and 2/3 (*k*) cubic-like sites in the 6H crystal.

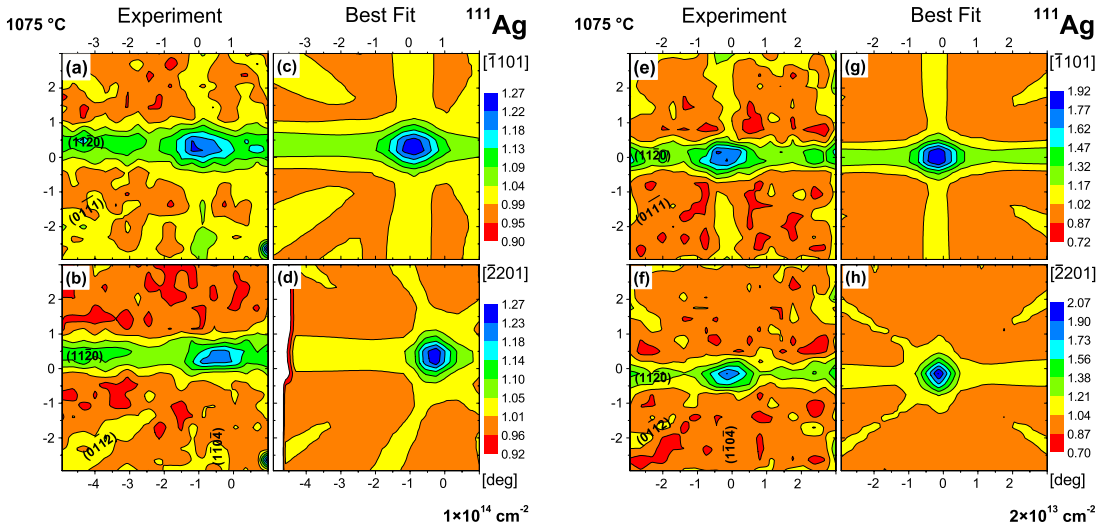

Figure 3.18. Normalized experimental β^- emission channeling patterns from highest (1×10^{14} cm^{-2}) (a)-(b) and lowest (2×10^{13} cm^{-2}) (e)-(f) implanted ^{111}Ag fluence in 6H-SiC, and corresponding best one-site fits using ideal $S_{Si,h+k}$ sites in the vicinity of [1101] and [2201] directions after annealing at 1075 °C.

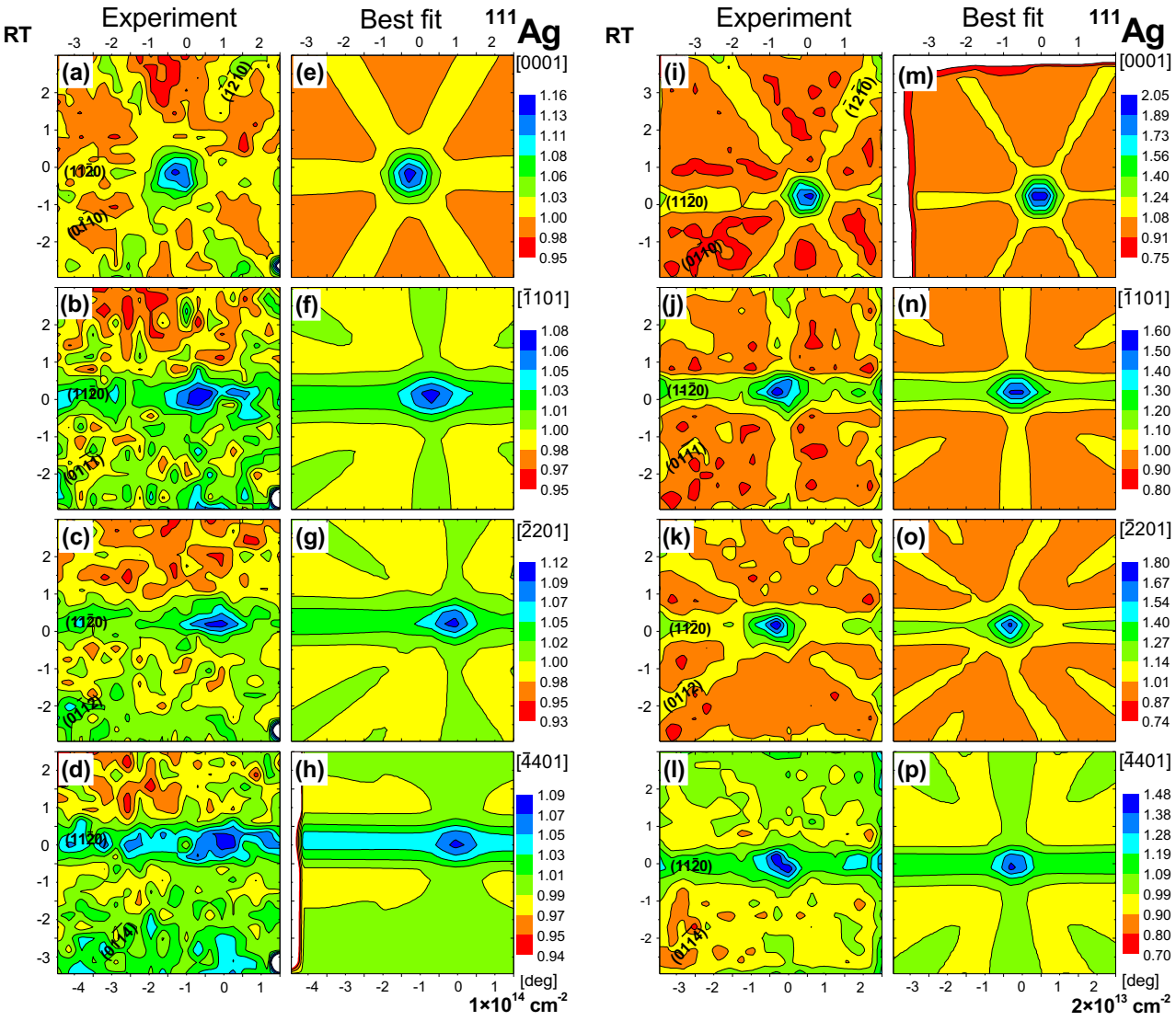

Figure 3.19. Normalized experimental β^- emission channeling patterns and corresponding best two-site fits for a combination of ideal $S_{Si,h+k}$ and BC(c+a) sites, in the vicinity of [0001], [$\underline{1}$101], [$\underline{2}$201] and [$\underline{4}$401] directions following highest fluence (1×10^{14} cm^{-2}) (a)-(h), and lowest fluence (2×10^{13} cm^{-2}) (i)-(p), ^{111}Ag implantation into 6H-SiC at RT.

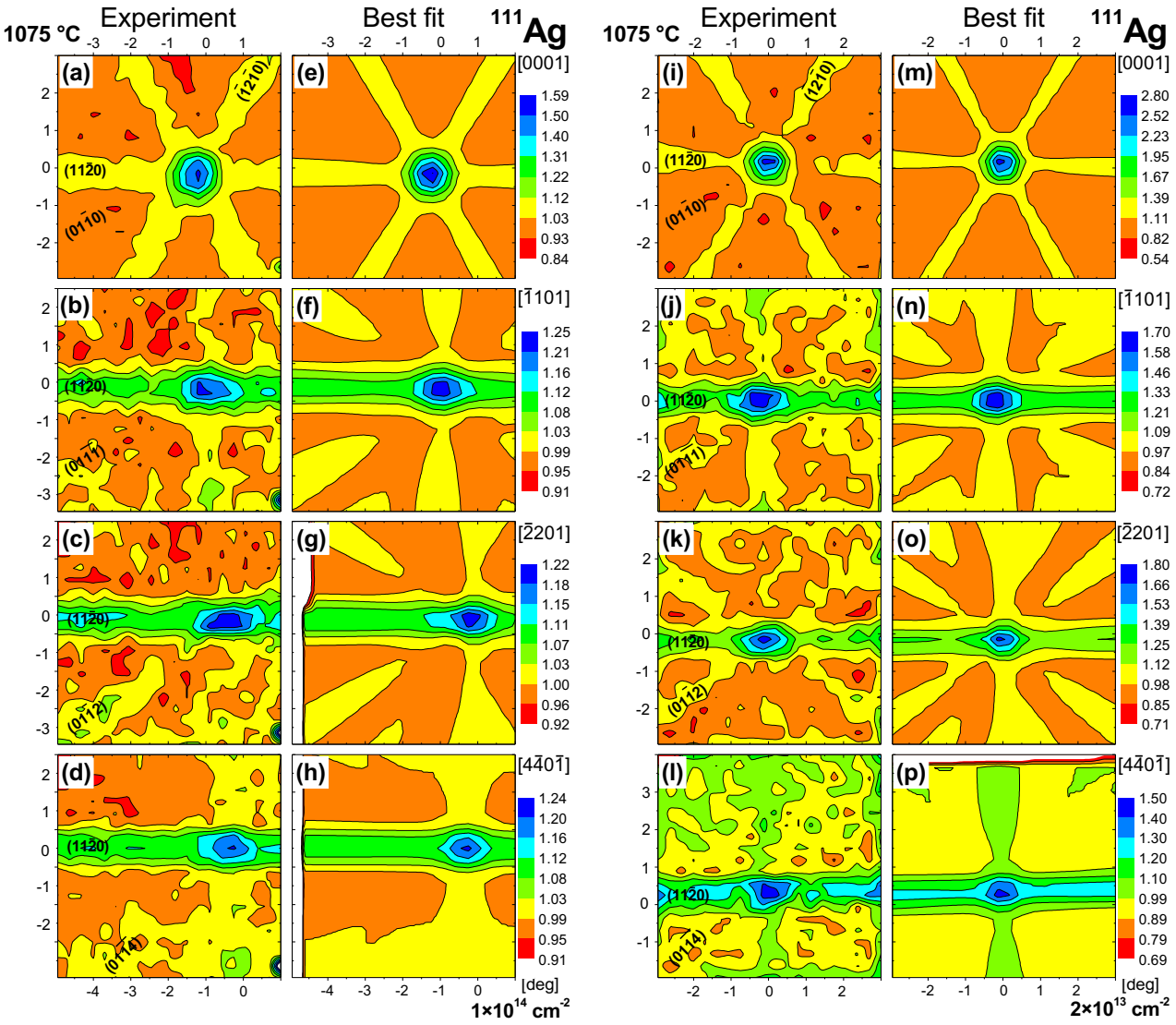

Figure 3.20. Normalized experimental β^- emission channeling patterns and corresponding best two-site fits for a combination of ideal $S_{Si,h+k}$ and BC(c+a) sites, in the vicinity of [0001], [$\underline{1}$101], [$\underline{2}$201] and [$\underline{4}$401] directions following highest fluence (1×10^{14} cm^{-2}) (a)-(h), and lowest fluence (2×10^{13} cm^{-2}) (i)-(p), ^{111}Ag implantation into 6H-SiC and annealing at 1075 °C.

3.3.3. Discussion

Figure 3.21 shows the Ag fitted fractions for the two considered sites, substitutional Si and BC in 6H, and substitutional Si and sites in between substitutional C and BC in 3C, as well as 'random' sites that give isotropic emission distribution as a function of annealing temperature. Two samples of each polytype were implanted, one with fluence of 6×10^{12}-2×10^{13} Ag^{+} cm^{-2} and the other with 1×10^{14} Ag^{+} cm^{-2}.

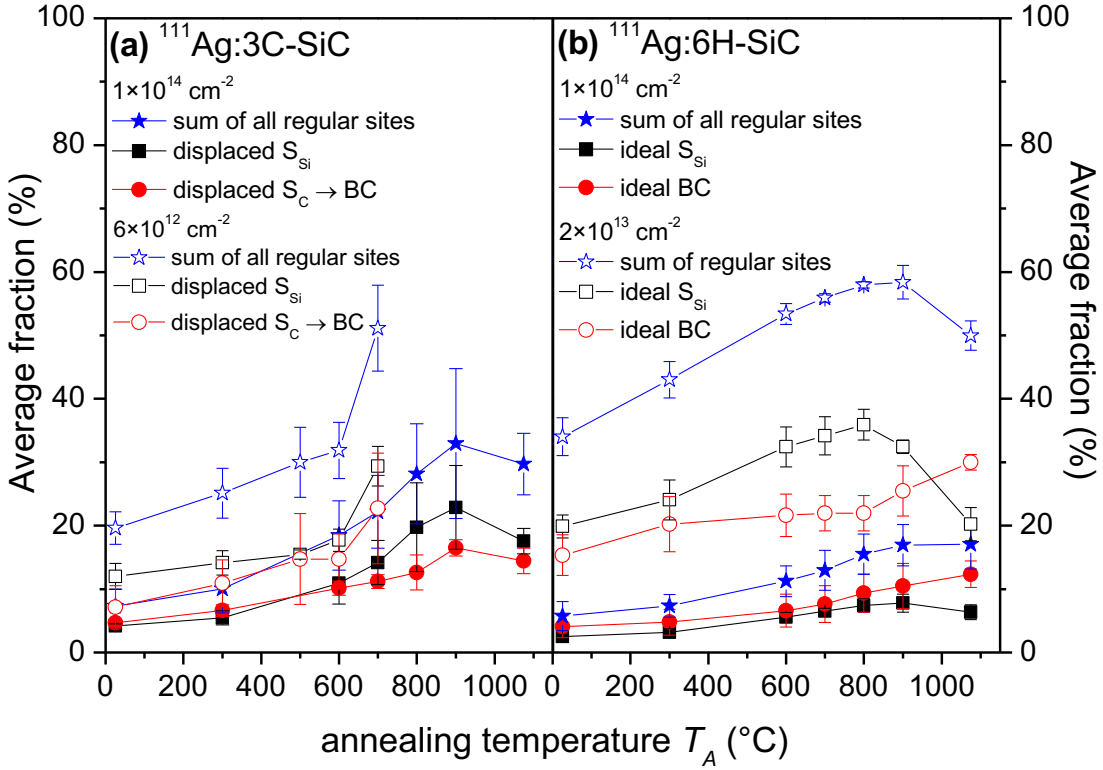

Figure 3.21. Fitted fractions of implanted ^{111}Ag in (a) 3C-SiC: emitter atoms on near substitutional Si (in black) and displaced S_C sites (in red) plus the sum of both site fractions (in blue) as a function of the annealing temperature, averaged for the four measured crystallographic directions; and (b) 6H-SiC: emitter atoms located on ideal Si and ideal BC sites. The error bars represent the spread in fitted fractions for the different crystallographic directions.

Note that one of the 3C samples was implanted in an initial Ag run with the particularly low fluence 6×10^{12} cm^{-2} and hence could be only measured and annealed up to 700 °C, with the intention to test the viability of experiments with the ^{111}Ag:SiC system. The other three samples were implanted in a subsequent Ag run and each subjected to the same experimental and annealing conditions. Note also that the behaviour of the fitted Ag fractions, as function of annealing temperature, is similar for samples with the same implanted probe fluence

irrespective of the SiC polytype used. Due to this fact, most of the discussion and subsequent conclusions will address both polytypes without distinction between them.

Nevertheless, care has to be taken because, for the 6H- samples, only ideal site simulations are available for the experimental data analysis, whereas for the 3C-SiC samples, it was also possible to take displacements from the ideal sites into account.

For the lowest Ag implanted fluence, the fraction located at substitutional Si sites dominates the patterns in the as-implanted state with 12% on near S_{Si} site (3C), and 20% on ideal S_{Si} site (6H), in contrast to only 7% and 17% on near BC and ideal BC respectively. For the 1×10^{14} Ag^{+} cm^{-2} implanted samples, the fitted probe fractions in both regular sites are similar, albeit very low: 4% and 5% for near S_{Si} and near BC sites (3C), and 4% and 3% for ideal S_{Si} and ideal BC sites (6H).

The fitted Ag fractions at ideal S_{Si} sites reach their maxima upon annealing at 800 °C-900 °C for all samples where this temperature was investigated, although the detailed behaviour differs. In 6H samples, one has, for the lowest Ag implanted samples, 36% of the probes located at ideal S_{Si} sites and for the one implanted with the highest fluence, only 7%. Then, in the 6H with lowest Ag fluence after the last annealing at 1075 °C, the probe fraction located at substitutional Si sites decreases. While some of this decrease is matched by an increase in the BC fraction, the sum fraction decreases even stronger, which means that most of the Ag probes that have disappeared from substitutional Si sites moved to 'random' positions, e.g. by clustering into Ag metal precipitates. In the high-fluence 6H sample, where overall fractions were quite low, the BC fraction was always dominating and became even more so after the 1075 °C annealing step. The 3C sample implanted with highest fluence did not show the partial conversion of Si substitutional Ag to sites in the neighbourhood of BC, but rather both fractions decreased simultaneously after the final 1075 °C annealing. Note that in all samples the sum of the two fitted probe fractions stay well below 100% throughout the measurements with the remaining fraction located at 'random' sites. The following aspects contribute in providing a possible explanation for this behaviour.

First, based on *ab initio* methods using density functional theory, Shrader *et al*. [Shrader2011] determined the structures and charge states of intrinsic and Ag-related defects in cubic 3C-SiC as well as the mechanisms of Ag diffusion. It was suggested that the most stable configuration for this impurity in SiC is within a defect cluster consisting of Ag located in a substitutional Si site coupled with a C vacancy with a charge state of −1, $(Ag_{Si}\text{-}V_C)^{-1}$.

Second, while according to the calculations of the same author the formation energy of interstitial Ag_{TC} with respect to a reservoir of metallic Ag is very high, ~10.5 eV, one has to take into account that ion implantation is a process that happens in non-equilibrium conditions and thus the formation energies of defects can easily be provided by the kinetic energy of the implanted ion. It thus cannot be ruled out that this defect is created. Nevertheless, contrary to what was observed for the 3*d* TMs studied here, no indication for the existence of tetrahedral carbon coordinated interstitial Ag (noted as Ag_{TC}) was found in any of the samples.

On the other hand, interstitial Ag_{TC} is predicted in Ref. [Shrader2011] to have a rather low migration energy, 0.89 eV, when compared with migration energies of 5.2 eV-6.5 eV and 3.5 eV-5.2 eV [Bockstedte2002] for the Si and C vacancies, respectively, or with the transformation of V_{Si}^{-} into a carbon vacancy-antisite complex with an energy barrier of 2.2 eV-2.5 eV [Itoh1989, Bockstedte2004], which suggests that there are vacancies available to capture the diffusing Ag interstitials. This author also calculated the pre-exponential factor D_0 for the interstitial migration, $D_0=9.57\times10^{-8}$ m^2s^{-1}, so it is possible to estimate the mean diffusion width $(6Dt)^{½}$ during the RT Ag implantation. If one takes the lowest fluence Ag implanted samples, which took ~10 min to be implanted, and expresses the diffusion coefficient D as $D=9.57\times10^{-8}$ m^2s^{-1} $\exp(-0.89\text{eV}/k_BT)$, one estimates a mean diffusion width of ~4 Å during implantation. Given the fact that the samples were in addition stored for several hours before the measurements started, there is ample time for interstitial Ag to migrate tens of Å and pair with vacancy-like defects resulting from implantation.

Third, there are effects expected from implantation damage and its annealing. As already discussed in the previous section, electrons emitted by the probe atoms located in damaged regions or, if travelling through those regions with increased de-channeling probability, are contributing to the isotropic background. While annealing temperatures as high as 1400 °C are needed to obtain a complete SiC lattice recovery, partial lattice recovery is possible at lower temperatures if the fluence of implanted heavy ions implanted is below 10^{15} cm^{-2}. So, the overall observed fraction increase up to 900 °C in all Ag:SiC samples is, as was already stated for the other TM probes in the previous section, most likely a result of the local recovery of the host lattice.

Several experimental and theoretical studies regarding the diffusion mechanism of Ag in most common single crystal polytypes such as 4H- and 6H-SiC, as well as in polycrystalline SiC, commonly known as β-SiC, are documented in the literature [Maclean2006, Friedland2009, Khalil2011, Shrader2011, Gerczak2015]. These studies were motivated by the use of SiC as a

barrier material that is intended to stop the accidental release of radionuclides from advanced nuclear reactor fuels, where the long-lived radioisotope ^{110m}Ag (253 d) is one of the prominent fission products. Typical Ag ion implantation fluences used in these studies were from 10^{14} cm^{-2} to 10^{17} cm^{-2}, with implantation energies that ranged from several hundred keV to several MeV and annealing temperatures up to 1600 °C. The disparity of the experimental results described by the different authors, which is reflected in the wide range of four orders of magnitude difference for the derived Ag diffusion coefficient, highlights the difficulty to establish the Ag transport mechanism inside SiC. Friedland *et al*. [Friedland2009] found using Rutherford Backscattering Spectrometry (RBS) channeling and electron microscopy techniques and annealing for 10 h at 1300 °C that Ag diffusion was observed in both polycrystalline SiC and 6H-SiC single crystal samples. The diffusion process was associated mainly to implant induced radiation damage. After further annealing at this temperature no additional diffusion took place in the 6H-SiC samples, while it was considerably reduced in the polycrystalline SiC. The later was associated by the authors to grain boundary diffusion mechanism. Gerczak *et al*. [Gerczak2015] found using transmission electron microscopy (TEM), scanning transmission electron microscopy (STEM) and secondary-ion mass spectrometry (SIMS) techniques and annealing for several hours in the temperature range of 1500 °C-1625 °C that Ag diffuses in both polycrystalline SiC and 4H-SiC samples. The author suggested two different mechanisms for the Ag diffusion depending on the SiC type studied: for 4H-SiC, Ag diffusion was due to a kick-out mechanism with Si self-insterstitials produced by the implantation process, whereas for the polycrystalline SiC, the Ag diffusion happened by the grain boundary process. Leng *et al*. [Leng2016] investigated the Ag diffusion in polycrystalline 3C-SiC as well as in single crystal 4H-SiC samples before and after irradiation with C^{2+} ions. The samples were annealed at temperatures that ranged from 1500 °C and 1600 °C up to 20 h. The subsequent diffusion profiles were analysed by SIMS and it was observed that, for the 3C-SiC polycrystalline material, the damage introduced by C^{2+} irradiation significantly enhanced the Ag diffusion coefficient as compared to the unirradiated samples due to a combined effect of radiation damage on diffusion and the presence of grain boundaries. On the other hand, neither 4H-SiC samples nor unirradiated and C^{2+} irradiated single crystals showed visible Ag diffusion.

In contrast with these results, Maclean *et al*. [Maclean2006], using SEM, analytical electron microscopy (AEM) and energy dispersive X-ray spectroscopy (EDS) and annealing at 1500 °C up to 480 hours, did not find, within the accuracy of their measurements, any evidence of Ag diffusion neither in the bulk nor along grain boundaries in their polycrystalline SiC samples. However, the author did not outright reject the possibility of the diffusion process happening,

instead presented the value of 5×10^{-19} cm^2s^{-1} as upper limit for the Ag diffusion coefficient corresponding to concentrations below the minimum sensitivity of his analysis. Although Maclean *et al*. [Maclean2006] did not observe any Ag diffusion, their upper limit for the diffusion coefficient comes close to the interval of values given by the other authors, either from experimental results or from theory, which ranged from 10^{-14} cm^2s^{-1} to 10^{-17} cm^2s^{-1}.

The important thing to retain from these results is the considerable stability of implanted Ag inside SiC, where annealing temperatures above 1300 °C were needed to observe Ag diffusion processes on a μm depth scale. In the following, the hypothesis will be investigated that the decrease in the substitutional Ag fraction following annealing at 1075 °C is due to the onset of substitutional Ag diffusion by the so-called Frank-Turnbull process (suggested in 1956 by Frank and Turnbull for the diffusion of Cu in Ge [Frank1956]) on a depth scale of order of magnitude 100 nm.

If it is assumed that the decrease in Ag fractions on S_{Si} sites is caused by the onset of Ag diffusion starting from substitutional sites, it is possible to estimate the activation energy E_A for this diffusion process by using a similar Arrhenius model, as was already described in the previous section. Note that in this simple model E_A is to be interpreted as the energy barrier $E_A = E_B + E_M$, i.e. the sum of the binding energy E_B of Ag to a substitutional Si site plus the migration energy E_M of interstitial Ag.

Table 3.3. Estimates for the Ag on near S_{Si} sites activation energy for diffusion E_A considering two different scenarios for the number of jumps: N=1 and $N=N_{max}$. For the last scenario, the value of N_{max} is estimated using the assumptions described in the text.

	6H-SiC			3C-SiC		
N_{max}	Ag fluence [cm^{-2}]	$E_A(N=1)$ [eV]	$E_A(N=N_{max})$ [eV]	Ag fluence [cm^{-2}]	$E_A(N=1)$ [eV]	$E_A(N=N_{max})$ [eV]
≈1020	2×10^{13}	4.0	3.2	-	-	-
≈5100	1×10^{14}	4.1	3.1	1×10^{14}	4.1	3.1

Two scenarios are considered for the calculation of N: (1) an upper limit estimate for the migration energy is obtained if a simple one-step jump and neglecting possible effects of retrapping is enough for the dissociation of the near substitutional Ag defect; (2) the fact that long-range diffusion of Ag, located on near S_{Si} sites, does not take place within a narrow temperature regime (in the literature, is a process that occurs in the temperature range of 1000 °C-1600 °C), indicates that there are effects from retrapping. The number of times a diffusing atom is captured by a trap before it escapes either to the bulk of the sample or towards the surface, starting from the center of a trap profile with a sheet density ϕ, is of order of

magnitude $3\pi R^2\phi$, where R is the capture radius. Assuming $R = 10$ Å and $\phi =$ (Ag atoms/cm^2) × (number of vacancies/implanted Ag), one estimates ≈5100 trapping events per Ag atom for the highest fluence implanted samples and ≈1020 for the lowest fluence implanted samples. The results are shown in table 3.3. Concerning the estimated activation energies for Ag diffusion E_A the following comments are appropriate: tentatively one might think that before the 1075-°C annealing step still a considerable amount of Si vacancies V_{Si} is contained in the SiC samples, in which case multiple retrapping should occur and the estimate E_A~3.1 eV-3.2 eV would yield the better estimate. However, if the V_{Si} should all have transformed to V_C-Si_C complexes, as was outlined in sections 1.6 and 3.2.1, these should not be able to trap interstitial Ag any more on S_{Si} sites, in which case the one-step model with E_A~4.0 eV-4.1 eV would be the more suitable approach.

A completely different scenario for Ag diffusion was outlined by Leng *et al*. [Leng2016] and should hence also be considered. They assumed that the diffusion of substitutional Ag does not follow the Frank-Turnbull model in which a substitutional foreign atom is spontaneously ejected as an interstitial, but rather the so-called kick-out mechanism, by which the ejection is caused by a native Si interstitial migrating through the lattice which "kicks out" the substitutional foreign atom and thus is able to take its place. In both cases the resulting Ag interstitial would then migrate fast through the lattice until it is captured by another trap, which in the *N*-step model is assumed to be also a Si vacancy. The kick-out process can hence, too, be approximated by 1 or *N*-step scenarios and the estimates for E_A(Ag) given in Table 3 would also apply, however, the interpretation of E_A would be different. In the kick-out picture, E_A would be to large extent simply the migration energy of the Si interstitial since the kickout of a Ag_{Si} by a neigbouring Si interstitial is probably not inhibited by a barrier. Leng *et al.* have calculated an activation barrier of E_A=3.35 eV for the reaction $Ag_{Si}+Si_i \rightarrow Ag_i(T_C)$ which in fact fits quite well with the energy range E_A=3.1 eV-4.1 eV estimated in this work. On the other hand, since Leng *et al.* did not calculate the activation barrier for simple Frank-Turnbull dissociation $Ag_{Si} \rightarrow Ag_i(T_C)+V_{Si}$, such a comparison value from theory is missing. As a matter of fact, from the phenomenological perspective of emission channeling experiments one cannot distinguish whether the instability of Ag on the substitutional Si sites is caused by substitutional Ag being released in a Frank-Turnbull process or being kicked out by a Si interstitial. Self-interstitials and vacancies are both a product of the ion implantation process and, although it is to be expected that they disappear gradually with the annealing procedure when forming

Frenkel pairs, it is reasonable to assume that some will have survived and still exist when annealing at 1075 °C.

Finally, a comparison with previous lattice location results of the same ^{111}Ag probe in Si single crystals [Wahl2002] will also be made. After RT implantation, the analysis of the Si results showed that the majority of Ag probes were located at near S_{Si} sites (~0.3 Å-0.4 Å from substitutional Si sites), similar to the ones observed in this work.

Similar near substitutional sites were in later works on the lattice location of Fe, Ni, Mn and Co in Si [Silva2013, Silva2014a, Silva2014b, Silva2016, Silva2017] interpreted as TMs inside multivacancy complexes such as divacancies or hexavacancies. In this thesis, evidence was presented that Ag in SiC is found on two types of lattice sites: one that is relatively close to the ideal Si site, and a second one that is located in the vicinity of the S_C and BC site, although EC analysis is unable to clearly identify its exact location. A likely explanation is that one represents Ag inside a single Si vacancy, the other inside a mixed Si-C divacancy, although in the latter case the EC results do not confirm the same structure as predicted in the literature [Shrader2011] for the resulting (Ag_{Si}-V_C) complex.

Regarding the annealing behaviour of Ag in Si, with progressive thermal treatments, a maximum Ag fraction on near S_{Si} sites of around 60-80% after annealing at 200 °C-300 °C was achieved in Si, a striking difference when compared with Ag:SiC results, where the Ag fraction maximum was achieved only upon 900 °C annealing. Upon annealing above 300 °C, the near substitutional Ag fraction in Si decreased continuously until reaching values close to detection limit after annealing at 600 °C, at which point the authors considered that Ag had partially out-diffused to the crystal surface, a situation which was confirmed by the detection of radioactivity on the sample holder. Hence, whereas in Si overcoming a dissociation energy around 1.8 eV-2.2 eV was enough to activate the diffusion process of substitutional ^{111}Ag, its stability in SiC with activation energy around 3.1 eV-4.1 eV is considerably higher.

Fits using two sites were also made in the case of Si – near substitutional plus tetrahedral interstitial (T) – which resulted, except following annealing at 400 °C and 500 °C where T fractions had values around 20%, in small T fractions close to the detection limit. Although fits with two sites were tested in this work for ^{111}Ag in SiC, the resulting second site was always a displaced S_C or BC site. The T sites (T_C and T_{Si} sites) were also tested in all Ag:SiC samples, but their fraction results always negative.

3.3.4. Conclusions

The lattice location of the ^{111}Ag 4*d* transition metal probes in both 3C- and 6H-SiC polytypes was experimentally determined as a function of annealing temperature up to 1075 °C. Two samples of each polytype were implanted with different Ag fluences ranging from 6×10^{12} cm^{-2} to 10^{14} cm^{-2}. In all cases two types of lattice sites were identified: Ag on or relatively close to a substitutional Si site, and a second site where Ag would be located near the S_C or BC position in a perfect lattice. Tentatively these two types of sites are identified as Ag inside a single Si vacancy Ag_{Si} and the so-called Ag_{Si}-V_C complex, i.e. Ag inside a mixed Si and C di-vacancy. Regarding specifically the 6H-SiC polytype, no indications were found for a deviation of the Ag dopant distribution on the substitutional Si sites from the statistical mixture of 1/3 hexagonally (*h*) and 2/3 cubically (*k*) coordinated positions, a result which is similar to the one observed for the other TM probes ^{56}Mn, ^{59}Fe and ^{65}Ni. However, contrary to what was observed for the other 3*d* TMs, no interstitial Ag (Ag_{TC}) could be detected in any of the SiC samples, which is explained by the low migration energy of 0.89 eV, which allows interstitial Ag to migrate to traps already at RT. Irrespective of the SiC polytype used, the Ag fractions identified at the two types of lattice sites (displaced substitutional Si and S_C or BC) presented similar behaviour as function of annealing temperature. Although qualitatively the same lattice sites were identified, the samples implanted with the highest ^{111}Ag fluences showed considerably higher random fractions, which is most likely attributed to partial amorphization of the implantation zone. Nevertheless, lattice recovery is still possible by the use of thermal treatments, as observed in Fig. 3.21. The activation energy for Ag leaving the substitutional Si site E_A was estimated as 3.1 eV-4.1 eV. While these values are comparable to the 3.35 eV theoretically predicted by Leng *et al*. for kick-out of substitutional Ag by Si self-interstitials [Leng2016] a comparison to the activation energy for simple dissociation of Ag from the Si site cannot be made since this process was not considered by Leng *et al*. By means of emission channeling, it is not possible to distinguish between substitutional Ag released by a kick-out or Frank-Turnbull process since the experimental outcomes would be very similar. The Ag probes occupying the vicinity of S_C or BC site were found to persist even at an annealing temperature of 1075 °C, showing that the corresponding defect complex is highly stable against annealing.

References

[Agostinelli2003] S. Agostinelli *et al*. "GEANT4 - A simulation toolkit", *Nucl. Instruments Methods Phys. Res.* A **506** 250–303 (2003).

[Bharuth2003] K. Bharuth-Ram, U. Wahl, J. G. Correia, "Lattice location of Fe in diamond", *Nucl. Instruments Methods Phys. Res.* B **206** 941–946 (2003).

[Bharuth2008] K. Bharuth-Ram, H. P. Gunnlaugsson, R. Mantovan, V. V. Naicker, D. Naidoo, R. Sielemann, G. Weyer, T. Agne, "Mössbauer study of Fe in 3C-SiC following ^{57}Mn implantation", *Hyperfine Interact.* **184** 207–211 (2008).

[Bockstedte2002] M. Bockstedte, M. Heid, A. Mattausch, O. Pankratov, "The nature and diffusion of intrinsic point defects in SiC", *Mater. Sci. Forum* **389–393** 471–476 (2002).

[Bockstedte2004] M. Bockstedte, A. Mattausch, O. Pankratov, "*Ab initio* study of the annealing of vacancies and interstitials in cubic SiC: Vacancy-interstitial recombination and aggregation of carbon interstitials", *Phys. Rev.* B **69** 235202(1–13) (2004).

[Danno2012] K. Danno, H. Saitoh, A. Seki, T. Shirai, H. Suzuki, T. Bessho, Y. Kawai, T. Kimoto, "Diffusion of transition metals in 4H-SiC and trials of impurity gettering" *Appl. Phys. Express* **5** 031301 (2012).

[Debelle2010] A. Debelle, L. Thomé, A. Boulle, F. Garrido, J. Jagielski, D. Chaussende, "Characterization and modelling of the ion-irradiation induced disorder in 6H-SiC and 3C-SiC single crystals", *J. Phys. D: Appl. Phys*. **43** 455408(1–7) (2010).

[Frank1956] F. C. Frank, D. Turnbull, "Mechanism of diffusion of copper in germanium", Phys. Rev. **104** 617-618 (1956).

[Friedland2009] E. Friedland, J. B. Malherbe, N. G. van der Berg, T. Hlatshwayo, A. J. Botha, E. Wendler, W. Wesch, "Study of silver diffusion in silicon carbide", *J. Nucl. Mater.* **389** 326–331 (2009).

[Gerczak2015] T. J. Gerczak, B. Leng, K. Sridharan, J. L. Hunter Jr., A. J. Giordani, T. R. Allen, "Observations of Ag diffusion in ion implanted SiC", *J. Nucl. Mater.* **461** 314-324 (2015).

[Gunnlaugsson2006] H. P. Gunnlaugsson, M. Dietrich, "Identification of substitutional and interstitial Fe in 6H-SiC", *Hyperfine Interact.* **169** 1319-1323 (2006).

[Hofsäss1991] H. Hofsäss, G. Lindner, "Emission channeling and blocking", *Phys. Rep.* **201** 121–183 (1991).

[Itoh1989] H. Itoh, N. Hayakawa, I. Nashiyama, E. Sakuma, "Electron spin resonance in electron irradiated 3C SiC", *J. Appl. Phys.* **66** 4529–4531 (1989).

[Itoh1997] H. Itoh, A. Kawasuso, T. Ohshima, M. Yoshikawa, I. Nashiyama, S. Tanigawa, S. Misawa, H. Okumura, S. Yoshida, "Intrinsic defects in cubic silicon carbide" *Phys. stat. sol* (a) **162** 173–198 (1997).

[Jiang1999] W. Jiang, W. J. Weber, S. Thevuthasan, D. E. McCready, "Displacement energy measurements for ion-irradiated 6H-SiC", *Nucl. Instruments Methods Phys. Res.* B **148** 557-561 (1999).

[Jiang2001] W. Jiang, W. Weber, S. Thevuthasan, "Ion implantation and thermal annealing in silicon carbide and gallium nitride", *Nucl. Instruments Methods Phys. Res.* B **178** 204-208 (2001).

[Jiang2009] W. Jiang, W. J. Weber, J. Lian, N. M. Kalkhoran, "Disorder accumulation and recovery in gold-ion irradiated 3C-SiC", *J. Appl. Phys*. **105** 013529(1–6) (2009).

[Jiang2010] W. Jiang, H. Wang, I. Kim, Y. Zhang, W. J. Weber, "Amorphization of nanocrystalline 3C-SiC irradiated with Si^+ ions", *J. Mater. Res.* **25** 2341–2348 (2010).

[Jonson2000] B. Jonson, A. Richter, "More than three decades of ISOLDE physics", *Hyperfine Interact.* **129** 1–22 (2000).

[Kawasuso1998] A. Kawasuso, H. Itoh, N. Morishita, M. Yoshikawa, T. Ohshima, I. Nashiyama, S. Okada, H. Okumura, S. Yoshida, "Silicon vacancies in 3C-SiC observed by positron lifetime and electron spin resonance", *Appl. Phys.* A **212** 209–212 (1998).

[Khalil2011] S. Khalil, N. Swaminathan, D. Shrader, A. J. Heim, D. Morgan, I. Szlufarska, "Diffusion of Ag along $\sum 3$ grain boundaries in 3C-SiC", *Phys. Rev*. B **84** 214104(1–13) (2011).

[Leng2016] B. Leng, H. Ko, T. J. Gerczak, J. Deng, A. J. Giordani, J. L. Hunter Jr., D. Morgan, I. Szlufarska, K. Sridharan, "Effect of carbon ion irradiation on Ag diffusion in SiC", *J. Nucl. Mater*. **471** 220–232 (2016).

[Machado2015] W. V. M. Machado, J. F. Justo, L. V. C. Assali, "Iron and manganese-related magnetic centers in hexagonal silicon carbide: A possible roadmap for spintronic devices", *J. Appl. Phys.* **118** 045704(1–6) (2015).

[Maclean2006] H. J. MacLean, R.G. Ballinger, L. E. Kolaya, S. A. Simonson, N. Lewis, M. E. Hanson, "The effect of annealing at 1500 °C on migration and release of ion implanted silver in CVD silicon carbide", *J. Nucl. Mater.* **357** 31–47 (2006).

[Medvedeva2003] N. I. Medvedeva, E. I. Yur'eva, A. L. Ivanovskii, "Electronic structure of cubic silicon carbide with substitutional 3d impurities at Si and C sites", *Semiconductors* **37** 1243–1246 (2003).

[Mehrer2007] H. Mehrer, "Diffusion of interstitial solutes in metals", *Diffusion in Solids,* M.

Cardona, P. Fulde, K. von Klitzing, R. Merlin, H. J. Queisser and H. Störmer (Eds.), Springer-Verlag, 2007, pp. 316–326.

[Miao2003] M. Miao, W. Lambrecht, "Magnetic properties of substitutional 3d transition metal impurities in silicon carbide", *Phys. Rev.* B **68** 125204(1–10) (2003).

[Miranda2012] P. Miranda, U. Wahl, N. Catarino, K. Lorenz, J.G. Correia, E. Alves, "Damage formation and recovery in Fe implanted 6H-SiC", Nuclear Instruments and Methods in Physics Research B **286** 89–92 (2012).

[Petrenko2001] T. T. Petrenko, T. L. Petrenko, V. Y. Bratus, J. L. Monge, "Calculation of hyperfine parameters of positively charged carbon vacancy in SiC", *Physica* B **308** 637-640 (2001).

[Shrader2011] D. Shrader, S. M. Khalil, T. Gerczak, T. R. Allen, A. J. Heim, I. Szlufarska, D. Morgan, "Ag diffusion in cubic silicon carbide", *J. Nucl. Mater*. **408** 257–271 (2011).

[Silva2013] D. J. Silva, U. Wahl, J. G. Correia, J. P. Araujo, "Influence of n^+ and p^+ doping on the lattice sites of implanted Fe in Si", *J. Appl. Phys.* **114** 103503(1-9) (2013).

[Silva2014a] D. J. Silva, U. Wahl, J. G. Correia, L. M. C. Pereira, L. M. Amorim, M. R. Da Silva, E. Bosne, J. P. Araújo, "Lattice location and thermal stability of implanted nickel in silicon studied by on-line emission channeling", *J. Appl. Phys.* **115** 023504 (2014).

[Silva2014b] D. J. Silva, U. Wahl, J. G. Correia, L. M. C. Pereira, L. M. Amorim, M. R. Da Silva, J. P. Araújo, "Origin of the lattice sites occupied by implanted Co in Si", *Semicond. Sci. Technol.* **29** 125006(1–5) (2014).

[Silva2016] D. J. Silva, U. Wahl, J. G. Correia, L. M. Amorim, M. R. da Silva, L. M. C. Pereira, J. P. Araújo, "Direct observation of the lattice sites of implanted manganese in silicon", *Appl. Phys.* A **122** 241 (2016).

[Silva2017] D. J. Silva, U. Wahl, J. G. Correia, L. M. Amorim, M. R. da Silva, L. M. C. Pereira, J. P. Araújo, "Lattice location of implanted Co in heavily doped n^+ and p^+ type silicon", *Appl. Phys.* A **123** 286(1–8) (2017).

[Takano2001] K. Takano, H. Nitta, H. Seto, C. G. Lee, K. Yamada, Y. Yamazaki, H. Sato, S. Takeda, E. Toya, Y. Iijima, "Volume and dislocation diffusion of iron, chromium and cobalt in CVD β-SiC", *Sci. Technol. Adv. Mater.* **2** 381–388 (2001).

[Usman2010] M. Usman, M. Nour, A. Y. Azarov, A. Hallén, "Annealing of ion implanted 4H-SiC in the temperature range of 100-800 °C analysed by ion beam techniques", *Nucl. Instruments Methods Phys. Res.* B **268** 2083–2085 (2010).

[Vetter2003] U. Vetter, H. Hofsäss, U. Wahl, M. Dietrich, "Lattice location studies of rare earth impurities in 3C-, 4H- and 6H-SiC", *Diam. Relat. Mater.* **12** 1883–1886 (2003).

[Wahl2000] U. Wahl, “Advances in electron emission channeling measurements in semiconductors”, *Hyperfine Interact*. **129** 349–370 (2000).

[Wahl2002] U. Wahl, J. G. Correia, A. Vantomme, Isolde Collabotation,”Lattice location of implanted Ag in Si”, *Nucl. Instruments Methods Phys. Res.* B **190** 543–546 (2002).

[Wahl2004] U. Wahl, J. G. Correia, A. Czermak, S. G. Jahn, P. Jalocha, J. G. Marques, A. Rudge, F. Schopper, J. C. Soares, A. Vantomme, P. Weilhammer “Position-sensitive Si pad detectors for electron emission channeling experiments”, *Nucl. Instruments Methods Phys. Res.* A **524** 245–256 (2004).

[Wahl2005] U. Wahl, J. G. Correia, E. Rita, J. P. Araújo, J. C. Soares, “Lattice sites of implanted Fe in Si”, *Phys. Rev.* B **72** 014115(1–8) (2005).

[Wahl2006] U. Wahl, J. G. Correia, E. Rita, J. P. Araújo, J. C. Soares, “Fe and Cu in Si: Lattice sites and trapping at implantation-related defects”, *Nucl. Instruments Methods Phys. Res.* B **253** 167–171 (2006).

[Wimbauer1997] T. Wimbauer, B. K. Meyer, A. Hofstaetter, A. Scharmann, H. Overhof, “Negatively charged Si vacancy in 4H SiC: A comparison between theory and experiment”, *Phys. Rev.* B **56** 7384–7388 (1997).

[Wright2016] E. Wright, J. Coutinho, S. Öberg, V. J. B. Torres, “Mössbauer parameters of Fe-related defects in group-IV semiconductors : First principles calculations”, *J. Appl. Phys.* **119** 181509(1–16) (2016).

[Ziegler2010] J. F. Ziegler, M. D. Ziegler. J. P. Biersack, “SRIM - The stopping and range of ions in matter (2010)”, *Nucl. Instruments Methods Phys. Res.* B **268** 1818–1823 (2010).

Chapter 4

Electrical dopant lattice location in SiC

As was discussed already in section 1.4, the most common electrical dopants in SiC are N and P as donors from group V and Al as acceptor from group III; B and Ga have been investigated, too, but found less suitable for the use in devices. Unfortunately, all of these elements are impossible or rather difficult to obtain as radioactive probes at ISOLDE. On the other hand, indium is readily available, giving the opportunity to explore its lattice location using emission channeling and thus also study the behaviour of an implanted group III element. It has been briefly mentioned in section 1.4 that it was not possible to obtain *p*-type SiC from In doping during growth, which clearly limits the interest in In as a practical electrical dopant in this material. However, its behaviour as an implanted impurity is still interesting from a fundamental point of view. This chapter is to be the base of a manuscript with title "Lattice location of implanted ^{124}In in 3C-SiC" (to be submitted). The emission channeling technique was used to extract crucial information about lattice location of ion implanted short-lived ^{124}In impurities and their interaction with defects in their vicinity, as a function of implantation temperature from room temperature up to 800 °C. Results are presented and summarized in this chapter.

4.1. Lattice location of ^{124}In in 3C-SiC

The lattice location of the radioactive isotope ^{124}In implanted into a 3C-SiC single crystal was investigated by means of the EC technique as function of the implantation temperature. For that purpose, the ^{124}In beams provided at ISOLDE were used, which actually consisted of a mixture of 73% ^{124}In ($t_{1/2}$=3.17 s) in its ground state and 27% of isomeric ^{124m}In ($t_{1/2}$=2.4 s). Both ^{124}In states decay to the stable isotope ^{124}Sn by means of β^- emission, and the EC technique is based on the observation of the overall anisotropic β^- intensity patterns emitted when the radioactive probe atoms are embedded in single crystals, as already explained in detail in chapter 2. The fact that the probe beam consisted of a mixture of two states with different β energy spectra [endpoint energies $E_{\beta,max}$(^{124}In)=6227 keV and $E_{\beta,max}$(^{124m}In)=4843 keV, average β energies <E_β>(^{124}In)=2045 keV and <E_β>(^{124m}In)=1609 keV] was taken into account when performing the *manybeam* simulations.

An undoped single-crystalline cubic 3C-SiC sample with <100> oriented surface was used. Mass separated and chemically clean beams of radioactive isotopes were provided by the on-line isotope separator ISOLDE-CERN facility [Jonson2000]. The intended radioisotope was produced by fission of uranium carbide UC_2 targets, induced by 1.4 GeV proton beams from the CERN PSB, followed by chemically selective laser ionization and electromagnetic mass separation. Since both ^{124}In and ^{124m}In are very short-lived isotopes with half-lives of a few seconds only, all EC measurements were performed on-line with implantation and measurement taking place simultaneously, at RT and subsequently at elevated temperatures, made possible by the use of a thermal shield of aluminated mylar in front of the detector, in a vacuum better than 10^{-5} mbar. The total implanted fluence at the end of the experiment was ~5×10^{12} cm^{-2}. SRIM [Ziegler2010] simulations show that each implanted In ion produces ~800 vacancies and interstitials. The corresponding range, straggle and peak concentration estimated for Gaussian implantation profile, are 232 Å, 61 Å and 2×10^{18} cm^{-3} respectively. The experimental conditions used for measuring ^{124}In:3C-SiC β^- emission yields, the necessary background correction procedure, fitting routine and relevant references are the same as for the TM:3C-SiC and are described in section 3.1.

4.1.1. 3C-SiC: ^{124}In fitting process

The patterns in Fig. 4.1(a-d) show the measured β^- emission yield in the vicinity of the <100>, <110>, <111> and <211> directions of the 3C-SiC sample directly during RT implantation of

^{124}In. The fact that prominent channeling is observed along all major axes and closest-packed planes ({110}, {111} and {100}) is clear evidence that the majority of In probes that are positioned on regular sites and hence contribute to the channeling effect, are located on substitutional Si sites. Indeed, it is possible to visually identify this by comparing the experimental patterns [Fig. 4.1(a-d)] with the corresponding simulated patterns for the ideal S_{Si} site, shown in Fig. 2.9(a). Note that although the simulated patterns, displayed in Fig. 2.9(a) for several ideal substitutional and interstitial sites, were calculated for ^{56}Mn probes, they are quite similar to the ^{124}In patterns which were used during the fit procedure.

The remaining patterns from Fig. 4.1(i-l) and (q-s) correspond to the measured β^- emission yield during 600 °C and 800 °C implantation. Besides an overall increase in the intensity of all channeling effects, there are no evident changes in the experimental patterns. Only with a quantitative analysis by fitting simulated patterns to the observed yields was it possible to obtain information on the occupied sites, with figures 4.1(e-f) presenting the best fit results for the RT implantation and Fig. 4.1(m-p) and (t-v) those for 600 °C and 800 °C implantation.

Single fractions on regular sites were first considered for the initial fitting process. It was confirmed that only one type of site contributes to the best fits for RT and through all the high-temperature implantation steps up to 800 °C, and that this site is the substitutional Si site. Note that the experimental results can only be satisfactorily described if, in addition to the fraction of In atoms in regular sites, it is also allowed for a fraction on "random" sites, which contributes with an isotropic yield.

Next, the displacements from the ideal S_{Si} site towards BC, AB_{Si}, SP_{Si} and D_{Si} interstitial sites were also tested. The best fit, for the RT patterns, was obtained for a static displacement of (0.1–0.2) Å from S_{Si} towards the AB_{Si} site, a value which is larger than the thermal vibration amplitude of Si and C in SiC, which are u_1(Si)=0.060 Å, u_1(C)=0.061 Å (reference values, already discussed in chapter 2), suggesting that the implanted In atoms are somewhat displaced from the perfect S_{Si} sites.

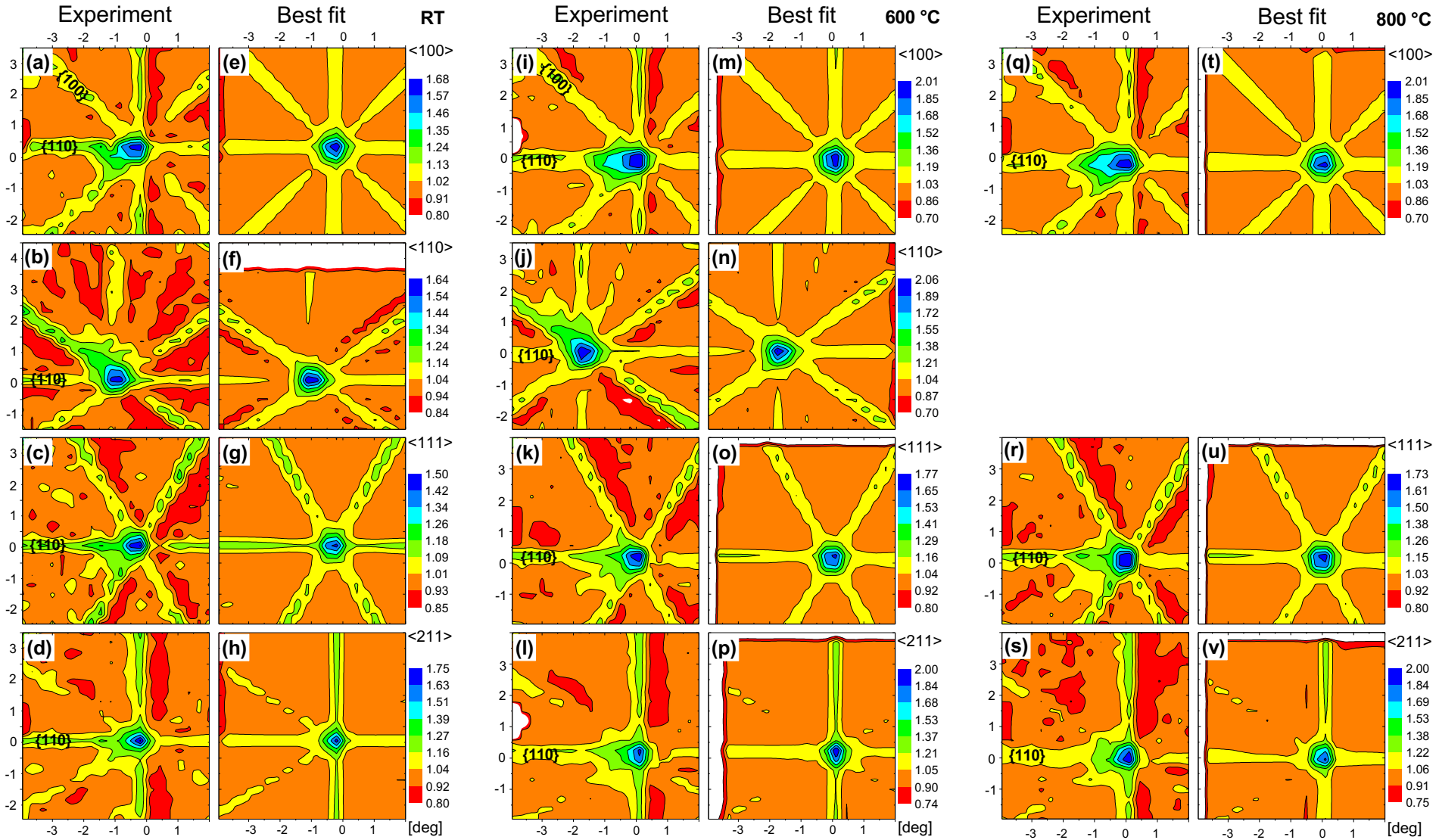

Figure 4.1. Normalized experimental ^{124}In β^- emission channeling patterns in the vicinity of <100>, <110>, <111> and <211> directions during RT (a-d), 600 °C (i-l) and 800 °C implantation (q-s) into 3C-SiC. The plots (e-h), (m-p) and (t-v) are the corresponding best fits of theoretical patterns. Note that in some cases the crystal was oriented during experiment in such a way that the recorded patterns included areas which were further than 3° away from a major crystallographic direction. Since the *manybeam* simulations were restricted to an angular range of ±3° from the axes, the corresponding areas along the edges or corners of patterns (f), (h), (m), (o), (p), (t), (u) and (v) are shown in white.

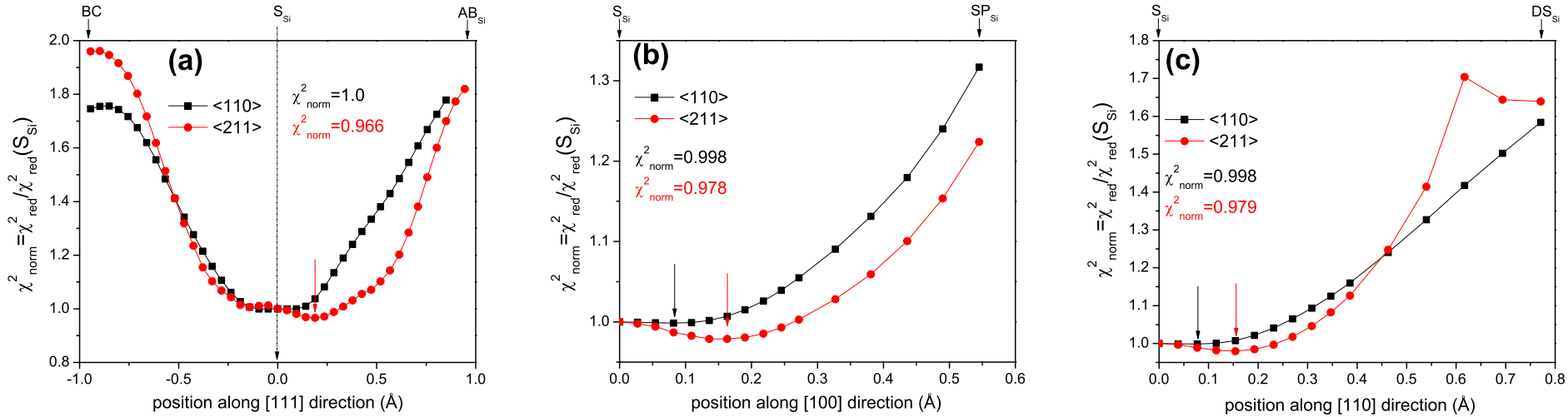

Figure 4.2. Normalized χ^2_{norm} of 1-site fits to <110 and <211> patterns as a function of displacement from the ideal S_{Si} site for ^{124}In during RT implantation. (a) is the displacement along [111] towards BC and AB_{Si}, (b) along [100] towards SP_{Si} and (c) along [110] towards D_{Si}. The χ^2 was in all cases normalized to that for the one-site fit of the ideal substitutional Si site. The full arrows (black and red), indicate the displacement positions where the lowest χ^2 was obtained, and the dashed arrow, located in (a), represents the starting reference point for the displacements.

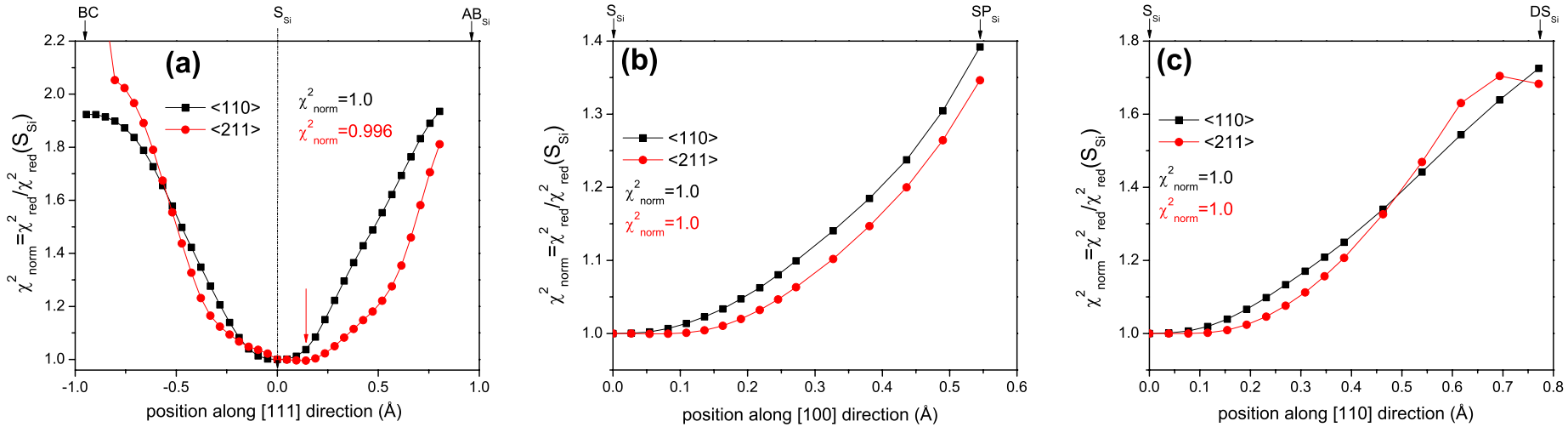

Figure 4.3. Same as Fig. 4.2, but for implantation at 600 °C.

This displacement represents only, at maximum, a ~4% improvement in χ^2_{norm} with regards to the value obtained for the ideal S_{Si} site, and yields only slightly better fit than the ones obtained for displacements towards BC, SP_{Si} or DS_{Si} sites. Nevertheless, the improvements in fit quality are quite comparable and consequently it is not possible to identify a preferred direction for the displacement from the ideal S_{Si} position (Fig. 4.2). For implantation at 300 °C the In probe displacement decreased to approximately the values of u_1(Si,C), which leads to In incorporation into the ideal Si substitutional site. Further increase of the implantation temperature to 600 °C and 800 °C does not alter the displacements (Fig 4.3 displays the In static displacement from the ideal S_{Si} site for the 600 °C implantation). The possibility for more than one regular site being occupied was also explored. In particular, tetrahedral interstitial Si-coordinated (T_{Si}) and tetrahedral interstitial C-coordinated (T_C) sites were also analysed. For example, a combination of sites (S_{Si}+T_C) yielded T_C fractions that were always negative or very close to zero. Similarly, the combination of sites (S_{Si}+T_{Si}) improved the χ^2_{norm} below 5%.

4.2. Discussion

In order to interpret the incorporation of In into near substitutional Si sites, the defect situation following ion implantation has to be considered. The SRIM simulation indicates that initially around 400 Si vacancies, as well as a similar number of C vacancies and corresponding interstitials are created per implanted atom. The damage created offers ample possibilities for In probes to be incorporated in different types of lattice sites and forming complexes with crystal defects. Nevertheless, Miyata *et al*. predicted on the basis of *ab initio* calculations for 4H-SiC, that In impurities prefer to substitute on a silicon site [Miyata2008]. This result confirmed the previous experimental works using PAC spectroscopy technique, done by Licht *et al*. and Achtziger *et al*., in 4H- and 6H-SiC samples [Licht1997, Achtziger1998]. Figure 4.4(b) shows the fitted In fraction for the considered sites (near S_{Si} after RT and ideal S_{Si} at higher temperatures) as function of implantation temperature, reaching a maximum of 45% during 800 °C implantation, but well below the 100% mark. The 6% In fraction increase on substitutional Si sites during the 600 °C implantation coincides with the probe's shift to the ideal substitutional position, indicated by the static displacements being below the thermal vibration amplitude of the Si and C atoms, Fig. 4.4(a).

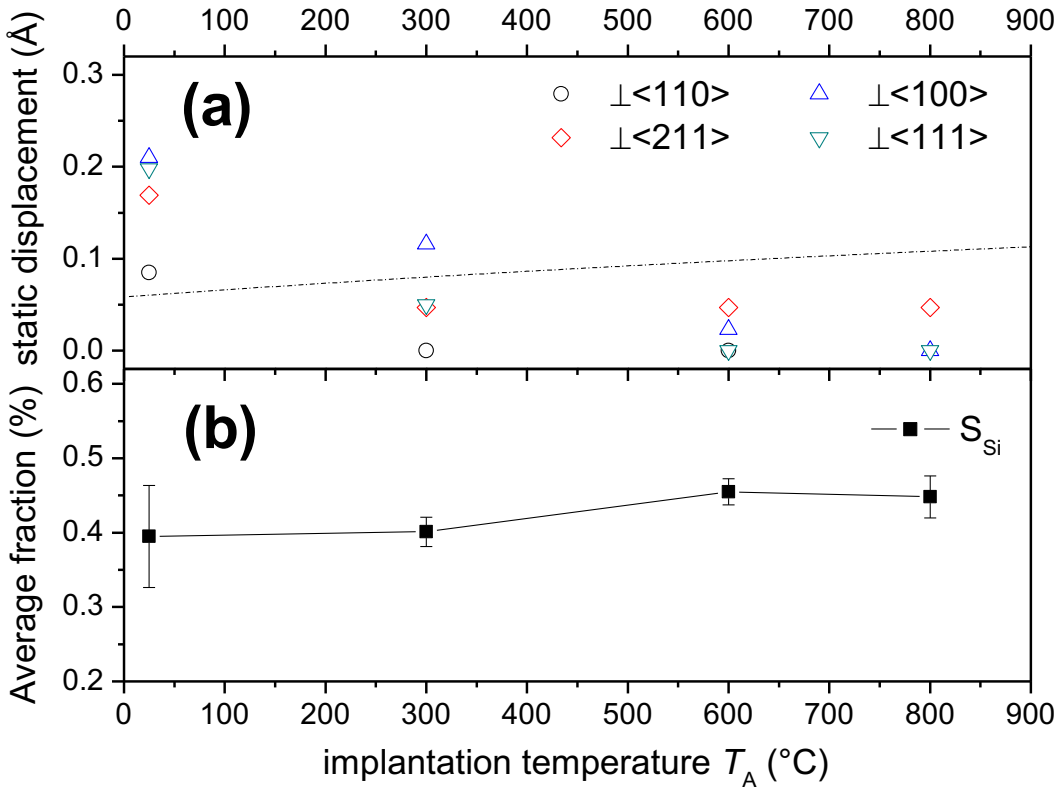

Figure 4.4. (a) One-dimensional rms displacements perpendicular to the channeling axes, from the fits as a function of implantation temperature. The dashed line corresponds to the thermal vibration amplitude dependence with temperature of Si in SiC. Panel (b): Fitted fractions of ^{124}In emitter atoms on substitutional Si sites as a function of the annealing temperature, averaged for the four measured crystallographic directions. The error bars represent the spread in fitted fractions for the different crystallographic directions.

This result can be explained if one takes into account the effects related to implantation damage and its annealing and can be considered a sign of the local recovery of the defective host lattice. This was already observed for TM:SiC and discussed in detail in section 3.2.3.

Reports on implanted In atom impurities in SiC are scarce [Meier1994, Licht1997, Achtziger1998]; these works studied the formation and the stability of indium complexes in 3C-, 4H- and 6H-SiC using PAC spectroscopy at RT and annealing temperatures up to ~1530 °C, however, the implanted fluences are not mentioned in any of the three publications. All authors reported the presence of In probes at substitutional Si sites after RT implantation, although the fraction stays below 5% for annealing temperatures below 600 °C. Above this annealing temperature, Licht *et al.* and Achtziger *et al.* [Licht1997, Achtziger1998] report maximum substitutional In fractions of ~17% upon annealing 4H-SiC at 1530 °C, and ~30% after annealing 6H-SiC at ~1080 °C. Nonetheless, in the annealing temperature range of 600 °C-800 °C all reported In fractions located at substitutional Si sites are far below the ones found in the present work. The authors also reported the appearance of In complexes of the type

In-V_C, after annealing at ~1020 °C, justified by the start of segregation of carbon to the SiC surface and consequent formation of carbon vacancies. It is not possible to study the lattice location of ^{124}In impurities in this temperature regime due to technical limitations associated with the chosen probe and the online EC experimental setup. On the one hand, due to the necessity of implanting the probes while measuring at the same time, acquiring EC data for annealing temperatures above 800 °C is not possible for the ^{124}In probe without damaging the 2D pad detector by excessive light emitted from the sample. On the other hand, the online experimental setup can in any case only reach, at maximum, an annealing temperature of 900 °C.

Ion implantation results in the creation of atomic-level defects whose accumulation can induce amorphization, dopant diffusion or detrimental dopant-defect interactions. The latter is usually considered as the reason why the implanted dopants are not electrically active after the implantation process. The electrical activation of ion implanted dopants requires both their incorporation on the proper lattice sites, i.e. usually substitutional sites, plus the removal of electrically compensating defects resulting from the implantation damage. In most cases, e.g. in Si, Ge, or GaAs, this can be performed after the ion implantation, known as a post-implant annealing step.

Although a considerable part of the implantation-induced damage in SiC can be removed at 1200 °C, to achieve reasonable electrical activation annealing at temperatures in excess of 1500 °C is needed because of the high bond strength of the SiC lattice. Even in this case post-implant annealing alone may not be sufficient, and studies have also been performed on how to decrease the damage formation via performing high-temperature implants. The detrimental action of radiation damage on the electrical activity of nitrogen donors in SiC has been investigated by Åberg *et al* [Åberg2001]. They found that in *n*-type SiC free electron concentrations are severely depleted following the irradiation with MeV ions of H, He, B and Al, but that the effect can be considerably reduced at irradiation temperatures above 600°C. For the doping of SiC by means of ion implantation of N, P, Al or B usually implantation temperatures around 400-600 °C followed by post-implant annealing at 1500-1700 °C are chosen [Laube2002, Hallén2016].

The only study that could be found in the literature reporting on the attempt of SiC doping by means of In ion implantation is the work of Hart [Hart1971], who implanted 40 keV In ions at fluences above 10^{14} cm^{-2} into 3C- and 6H-SiC at various temperatures. Rutherford Backscattering Spectroscopy/Channeling (RBS/C) studies indicated that ~90% of In atoms were substitutional following 450 °C 3×10^{14} cm^{-2} implantation into 3C-SiC and annealing at 1200 °C, and ~95%

aligned with the c-axis in 6H-SiC after 350°C 1×10^{14} cm^{-2} implantation and 1200 °C annealing (the exact lattice site of In could not be determined in these studies). However, electrical characterization indicated weak *p*-type character only in the 6H sample if it was annealed at 1000 °C or less, and the authors concluded that this "may be due to acceptor behaviour of the implanted In. However, it is possible that some yet unidentified acceptor type defect exists at these temperatures."

Up to date, no report about experimental measurement of the In acceptor ionization energy has been made. Only an *ab initio* study can be found, done by Miyata *et al.* [Miyata2008] who calculated the ionization energy of indium in 4H-SiC: $E_a(Si_h)$~150 meV and $E_a(Si_k)$~260 meV. As a comparison, the aluminium ionization energy in 3C-SiC, at substitutional Si site, is E_a(Si)=254 meV [Ikeda1980], and in 4H-SiC is $E_a(Si_h)$=197.9 meV and $E_a(Si_k)$=201.3 meV [Ivanov2005]. Accepting the values calculated by Miyata *et al*., they are similar to the ones obtained for aluminium, which implies that indium can be an option as a shallow acceptor to aluminium if considered only the ionization energy values. However, the reported indium solubility (9.5×10^{16} cm^{-3} at 2500 °C) is 4-5 orders of magnitude lower than the solubility of aluminium (2×10^{21} cm^{-3}) [Harris1995], which should undoubtedly limit the applicability of indium as an electrical dopant. On the other hand, since Hart [Hart1971] has already reported successful substitutional In incorporation of $>10^{20}$ cm^{-3} by means of ion implantation, this may not be a limiting factor either.

Finally, it will be interesting to compare the current experiment on ^{124}In:3C-SiC to previous lattice location results for the same element in other group IV semiconductors – diamond and silicon [Dezsi1985, Lindner1986, Alves1991, Hofsäss1993, Quintel1996, Bharuth2001]. Concerning the system In:(*n*-type)Si, Lindner *et al.* [Lindner1986] reported 55%-60% of ^{112m}In and ^{114m}In probes located at substitutional Si sites after RT implantation. Upon annealing at 427 °C an increase in the channeling yield was observed and associated to the rearrangements of In atoms and removal of radiation damage inside the Si lattice. The work done by Alves *et al.* [Alves1991] complemented the previous work by studying the In thermal stability of a similar system In:(*p*-type)Si up to 900 °C by means of RBS/C. The author reported an In fraction of 50% located at substitutional Si sites after annealing at 550 °C. Consequent annealing at higher temperatures resulted in loss of substitutional In that was attributed to the formation of In precipitates. In stark contrast Dezsi *et al.* [Dezsi1985] using as well RBS/C reported an In fraction below 20% on substitutional Si sites after RT implantation and, with subsequent annealings up to 1000 °C, a steady In fraction increase to a maximum of 70% on the same site. Lindner *et al.* tentatively addresses the difference in results in his work. Concerning In in

diamond, both Hofsäss *et al*. [Hofsäss1993] and Quintel *et al.* [Quintel1996] reported strong conversion electron emission channeling effects corresponding to ^{111}In probes located at substitutional C sites after annealing in the temperature range 1000 °C-1200 °C with fractions reaching a maximum of 45%. ^{111}In probes located at interstitial sites were also considered, by both authors, but estimated below 10%. Bharuth-Ram *et al*. [Bharuth2001] reached similar results, reporting an ^{111}In fraction of 32% on substitutional C sites, however, in this case after annealing at 1200 °C they also identified a fraction of 10% in tetrahedral interstitial sites. How do the In:3C-SiC results relate to the ones briefly discussed here for the silicon and diamond semiconductors? Contrary to silicon, SiC and diamond present high radiation hardness due to their high bond-strength, which is illustrated by their short bond length, 1.54 Å for (C–C) and 1.89 Å for (Si–C), against 2.35 Å for Si. On the other hand, the host lattice damage produced by the ion implantation process needs very high annealing temperatures, well above 1000 °C, to recover and activate the implanted dopants. All of these materials will suffer amorphization if the damage density threshold, produced by ion implantation process, is surpassed. This damage density is often expressed in the number of displacements per host atom (dpa) needed to turn the structure amorphous. While for SiC at RT this threshold is crossed if implanted ions have created ~4×10^{22} vacancies/cm^3 (~0.45 dpa) [Debelle2010], for diamond the critical damage level is found to be only ~10^{22} vacancies/cm^3 (~0.06 dpa) [Kalish1999] (atomic densities in SiC and diamond are 9.65×10^{22} atoms/cm^3 and 1.76×10^{23} atoms/cm^3, respectively); for Si values from 0.02-0.2 dpa can be found in the literature [Pelaz2004]. Although recrystallization of amorphous SiC is possible [Jiang1999, Bae2004, Jiang2009], amorphization of diamond is an irreversible process (identified as graphitization), where upon annealing new carbon bonds can be formed with sp^2 instead with sp^3 hybridization (more detail about this subject can be found in [Kalish1999, Zeidler1993]). In stark contrast, silicon is known to easily recover its crystalline structure: even discrete amorphous regions (nanometer sized) produced by implantation of heavy ions are annealed at temperatures below 400 °C, and solid phase epitaxial regrowth (SPEG) of a fully amorphous layer starts at 550 °C [Pelaz2004]. In all cases, the fact that emission channeling effects could already be measured in the RT as-implanted state in Si, SiC and diamond, readily proves that the implanted fluences were below the threshold for amorphization. It is possible to provide a rough estimation of the number of vacancies/cm^{-3} produced in the works of [Hofsäss1993, Quintel1996, Bharuth2001] on diamond, since the maximum used implantation energies are known, as well as the In implantation fluence range. These parameters can then be used as inputs in SRIM in order to

calculate the near-Gaussian implantation profile and the peak concentration of vacancies produced inside the host lattice. As a result, one estimates ~10^{21} vacancies/cm^3, value of the same order of magnitude of the one estimated for this experiment. Increases in the intensity of emission channeling effects during thermal annealing, as observed in Si around 427 °C [Lindner1986] and in diamond above 1000 °C, then show the existence of major damage annealing steps. In the current study, the fact that ^{124}In emission channeling effects increased at an implantation temperature of 600 °C are also in accordance with damage reduction at that implantation temperature seen in other studies, e.g. [Åberg2001, Laube2002, Hallén2016]. The In fraction located at substitutional sites is similar for both SiC and diamond, maximum of 45% for ^{111}In:C after annealing >1000 °C against 45% in ^{124}In:3C-SiC following implantation at 800 °C.

4.3. Conclusions

As described in this chapter, the In lattice location was experimentally determined in undoped 3C-SiC. The fits of the experimental patterns assign 39% of the implanted In dopants near substitutional Si sites - static displacement estimated of (0.1 Å-0.2 Å) along the <111> direction towards AB_{Si} site, after RT ion implantation. While the substitutional incorporation occurs already in the as-implanted state, annealing at 600 °C is required to promote substitutional In with rms values below the thermal vibration amplitude of the Si and C atoms, which corresponds to perfect substitutional incorporation of In at Si sites. This confirms the theoretical prediction, which suggested that In atoms in SiC are most stable in substitutional Si sites [Miyata2008]. Also, at this implantation temperature an increase of the substitutional In fraction to a maximum of 45% was observed. Both increase of the In substitutional fraction by 6% and the promotion of the In probes location to ideal S_{Si} sites in the temperature range 300 °C – 600 °C, are a clear indication of the recovery of the host lattice.

References

[Åberg2001] D. Åberg, A. Hállen, P. Pellegrino, B. G. Svensson, "Nitrogen deactivation by implantation-induced defects in 4H-SiC epitaxial layers", *Appl. Phys. Lett.* **78** 2908-2910 (2001).

[Achtziger1998] N. Achtziger, D. Forkel-Wirth, J. Grillenberger, T. Licht, W. Witthuhn, "Identification of deep band gap states in 4H- and 6H-SiC by radio-tracer DLTS and PAC-spectroscopy", *Nucl. Instruments Methods Phys. Res.* B **136–138** 756–762 (1998).

[Alves1991] E. Alves, M. F. da Silva, J. May, V. Haslar, P.Seidl, U. Feuser, R. Vianden, "Epitaxial regrowth and lattice location of indium implanted in arsenic-preamorphized silicon", *Nucl. Instruments Methods Phys. Res.* B **55** 580–584 (1991).

[Bae2004] In-Tae Bae, M. Ishimaru, Y. Hirotsu, "Solid phase epitaxy of amorphous silicon carbide: ion fluence dependence", *J. Appl. Phys*. **96** 1451–1457 (2004).

[Bharuth2001] K. Bharuth-Ram, A. Burchard, M. Deicher, H. Quintel, M. Restle, H. Hofsäss, C. Ronning, "Implantation sites of In, Cd and Hf ions in diamond", *Phys. Rev*. B **64** 195207(1–8) (2001).

[Debelle2010] A. Debelle, L. Thomé, D Dompoint, A. Boulle, F. Garrido, J. Jagielski, D. Chaussende, "Characterization and modelling of the ion-irradiation induced disorder in 6H-SiC and 3C-SiC single crystals", J. Phys. D: Appl. Phys. **43** 455408(1-7) (2010).

[Dezsi1985] I. Dezsi, L. Hermans, J. Van Cauteren, M. Rots,"A TDPAC study of the lattice location of implanted indium in silicon", *Rad. Eff. Lett*. **85** 277–282 (1985).

[Hallén2016] A. Hallén, M. Linnarsson, "Ion implantation technology for silicon carbide", *Surface & Coatings Technol.* **306** 190–193 (2016).

[Harris1995] G. L. Harris, in *Properties of Silicon Carbide* (INSPEC, Exeter, 1995), chapter 7, pp. 155.

[Hart1971] R.R. Hart, H.L. Dunlap, O.J.Marsh, "Backscattering analysis and electrical behavior of SiC implanted with 40 keV indium", *Ion Implantation in Semiconductors* ed I. Ruge and J. Graul (Springer, Berlin, Heidelberg, 1971) pp. 134–140.

[Hofsäss1993] H. Hofsäss, M. Restle, U. Wahl, E. Recknagel, "Lattice location and annealing studies of heavy ion implanted diamond", *Nucl. Instruments Methods Phys. Res.* B **80–81** 176–179 (1993).

[Ikeda1980] Ikeda, M., H. Matsunami, T. Tanaka, "Site effect on the impurity levels in SiC", *Phys. Rev*. B **22** 2842–2854 (1980).

[Ivanov2005] I. G. Ivanov, A. Henry, E. Janzén, "Ionization energies of phosphorus and

nitrogen donor and aluminium acceptors in 4H silicon carbide from the donor-acceptor pair emission", *Phys. Rev*. B **71** 241201(1–4) (2005).

[Jiang1999] W. Jiang, W. J. Weber, S. Thevuthasan, D. E. McCready, "Displacement energy measurements for ion-irradiated 6H-SiC", *Nucl. Instruments Methods Phys. Res. Sect.* B **148** 557–561 (1999).

[Jiang2009] W. Jiang, W. J.Weber, J. Lian, N. M. Kalkhoran, "Disorder accumulation and recovery in gold-ion irradiated 3C-SiC", *J. Appl. Phys*. **105** 013529(1–6) (2009).

[Jonson2000] B. Jonson, A. Ritchter, "More than three decades of ISOLDE physics", *Hyperfine Interact.* **129** 1–22 (2000).

[Kalish1999] R. Kalish, A. Reznik, S. Prawer, D. Saada, J. Adler, "Ion-implantation-induced defects in diamond and their annealing: expriment and simulation", *Phys. Stat. Sol*. A **174** 83–89 (1999).

[Laube2002] M. Laube, F. Schmid, G. Pensl, G. Wagner, M. Linnarsson, M. Maier, "Electrical activation of high concentrations of N^+ and P^+ ions implanted into 4H-SiC", *J. Appl. Phys*. **92** 549–554 (2002).

[Licht1997] T. Licht, N. Achtziger, D. Forkel-Wirth, K. Freitag, J. Grillenberger, M. Kaltenhäuser, U. Reislöhner, M. Rüb, M. Uhrmacher, W. Witthuhn, ISOLDE Collaboration, "Hafnium cadmium and indium impurities in 4H-SiC observed by perturbed angular correlation spectroscopy", *Diam. Rel. Mater*. **6** 1436-1439 (1997).

[Lindner1986] G. Lindner,H. Hofsäss, S. Winter, B. Besold, E. Recknagel,G.Weyer, J. W. Petersen, "Direct evidence for substitutional ion-implanted indium dopants in silicon", Phys. Rev. Lett. **57** 2283–2286 (1986).

[Meier1994] J. Meier, D. Forkel-Wirth, T. Licht, U. Reislöhner, M. Uhrmacher, W. Witthuhn, ISOLDE Collaboration, "Perturbed-angular-correlation spectroscopy on indium and cadmium-complexes in silicon carbide", *Mat. Res. Soc. Symp. Proc.* **339** 613–618 (1994).

[Miyata2008] M. Masanori, Y. Higashiguchi, Y. Hayafuji, "*Ab Initio* study of substitutional impurity atoms in 4H-SiC", *J. Appl. Phys.* **104** 123702(1–4) (2008).

[Pelaz2004] L. Pelaz, L. A. Marqués, J. Barbolla, "Ion-beam-induced amorphization and recrystallization in silicon", *J. Appl. Phys*. **96** 5947(1–30) (2004).

[Quintel1996] H. Quintel, K. Bharuth-Ram, H. Hofssäss, M. Restle, C. Ronning, "Emission channeling study of annealing of radiation damage in heavy-ion implanted diamond", *Nucl. Instruments Methods Phys. Res.* B **118** 72–75 (1996).

[Zeidler1993] J. R. Zeidler, C. A. Hewett, R. G. Wilson, "Carrier activation and mobility of

boron-dopants in ion-implanted diamond as a function of implantation conditions", *Phys. Rev*. B **47** 2065–2071 (1993).

[Ziegler2010] J. F. Ziegler, M. D. Ziegler. J. P. Biersack, "SRIM - The stopping and range of ions in matter (2010)", *Nucl. Instruments Methods Phys. Res.* B **268** 1818–1823 (2010).

Chapter 5

To give a broader view of the main achievements of this work, the conclusions of the last two chapters are reviewed in a more general perspective. This chapter ends with some suggestions for further research.

Conclusions

The possible lattice sites of a foreign atom in a semiconductor are of fundamental importance since they determine its electrical, optical or magnetic properties as a dopant or contaminant. Surprisingly, for SiC there existed very little knowledge on the lattice sites of impurities.

The main aim of this thesis was to achieve new insights into the structural properties of the 3*d* and 4*d* transition metals (TMs) in SiC by investigating the lattice location of the 3*d* TM probes ^{56}Mn, ^{59}Fe, ^{65}Ni and the 4*d* TM probe ^{111}Ag. Two different lattice sites were identified in each case: while both 3*d* and 4*d* probes share a preference for displaced substitutional Si sites, the second type of lattice site differed profoundly, with the 3*d* probes ^{56}Mn, ^{59}Fe and ^{65}Ni atom occupying C-coordinated tetrahedral interstitial sites whereas ^{111}Ag was found in the neighbourhood of substitutional C and BC positions. The direct evidence for the occupation of each site and its related thermal stability allowed a more detailed understanding of some microscopic mechanisms at play, which are described in the following.

The interaction of the transition metal impurities with defects (vacancy and self-interstitial related), induced by the ion implantation process plays an important role in the reliability of SiC to work as intended as a semiconductor.

It was found that the 3*d* transition metals were preferentially located at ideal tetrahedral interstitial carbon coordinated sites after the implantation process, but also at near substitutional Si sites, albeit with lower fraction values. This result expands the information available in literature, where so far only substitutional Si sites were considered to be occupied by the transition metals. This work also clearly showed that only a part of the transition metals migrated from the initial interstitial to substitutional Si positions with the thermal treatments, with the remaining fraction going to the so-called "random" positions. These site changes are attributed to the onset of migration of interstitial TMs, for which activation energies of E_M=1.7-3.2 eV are estimated in this work. However, by comparing these migration energies with the activation energy attributed by theoretical and experimental works to the transformation of silicon vacancies into a complex V_C-C_{Si} antisite defect (2.2-2.5 eV), it was concluded that the site changes to random sites indicate that silicon vacancies have become unavailable as major traps in the same temperature regime. This work also showed that the behaviour of the three investigated 3*d* transition metals is similar, irrespective of the element and the SiC polytype used as a host.

The lattice location of ^{111}Ag in 3C- and 6H-SiC polytypes showed that the Ag probes, besides being preferentially located at near-substitutional Si sites, with a smaller fraction were also found on sites near substitutional C and BC positions, which is in stark contrast to the 3*d* TMs studied in this thesis. Also, after low-fluence implantation, up to 19% of the Ag atoms are located on displaced substitutional Si sites, whereas the highest-fluence implantation resulted in a lower substitutional fraction of only 3-5% for both SiC polytypes. Because of the larger defect concentration in the latter case, the remainder located on lattice sites with heavily damaged surroundings, most likely locally amorphized, once again showing the importance of implantation induced defects in the host lattice. It was verified that silver atoms located at substitutional Si sites start to diffuse after annealing at 1075 °C with an estimated activation energy interval of 3.1 eV-4.1 eV. While several experimental and theoretical studies are available in the literature regarding the Ag diffusion in SiC, there is still no agreement on the specific mechanism that mediates the diffusion process. Nevertheless, one of the results provided by the literature, a process mediated by a kick-out mechanism by silicon self-interstitials with calculated activation energies of 2.71 eV-3.35 eV, fits quite well with the energy range obtained in this thesis. However, since kick-out and simple Frank-Turnbull diffusion (spontaneous ejection of Ag without the participation of a Si interstitial) have essentially the same consequences on the fraction of Ag disappearing from substitutional sites, the EC technique is unable to provide further insights about the origin of the Ag instability.

Finally, while this thesis focuses mainly on TMs since these elements are well established probes at ISOLDE, indium appears as an added bonus due to its availability as a probe and considered a *p*-type SiC dopant candidate, if incorporated in electrically active substitutional sites. Still, very little is known, even today. Few experimental works could be found in the literature, which reported the location of In atom probes on substitutional positions, although presenting a wide range for the maximum fraction values on these sites, from ~20% up to 95%. The answer to whether In is suitable for *p*-type doping or not, depends on two factors: (1) In incorporation on the substitutional Si sites and (2) the removal of electrically compensating defects resulting from the implantation damage. While the first factor was shown in the literature to be achieved by hot In implantation and post annealing at 1200 °C, the existence of electrically compensating defects and their identification are still an open question. The available literature only reports on the formation of In complexes of the type In–V_C, after annealing at ~1020 °C, justified by the start of segregation of carbon to the SiC surface and consequent formation of carbon vacancies, but no comment is made whether or not this complex can be considered an electrically compensating defect.

Here, the lattice location of In in 3C-SiC was clearly identified. This work showed that In sits preferably on substitutional Si sites, reaching a fraction occupation of 45% following implantation at 800 °C. Unfortunately, it was not possible to confirm the In fraction values >90% occupying the substitutional sites, reported in the literature after annealing at 1200 °C due to the experimental setup limitations, already pointed out in section 4.2. Also, due to this experimental limitation, it was not possible to confirm the In–V_C complex defect formation.

As a final remark, compared with silicon, silicion carbide technology is in its infancy where much remains to be done. In that regard, the author believes that this work contributed to giving additional insight into the issues raised in the introduction of this thesis.

Perspectives

The present work opened several perspectives for future research for both TMs and electrical dopants in SiC. In this context, a summary of topics for future work is presented in the following. The 3*d* TMs Co and Cu are also known to introduce deep levels in semiconductors such as silicon. It would be interesting to extent the lattice location studies to these elements, as they are readily available at ISOLDE and because on the one hand, there is little information available in the literature, on the other hand, to confirm whether the observed fraction evolution with the thermal treatment, which was found to be independent from the used SiC polytype for the other 3*d* TMs (Mn, Fe and Ni) studied in this thesis, is also valid for Co and Cu.

Regarding the electrical dopants of SiC, theoretical calculations available in the literature report that antimony introduces a much shallower donor level when compared with the more conventional *n*-type dopants such as nitrogen and phosphorus. Being also a probe available at ISOLDE and successfully used before for emission channeling experiments, it would be interesting to complement the In study made in this work. It should be noted that the study of antimony was one of the objectives of this thesis. However, the isotope ^{124}Sb ($t_{1/2}$=60 d), which was previously used for EC studies in ZnO and GaN, was not available at ISOLDE during the time frame of this thesis. Attempts to replace it by using ^{128}Sb (9 h) populated by decay of ^{128}Sn (59 min) were unsuccessful, due to complications with the branching ratios of the decay scheme.

Lastly, recently beryllium was implemented successfully as a probe at ISOLDE and beam time is already scheduled for EC measurements on the lattice location of ^{11}Be (13.6 s) in SiC. The literature reports that this element has been found to be an amphoteric impurity in this semiconductor and has been shown that by ion implantation it can be used to fabricate *p*-type 6H-SiC. Also starting this year, Aluminium will be available as a probe at ISOLDE. Being a usually used *p*-type dopant in SiC, EC studies can add valuable information about its location inside the host lattice. The ^{28}Al (2.2 min) or ^{29}Al (6.6 min) are two suitable candidates to do on-line EC measurements.

Appendix A

Root mean square (rms) displacement study

As was outlined already in section 2.5.1 (Table 2.1), varying values for rms displacements of Si and C atoms for different polytypes of silicon carbide can be found in the literature. They scatter considerably, ranging from u_1(Si)=0.034 Å, u_1(C)=0.048 Å [Stelmakh2007] to u_1(Si)=0.070 Å, u_1(C)=0.070 Å [Peng2009]. The *manybeam* simulations rely on the rms displacement values, so the choice of a specific pair of u_1 values is of considerable importance because it will affect the analysis results.

To tackle this problem, two pairs of u_1 values were chosen: u_1(Si)=0.060 Å, u_1(C)=0.061 Å [Schulz1979] and u_1(Si)=0.044 Å, u_1(C)=0.049 Å in order to see how the analysis results of 3C-SiC:^{59}Fe data are affected. Two sets of libraries containing simulated patterns, around <110> and <211> directions were produced. Two-site fits were made, where one position was fixed at the ideal T_C site and the other was displaced from ideal Si towards four different interstitial positions BC, AB_{Si}, SP_{Si} and DS_{Si}. This analysis was made for ^{59}Fe data measured at room temperature and after annealing at 500 °C and 800 °C and can be found in subsections A.1, A.2 and A.3. In subsection A.4, the fitted fractions of Fe emitter atoms sitting on ideal substitutional Si and interstitial T_C sites plus the sum of both sites as function of the annealing temperature, are compared for both rms displacements.

Looking at the results presented in these subsections, the following comments can be made. First, the behaviour of the χ^2_{norm}, for both rms displacement values, when Fe is displaced towards BC, AB_{Si}, SP_{Si} or DS_{Si} is similar. Second, the best fit (indicated by the red and black

arrows) is always in a position somewhat further away from the ideal substitutional Si for the simulations using lower rms displacements.

This can be understood as follows. The angular width of channeling effects is a function of the rms displacements of the host atoms, as well as of rms and static displacements of the probe atoms. As a rule of thumb, an increase in any of these displacements will narrow the angular width of channeling effects. Hence, if experimental patterns of a given angular width are e.g. fitted with patterns that were simulated assuming smaller rms host displacements, the best fit will usually be obtained for larger probe atom displacements, and vice versa.

Third, concerning the results of subsection A.4, the fitted Fe fractions using different rms displacements are, overall, very similar. Generally, all the fractions tend to be higher if smaller SiC rms displacements are used in the simulations. At maximum a difference of ~10% is obtained for the Fe fraction sitting in the interstitial T_C position.

In conclusion, despite of the uncertainty in the SiC rms displacement values available in the literature, one is sure that either value of rms displacement is adequate for our data analysis.

A.1. At room temperature

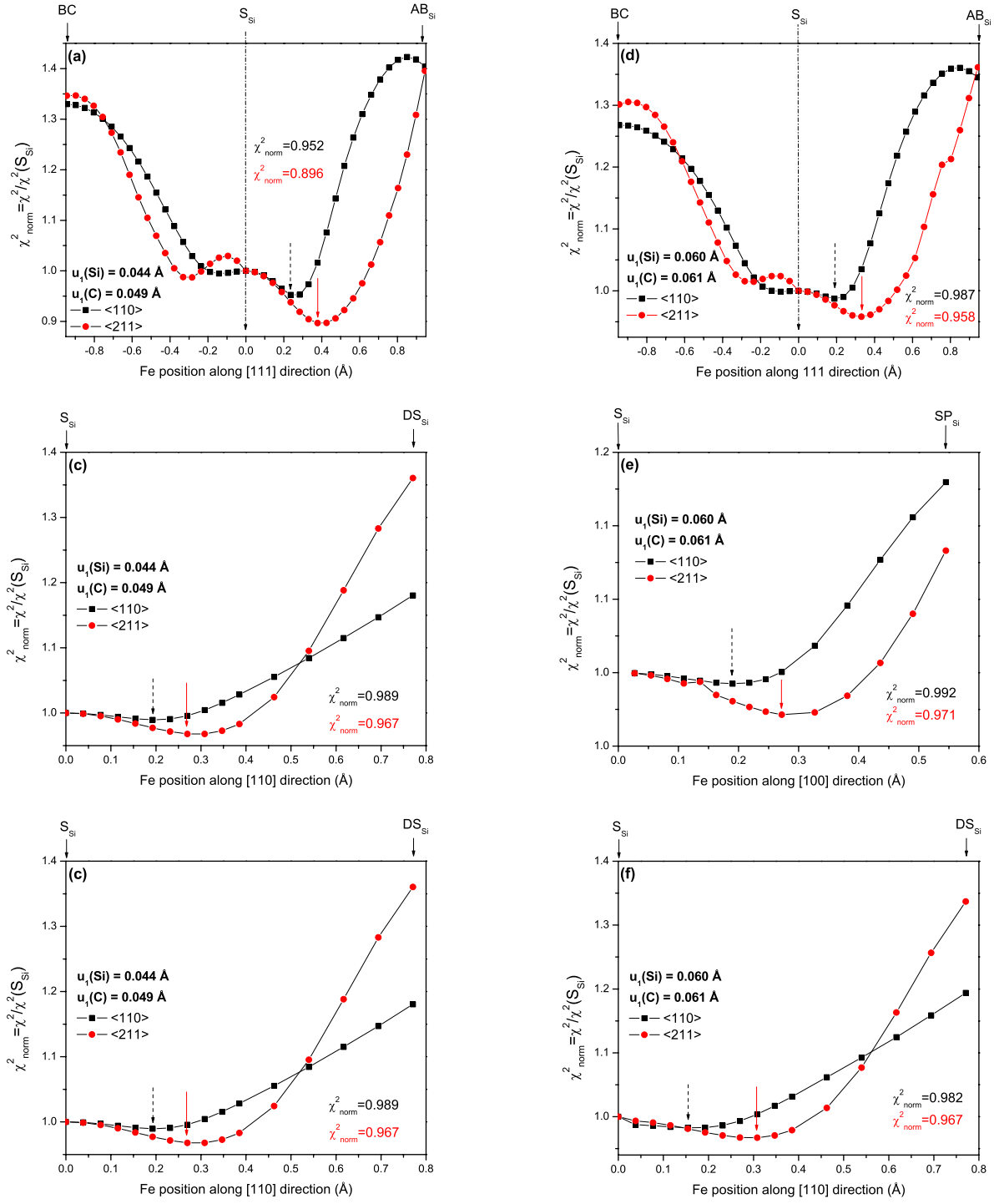

Figure A1. Normalized χ^2_{norm} of two-site fits to <110> and <211> patterns as a function of displacement from ideal S_{Si} for ^{59}Fe in the RT as-implanted state. (a,d) are for displacements along [111] towards BC and AB_{Si}, (b,e) along [100] towards SP_{Si}, and (c,f) along [110] towards DS_{Si}. (a-c) are results obtained using *manybeam* simulations for Si rms displacements of $u_1(Si)$=0.044 Å and $u_1(C)$=0.049 Å, while (d-f) used $u_1(Si)$=0.060 Å and $u_1(C)$=0.061 Å. While the first site was kept fixed at the ideal tetrahedral carbon interstitial (T_C), the position of the second site was moved in small steps. The χ^2 was in all cases normalized to that for the two-site fit of ideal T_C and ideal S_{Si}. The dashed and full arrows indicate the displacement positions where the lowest χ^2_{norm} was obtained.

A.2. After annealing at 500 °C

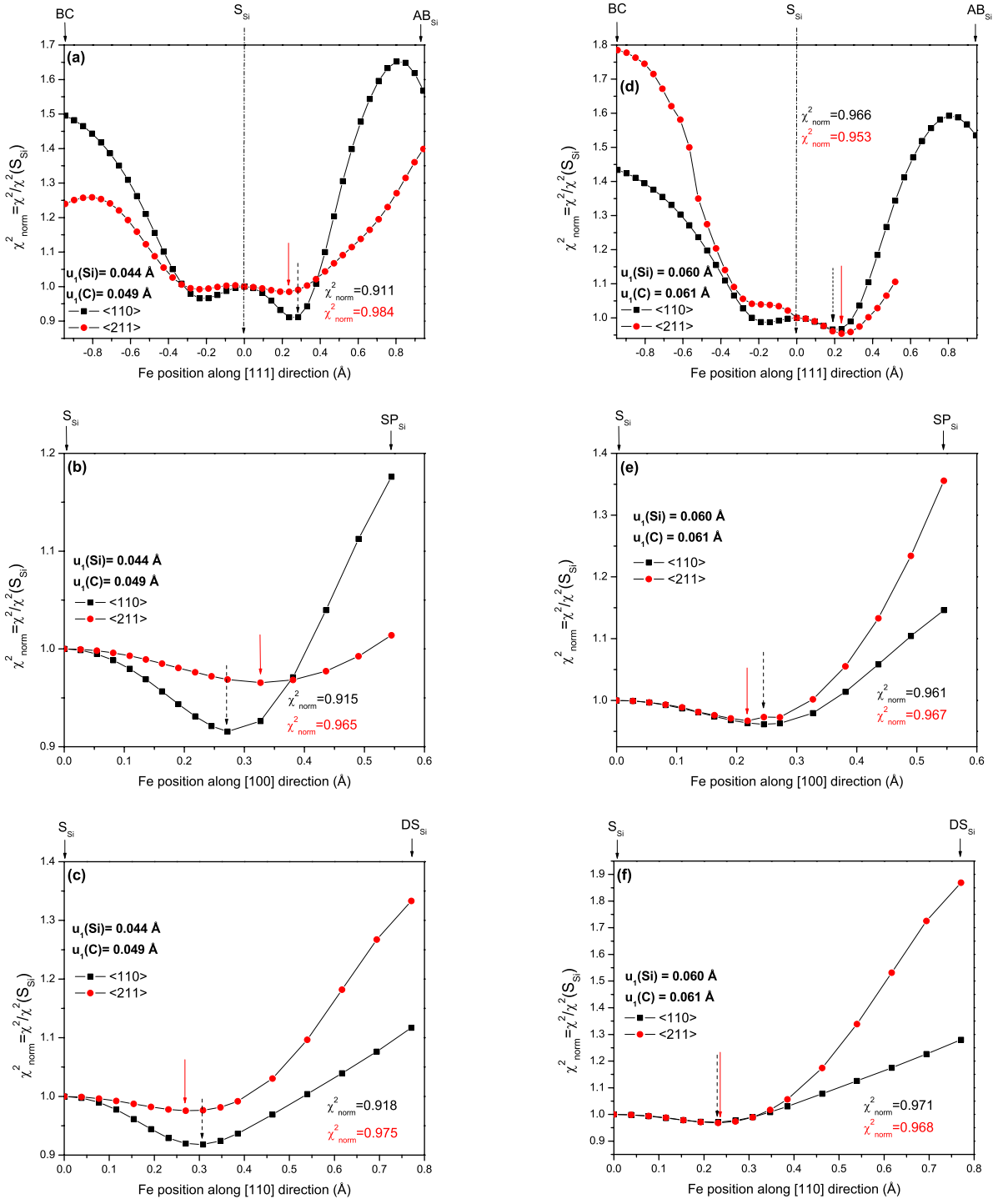

Figure A2. Same as figure A1 but after annealing at 500 °C.

A.3. After annealing at 800 °C

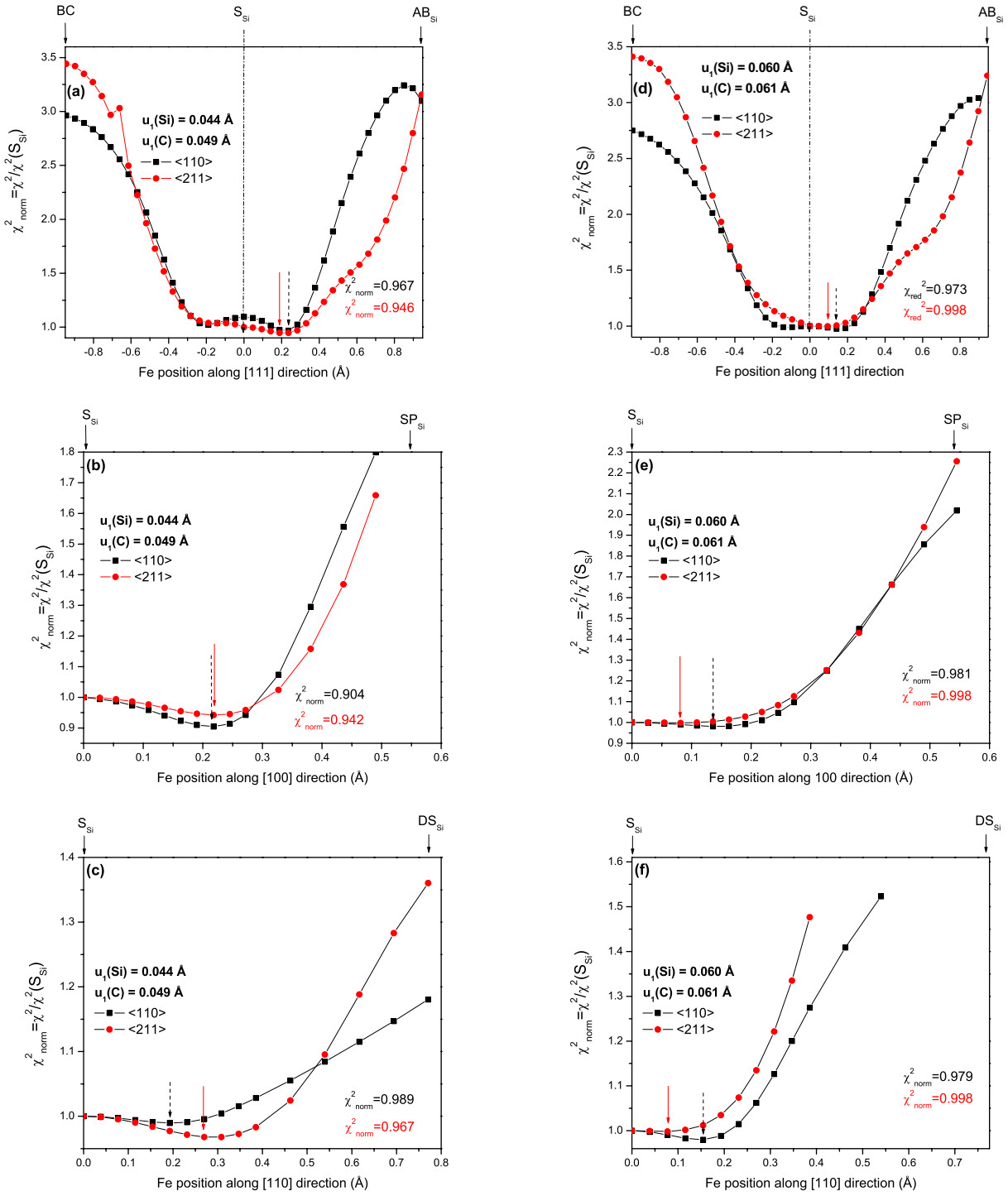

Figure A3. Same as figure A1 but after annealing at 800 °C.

A.4. Comparison of ^{59}Fe fractions using different SiC rms displacements

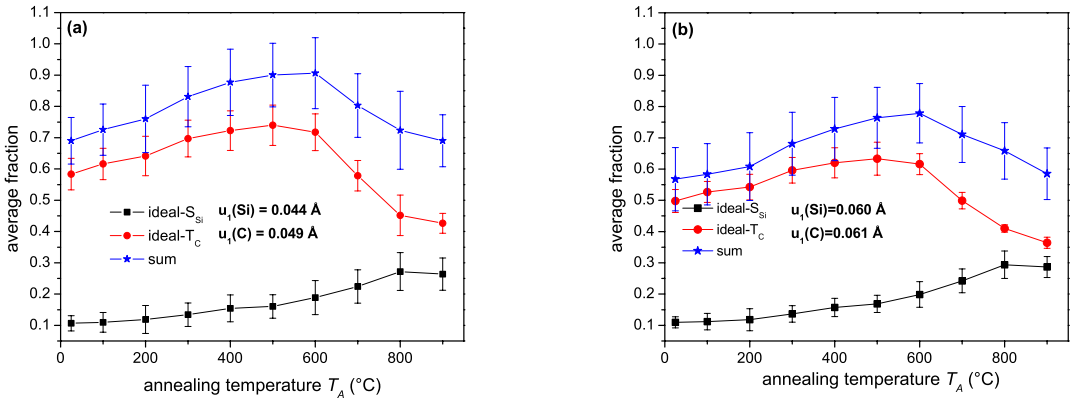

Figure A4. Fitted fractions for ^{59}Fe emitter atoms, obtained using *manybeam* simulations with two different sets of rms displacements u_1(Si) and u_1(C), on ideal substitutional Si (in black) and interstitial T_C sites (in red) plus the sum of both sites (in blue) as a function of the annealing temperature, averaged from the four measured crystallographic directions. The error bars represent the spread in fitted fractions for the different crystallographic directions.

References

[Schulz1979] H. Schulz, K.H. Thiemann, "Structure parameters and polarity of the wurtzite type compounds SiC–2H and ZnO", *Solid State Commun*. **32** 783–785 (1979).

[Peng2009] T.H. Peng, Y.F. Lou, S.F. Jin, W.Y. Wang, W.J. Wang, X.L. Chen, "Debye temperature of 4H–SiC determined by x-ray powder diffraction", *Powder Diffr*. **24** 311-314 (2009).

[Stelmakh2007] S. Stelmakh, E. Grzanka, M. Wojdyr, T. Proffen, S.C. Vogel, W. Palosz, B. Palosz, "Neutron diffraction studies of the atomic thermal vibrations in complex materials: application of the Wilson method to examination of micro and nano-crystalline SiC", *Z. Kristallogr.* **222** 174–887 (2007).

Appendix B

Identification of the preferential direction of displacement from the substitutional Si site for ^{56}Mn, ^{59}Fe, ^{65}Ni and ^{111}Ag in 3C-SiC

Table B.1-B.4 summarize the normalized χ^2_{norm} that corresponds to the best fits of 3C-SiC patterns when the TM probes are displaced from ideal S_{Si} sites, using the rms displacements u_1(Si) = 0.060 Å and u_1(C) = 0.061 Å, at room temperature and after two different annealing temperatures (500 °C, 800°C). For that purpose, in the case of ^{59}Fe (Table B.1), ^{56}Mn (Table B.2) and ^{65}Ni (Table B.3) two-site fits were performed, where the first site was kept fixed at the ideal interstitial T_C site, while the position of the second site was moved away from the ideal substitutional Si site in small steps of 0.047 Å along <111> directions towards BC or AB_{Si}, of 0.027 Å along <100> towards SP_{Si}, or of 0.039 Å along <110> towards DS_{Si} sites, as was shown already for ^{59}Fe in Appendix 1 (for location of these positions cf. Fig. 2.7). In the case of ^{111}Ag (Table B.4), where no interstitial site occupation was found, only one-site fits where the probe was moved away from ideal S_{Si} sites were performed. The objective of this study was to discover if the substitutional impurities were sitting preferentially on ideal substitutional Si sites or if they were slightly displaced along a specific crystallographic direction. Whereas the χ^2_{norm} corresponding to the displacements towards AB_{Si} sites indicates slightly better fits than for displacements towards BC, SP_{Si} or DS_{Si} sites, the improvements in fit quality are quite comparable. Hence it is concluded that while there seems to be a displacement from the ideal substitutional Si position for all TMs, it is not possible to identify its preferred direction. This

result can be explained since the continuum potentials used in the *manybeam* simulations show approximately rotational symmetry close to the atomic rows. Hence, if the displacements are small, say <0.3 Å, the direction of displacement does not particularly matter.

Table B.1. Normalized χ^2_{norm} of ^{59}Fe: <110> and <211> fits for RT as-implanted, as well as after annealing at 500 °C and 800 °C. Each value corresponds to the best fit obtained using two given sites: one fixed on T_C and the other being displaced from ideal substitutional Si site towards four different interstitial (BC, AB_{Si}, SP_{Si} and DS_{Si}) sites. The χ^2 was in all cases normalized to that for the two-site fit of ideal T_C and ideal S_{Si}. The values of the displacement that correspond to the best fit in each case are also given. Note that regarding $S_{Si}\rightarrow$ BC displacements for the <211> RT and 500 °C patterns fits only showed local minima with χ^2_{norm} above that for ideal S_{Si} [cf. Figs. A.1(d) and A.2(d)], while for the 800 °C pattern no minimum for $S_{Si}\rightarrow$ BC displacements was found.

<110> patterns	$S_{Si}\rightarrow$ BC		$S_{Si}\rightarrow AB_{Si}$		$S_{Si}\rightarrow SP_{Si}$		$S_{Si}\rightarrow DS_{Si}$	
	χ^2_{norm}	Disp. [Å]	χ^2_{norm}	Disp. [Å]	χ^2_{norm}	Disp. [Å]	χ^2_{norm}	Disp. [Å]
RT	0.998	0.10	0.987	0.19	0.992	0.19	0.982	0.15
500 °C	0.987	0.14	0.966	0.19	0.961	0.25	0.971	0.22
800 °C	0.989	0.14	0.973	0.14	0.981	0.14	0.979	0.15

<211> patterns	$S_{Si}\rightarrow$ BC		$S_{Si}\rightarrow AB_{Si}$		$S_{Si}\rightarrow SP_{Si}$		$S_{Si}\rightarrow DS_{Si}$	
	χ^2_{norm}	Disp. [Å]	χ^2_{norm}	Disp. [Å]	χ^2_{norm}	Disp. [Å]	χ^2_{norm}	Disp. [Å]
RT	1.014	0.24	0.958	0.33	0.971	0.27	0.967	0.31
500 °C	1.039	0.19	0.953	0.24	0.967	0.22	0.968	0.22
800 °C	1.0	0.	0.998	0.1	0.998	0.08	0.998	0.07

Table B.2. Normalized χ^2_{norm} of ^{56}Mn: <110> and <211> fits for RT as-implanted, as well as after annealing at 500 °C and 800 °C. Each value corresponds to the best fit obtained using the same conditions as the ones described for table B.1.

<110> patterns	$S_{Si}\rightarrow$ BC		$S_{Si}\rightarrow AB_{Si}$		$S_{Si}\rightarrow SP_{Si}$		$S_{Si}\rightarrow DS_{Si}$	
	χ^2_{norm}	Disp. [Å]	χ^2_{norm}	Disp. [Å]	χ^2_{norm}	Disp. [Å]	χ^2_{norm}	Disp. [Å]
RT	0.990	0.14	0.989	0.14	0.987	0.16	0.988	0.15
500 °C	0.984	0.14	0.988	0.10	0.979	0.14	0.983	0.12
800 °C	0.999	0.05	1.0	0.	1.0	0.	1.0	0.

<211> patterns	$S_{Si}\rightarrow$ BC		$S_{Si}\rightarrow AB_{Si}$		$S_{Si}\rightarrow SP_{Si}$		$S_{Si}\rightarrow DS_{Si}$	
	χ^2_{norm}	Disp. [Å]	χ^2_{norm}	Disp. [Å]	χ^2_{norm}	Disp. [Å]	χ^2_{norm}	Disp. [Å]
RT	0.979	0.14	0.982	0.24	0.982	0.22	0.982	0.23
500 °C	0.957	0.10	0.995	0.10	0.993	0.11	0.993	0.12
800 °C	0.929	0.14	0.994	0.10	0.998	0.08	0.998	0.08

Table B.3. Normalized χ^2_{norm} of ^{65}Ni: <110> and <211> fits for RT as-implanted, as well as after annealing at 500 °C and 800 °C. Each value corresponds to the best fit obtained using the same conditions as the ones described for table B.1.

<110> patterns	S_{Si}→ BC		S_{Si} →AB_{Si}		S_{Si}→ SP_{Si}		S_{Si}→DS_{Si}	
	χ^2_{norm}	Disp. [Å]	χ^2_{norm}	Disp. [Å]	χ^2_{norm}	Disp. [Å]	χ^2_{norm}	Disp. [Å]
RT	1.0	0.	1.0	0.	1.0	0.	1.0	0.
500 °C	1.0	0.	1.0	0.	1.0	0.	1.0	0.
800 °C	1.0	0.	1.0	0.	1.0	0.	1.0	0.

<211> patterns	S_{Si}→ BC		S_{Si} →AB_{Si}		S_{Si}→ SP_{Si}		S_{Si}→DS_{Si}	
	χ^2_{norm}	Disp. [Å]	χ^2_{norm}	Disp. [Å]	χ^2_{norm}	Disp. [Å]	χ^2_{norm}	Disp. [Å]
RT	1.0	0.	0.991	0.19	0.986	0.27	0.989	0.23
500 °C	0.969	0.23	0.978	0.24	0.980	0.19	0.977	0.19
800 °C	0.998	0.05	0.994	0.15	0.998	0.11	0.997	0.12

Table B.4. Normalized χ^2_{norm} of ^{111}Ag (1×10^{14} cm^{-2}): <110> and <211> fits for RT as-implanted, as well as after annealing at higher temperatures. In contrast to tables B.1-B-3, here each value corresponds to the best one-site fits obtained, where the probe is displaced from ideal substitutional Si site towards four different interstitial (BC, AB_{Si}, SP_{Si} and DS_{Si}) sites. The values of the displacement that correspond to the best fit in each case are also given.

<110> patterns	S_{Si}→ BC		S_{Si} →AB_{Si}		S_{Si}→ SP_{Si}		S_{Si}→DS_{Si}	
	χ^2_{norm}	Disp. [Å]	χ^2_{norm}	Disp. [Å]	χ^2_{norm}	Disp. [Å]	χ^2_{norm}	Disp. [Å]
RT	1.0	0.	1.0	0.	1.0	0.	1.0	0.
500 °C	0.989	0.14	0.940	0.24	0.992	0.11	0.979	0.19
800 °C	0.998	0.1	0.978	0.19	0.998	0.06	0.996	0.12

<211> patterns	S_{Si}→ BC		S_{Si} →AB_{Si}		S_{Si}→ SP_{Si}		S_{Si}→DS_{Si}	
	χ^2_{norm}	Disp. [Å]	χ^2_{norm}	Disp. [Å]	χ^2_{norm}	Disp. [Å]	χ^2_{norm}	Disp. [Å]
RT	0.999	0.05	1.0	0.	1.0	0.	1.0	0.
500 °C	0.862	0.38	0.903	0.52	0.968	0.22	0.942	0.31
800 °C	0.981	0.28	0.992	0.24	0.997	0.14	0.996	0.15

Table B.5. Normalized χ^2_{norm} of ^{111}Ag (6×10^{12} cm^{-2}): <110> and <211> fits for RT as-implanted, as well as after annealing at higher temperatures. Each value corresponds to the best fit obtained for the same conditions presented for table B.4.

<110> patterns	S_{Si}→ BC		S_{Si} →AB_{Si}		S_{Si}→ SP_{Si}		S_{Si}→DS_{Si}	
	χ^2_{norm}	Disp. [Å]	χ^2_{norm}	Disp. [Å]	χ^2_{norm}	Disp. [Å]	χ^2_{norm}	Disp. [Å]
RT	0.991	0.14	0.990	0.14	0.992	0.14	0.991	0.15
500 °C	0.962	0.19	0.980	0.14	0.986	0.11	0.975	0.15
800 °C	0.976	0.14	0.987	0.14	0.988	0.11	0.983	0.15

<211> patterns	S_{Si}→ BC		S_{Si} →AB_{Si}		S_{Si}→ SP_{Si}		S_{Si}→DS_{Si}	
	χ^2_{norm}	Disp. [Å]	χ^2_{norm}	Disp. [Å]	χ^2_{norm}	Disp. [Å]	χ^2_{norm}	Disp. [Å]
RT	0.975	0.28	0.901	0.33	0.939	0.27	0.942	0.27
500 °C	1.0	0.	0.981	0.19	0.984	0.16	0.986	0.15
800 °C	1.0	0.	0.972	0.19	0.978	0.16	0.978	0.15

Appendix C

Nuclear decay schemes of pure β^- emitters

^{56}Mn, ^{59}Fe, ^{65}Ni and ^{111}Ag are isotopes that emit β^- particles without having significant conversion electron lines. Note that all of these isotopes usually do also emit γ-radiation in addition to β^- particles. Experimental results from beta emission channeling are comparably simple to interpret: since the β particles are emitted directly by the mother nucleus during the decay, the angular emission yields give direct evidence of its lattice site. A major difficulty with these types of probes is the determination of the background caused by scattered electrons, as was outlined in section 2.5.3.

In contrast, channeling effects from conversion electrons (CE) are more difficult to assess: in most practical cases, conversion electrons are the result of excited states in the daughter nucleus of a β^-, β^+ or electron capture decay that de-excite to lower-lying states by directly transferring excitation energy to atomic electrons. As such CE emission channeling patterns typically give information on the lattice site of the daughter nucleus. Owing to the recoil received by the daughter nucleus during decay and the half-life of the excited state, CE emission channeling results are hence less straightforward to interpret.

The mass 124 beam used for the lattice location experiments of In was a mixture of 73% ^{124}In and 27% ^{124m}In. While both states decay by the emission of β^- particles, the decay of ^{124m}In is also accompanied by the emission of a number of conversion electrons, most prominently three lines with the following energies and branching ratios (number of CE per β^- decay): 73.7 keV

(6.5%), 91.1 keV (24%), and 115.9 keV (6.1%). Taking into account the composition of the mass 124 beam, a total of ~8.5% of the detected particles were CE resulting from two excited states in ^{124}Sn, which have half-lives of 3.1 μs and 0.27 μs, respectively (cf. Fig. C.6). Since the daughter nucleus ^{124}Sn has left the ^{124}In site due to nuclear recoil received during β^- decay and the half-lives of the CE emitting states are long enough for rearrangement of the outer shell electrons having taken place (which generally requires less than a few ns), the CE emission channeling effects, and hence ~8.5% of the overall channeling effects measured, are likely to represent the lattice sites of ^{124}Sn.

These schemes were extracted from the Livechart – Table of Nuclides – Nuclear structures and decay data (https://www-nds.iaea.org/).

C.1. ^{56}Mn → ^{56}Fe decay

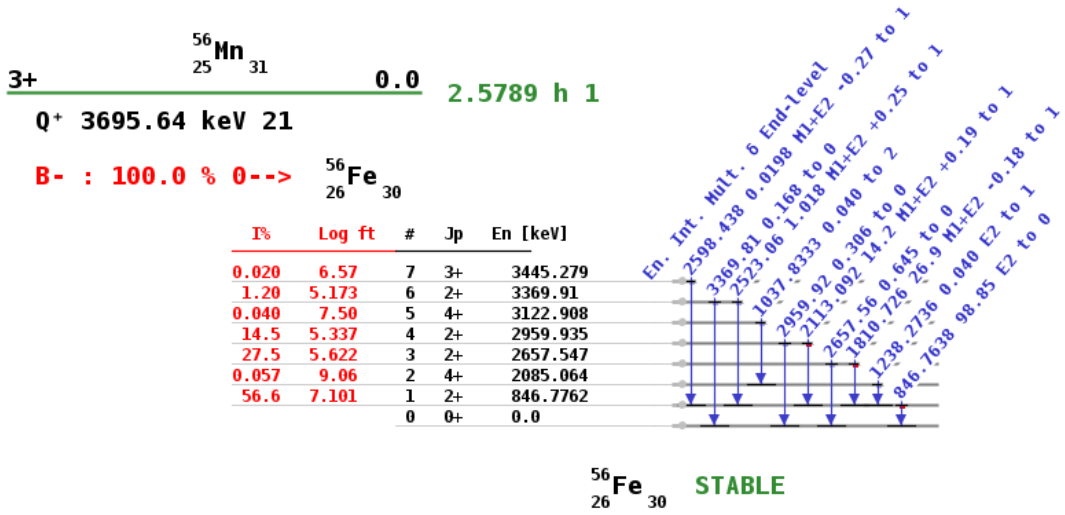

Figure C1. β^- decay of ^{56}Mn to ^{56}Fe used in the EC experiments presented in section 3.1.

C.2. $^{59}Fe \rightarrow {}^{59}Co$ decay

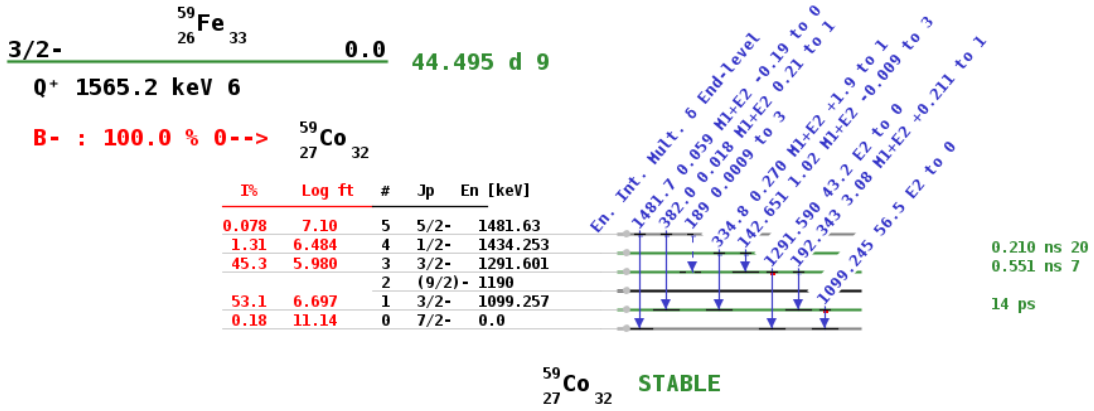

Figure C2. β⁻ decay of ^{59}Fe to ^{59}Co used in the EC experiments presented in section 3.1.

C.3. $^{65}Ni \rightarrow {}^{65}Cu$ decay

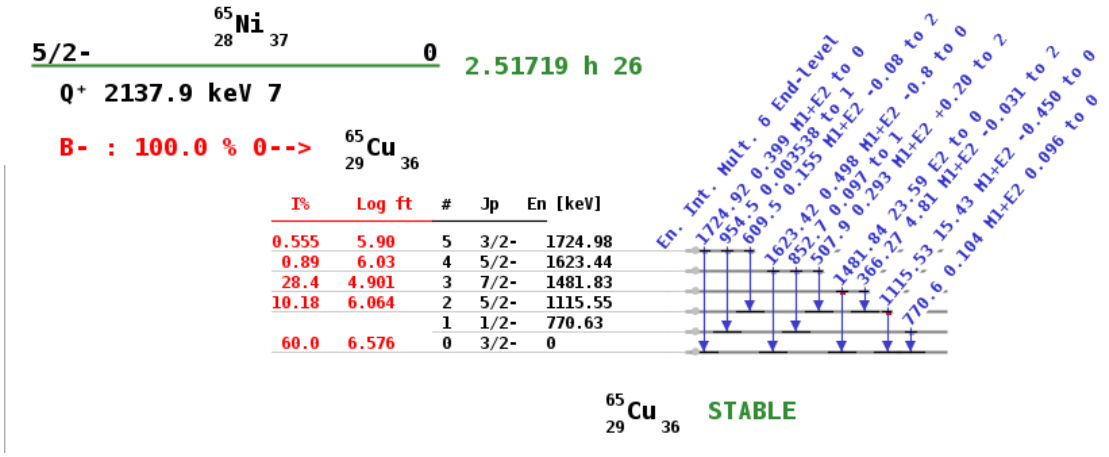

Figure C3. β⁻ decay of ^{65}Ni to ^{65}Cu used in the EC experiments presented in section 3.1.

C.4. $^{111}Ag \rightarrow {}^{111}Cd$ decay

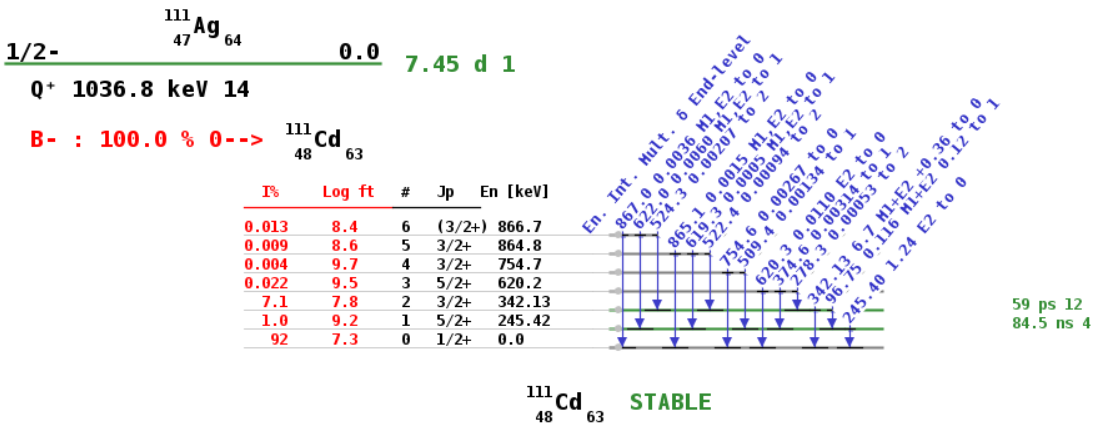

Figure C4. β⁻ decay of ^{111}Ag to ^{111}Cd used in the EC experiments presented in section 3.1.

C.5. $^{124}In \rightarrow {}^{124}Sn$ decay

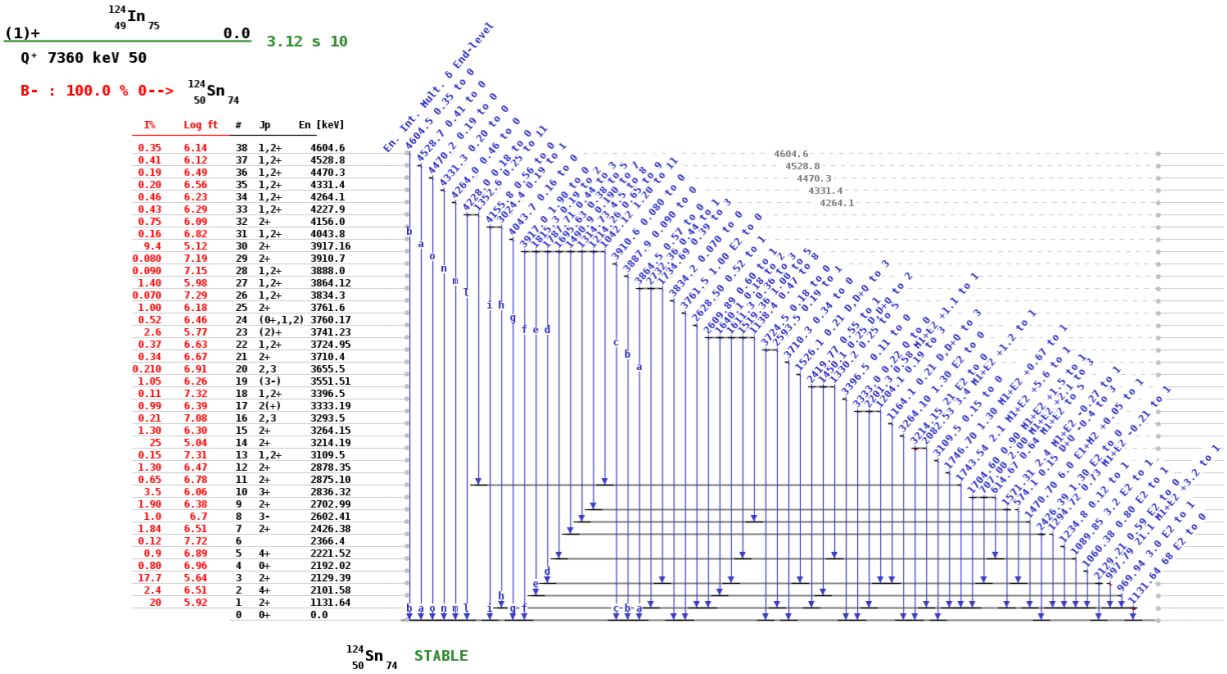

Figure C5. β^- decay of ^{124}In to ^{124}Sn used in the EC experiments presented in section 4.1.

C.6. $^{124m}In \rightarrow {}^{124}Sn$ decay

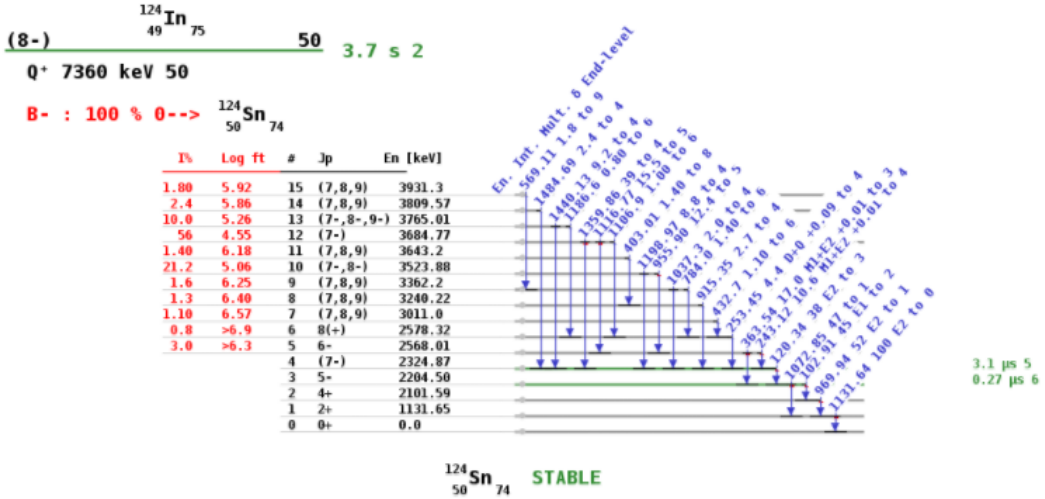

Figure C6. β^- decay of ^{124m}In to ^{124}Sn used in the EC experiments presented in section 4.1. Conversion electrons are mostly emitted by the excited states at 2324.87 keV and 2204.50 keV, which have half-lives of 3.1 µs and 0.27 µs, respectively.

List of publications and communications

The investigation carried out during this PhD program included the publications, oral and poster communications, listed below.

Publications

A.R.G. Costa, U. Wahl, J.G. Correia, E. David-Bosne, L.M. Amorim, V. Augustyns, D.J. Silva, M.R. da Silva, L.M.C Pereira, "Lattice sites of ion-implanted Mn, Fe and Ni in 6H-SiC", *Semicond. Sci. Technol*. **33** 015021(1-10) (2018)
doi: https://doi.org/10.1088/1361-6641/aa9f08

K. Johnston, J. Schell, J. G. Correia, M. Deicher, H. P. Gunnlaugsson, A. S. Fenta, E. David-Bosne, A.R.G. Costa, D. C. Lupascu, "The solid-state physics programme at ISOLDE: recent developments and perspectives*", J. Phys. G: Nucl. Part. Phys*. **44**, 104001(1-25) (2017)
doi: https://doi.org/10.1088/1361-6471/aa81ac

A.R.G. Costa, U. Wahl, J.G. Correia, E. Bosne, L.M. Amorim, V. Augustyns, D.J. Silva, M.R. da Silva, K. Bharuth-Ram, L.M.C. Pereira, "Lattice location of implanted transition metals in 3C-SiC", *J. Phys. D: Appl. Phys*. **50**, 215101(1-11) (2017)
doi: https://doi.org/10.1088/1361-6463/aa6878

U. Wahl, L.M. Amorim, V. Augustyns, A. Costa, E. David-Bosne, T.A.L. Lima, G. Lippertz, J.G. Correia, M.R. Silva, M.J. Kappers, K. Temst, A. Vantomme, L.M.C. Pereira, "Lattice location of Mg in GaN: A fresh look at doping limitations", *Phys. Rev. Letters* **118**, 095501 (2017)
doi: https://doi.org/10.1103/PhysRevLett.118.095501

M. Stachura, A. Gottberg, K. Johnston, M.L. Bissel, R.F.G. Ruiz, J.G. Correia, A.R.G. Costa *et al*., "Versatile Ion-polarized techniques on-line (VITO) experiment at ISOLDE-CERN", *Nucl. Instruments Methods Phys. Res.* B **376** 369-373 (2016)
doi: https://doi.org/10.1016/j.nimb.2016.02.030

D.J. Silva, U. Wahl, J.G. Correia, V. Augustyns, T.A.L. Lima, A. Costa *et al*., "Drawing the geometry of 3d transition metal-boron pairs in silicon from electron emission channeling experiments", *Nucl. Instruments Methods Phys. Res.* B **371** 59-62 (2016)
doi: https://doi.org/10.1016/j.nimb.2015.09.051

T.A.L. Lima, U. Wahl, J.G. Correia, V. Augustyns, D.J. Silva, A. Costa *et al*., "Identification of the interstitial Mn site in ferromagnetic (Ga,Mn)As", *Appl. Phys. Letters* **106** 012406(1-5) (2015)
doi: https://doi.org/10.1063/1.4905556

U. Wahl, J.G. Correia, A. Costa, E. David-Bosne, L.M.C. Pereira, L.M. Amorim, V. Augustyns, K. Temst, A. Vantomme, M.R. da Silva, D.J. Silva, J.P. Araújo, P. Miranda, K. Bharuth-Ram, "Emission Channeling with Short-Lived Isotopes (EC-SLI) at CERN's ISOLDE facility", Proceedings of the First International African Symposium on Exotic Nuclei (IASEN 2013), iThemba LABS, Cape Town, South Africa, 1-6/12/2013, World Scientific, Singapore 563-573 (2014)
doi: http://dx.doi.org/10.1142/9789814632041_0061

Oral presentations

A.R.G. Costa, U. Wahl, J. G. Correia, E. Bosne, L. Amorim, V. Augustyns, D. J. Silva, M. R. da Silva, K. Bharuth-Ram and L. M. C. Pereira, "Lattice location of 3d transition metals in Silicon Carbide", ISOLDE Workshop, Geneva, Switzerland (December 2016)

D. J. Silva, A.R.G. Costa, U. Wahl, J. G. Correia, V. Augustyns, T. A. L. Lima, E. Bosne, M. R. da Silva, L. M. C. Pereira and J. P. Araujo, "Exploring the geometry of 3d transition metal complexes in silicone with electron emission channeling", International Conference on defects in Semiconductors (ICDS2015), Helsinkia, Finland (July 2015)

Poster presentations

A.R.G. Costa, U. Wahl, J.G. Correia, L.M.C. Pereira, M.R. da Silva, D.J. Silva, K. Bharuth-Ram, "Lattice Location of implanted ^{111}Ag in 3C-SiC", ISOLDE Workshop, Geneva, Switzerland (December 2015)

A.R.G. Costa, U. Wahl, J.G. Correia, L.M. Amorim, L.M.C. Pereira, M.R. da Silva, D.J. Silva, K. Bharuth-Ram, "Lattice Location of implanted ^{56}Mn in 3C-SiC", International Conference on defects in Semiconductors (ICDS2015), Helsinkia, Finland (July 2015)

A.R.G. Costa, U. Wahl, J.G. Correia, L.M. Amorim, L.M.C. Pereira, M.R. da Silva, D.J. Silva, K. Bharuth-Ram, "Lattice Location of implanted ^{56}Mn in 3C-SiC", ISOLDE Workshop, Geneva, Switzerland (December 2014)

A.R.G. Costa, U. Wahl, J.G. Correia, L.M. Amorim, L.M.C. Pereira, M.R. da Silva, D.J. Silva, K. Bharuth-Ram, "Lattice Location of implanted ^{59}Fe in 3C-SiC", ISOLDE Workshop, Geneva, Switzerland (December 2013)

List of acronyms and abbreviations

ADC	analog digital converter
AEM	analytical electron microscopy
D	diffusion coefficient
D_0	pre-exponential factor
DLTS	deep level transient spectroscopy
dpa	displacements per atom
EC	emission channeling
EC-SLI	emission channeling with short-lived isotopes
E_A	energy barrier
E_B	binding energy
E_g	band gap energy
E_M	migration energy
EDS	energy dispersive X-ray spectroscopy
ENDOR	electron nuclear double resonance
EPR	electron paramagnetic resonance
FOM	figure of merit
GHM	high mass beam line
GLM	low mass beam line
GPS	general purpose separator
ISOLDE	isotope separator on line device
MS	Mössbauer spectroscopy
NRA	nuclear reaction analysis
PAC	perturbed angular correlation
PIXE	particle induced X-ray emission
PSB	proton synchrotron booster
RBS	Rutherford backscattering spectrometry
RBS/C	Rutherford backscattering and channeling spectrometry
RILIS	resonance ionization laser ion source
rms	root mean square
R_p	projected range during slowing down of a particle
RT	room temperature

SIC	small implantation chamber
SiC	silicon carbide
SIMS	secondary-ion mass spectrometry
SPEG	solid phase epitaxial regrowth
STEM	scanning transmission electron microscopy
SRIM	stopping and range of ions in matter
$t_{1/2}$	half-life
T_A	annealing temperature
T_D	Debye temperature
TEM	transmission electron microscopy
TM	transition metal

List of Tables

List of figures